Karlsruher Institut für Technologie

Thermally induced structural reordering in Li- and Mn-rich layered oxide lithium ion cathode materials

Zur Erlangung des akademischen Grades eines

DOKTORS DER NATURWISSENSCHAFTEN

(Dr. rer. nat.)

von der KIT-Fakultät für Chemie und Biowissenschaften

des Karlsruher Instituts für Technologie (KIT)

genehmigte

DISSERTATION

von

Florian Sigel, M.Sc.

Referent: Prof. Dr. Helmut Ehrenberg

Korreferent: Prof. Dr. Rolf Schuster

Tag der mündlichen Prüfung: 13.12.2018

I hereby declare that I have made this work independently and used no other than the specified sources and tools, as well as, whether verbatim or with regards to content, indicated all citations as such and I have paid attention to the statute of the Karlsruhe Institute of Technology (KIT) in the current version to ensure good scientific practice.

Karlsruhe, October 29, 2018

Florian Sigel

Zusammenfassung

In den letzten Jahren wurden beträchtliche Anstrengungen unternommen, um die Korrelation zwischen der Struktur und den elektrochemischen Eigenschaften von Li- und Mn-reichen NCM Schichtoxid Lithium-Ionen-Kathodenmaterialien besser zu verstehen. Insbesondere wurden Hochenergie Kathodenmaterialien mit der weit verbreiteten $Li_{1.2}Ni_{0.15}Co_{0.1}Mn_{0.55}O_2$ (HE5050) Zusammensetzung untersucht. Eine graduelle Umwandlung von einem trigonalen $R\bar{3}m$ Schichtoxid in eine kubische $Fd\bar{3}m$ Spinellstruktur während der elektrochemischen Zyklierung (De-/Lithiierung) führt zu einem unerwünschten Abfall der mittleren Lade- und Entladungsspannung, der auch als 'Voltage Fade' bezeichnet wird. Dieser Umwandlungsprozess verläuft über eine metastabile Struktur, die nach dem ersten Lade-/Entladezyklus (Formierung) vorliegt und durch einen Verlust der lokalen Kationenordnung und der Bildung von Gitterfehlern im ursprünglich hochgeordneten Material gekennzeichnet ist. In dieser Arbeit wurde der Ordnungs–Unordnungs-Übergang in Li- und Mn-reichen Schichtoxiden detailliert auf einer langreichweitigen atomaren Skala durch Röntgen- und Synchrotronstrahlungspulverdiffraktometrie sowie auf einer sehr lokalen atomaren Skala mit ^{6,7}Li-Kernspinresonanz- und Röntgenabsorptionsspektroskopie untersucht. Eine strukturelle 'Neuordnung' wurde durch eine thermische Behandlung (150 °C – 300 °C) in entladenen (lithiierten) und geladenen (delithiierten) Proben induziert, welche entweder zu einer teilweisen Wiederherstellung des hochgeordneten Ausgangszustands führte oder zu einer Intensivierung der strukturellen Degradation hin zu einer spinelltypischen Kationenanordnung. Die so erhaltenen strukturellen Umordnungsvorgänge wurden erneut auf einer langreichweitigen und lokalen atomaren Skala untersucht und mit den veränderten elektrochemischen Eigenschaften korreliert. Darüber hinaus wurde eine stark elektrochemisch ermüdete Probe (300 Zyklen), die einen ausgeprägten Spannungsabfall zeigt, in ihrem entladenen Zustand thermisch behandelt. Dieses Experiment führte zu einer teilweisen Wiederherstellung der pristinen hochgeordneten Struktur und den damit verbundenen elektrochemischen Eigenschaften, einschließlich der Wiedererhöhung der mittleren Lade- und Entladespannung. Abschließend wurden die Ergebnisse aller Messungen zu einem kohärenten Modell zusammengefasst, das den Einfluss der lokalen Kationenordnung, der Gitterdefekte und des Sauerstoffuntergitters auf die elektrochemischen Eigenschaften, wie der Sauerstoffredoxaktivität und den Voltage Fade, erklären kann.

Abstract

In recent years a considerable amount of effort has been put into a better understanding of the correlation between structure and electrochemical properties of Li- and Mn-rich NCM layered oxide lithium ion cathode materials, such as the widely spread $Li_{1.2}Ni_{0.15}Co_{0.1}Mn_{0.55}O_2$ (HE5050) composition. A gradual transformation from a trigonal $R\bar{3}m$ layered oxide towards a cubic $Fd\bar{3}m$ spinel structure during electrochemical cycling (de-/lithiation) results in an unwanted decay of the mean charge and discharge voltages, called 'voltage fade'. This transformation process proceeds via a metastable structure, which is present after the first charge/discharge cycle (formation) and is characterized by a local 'de'-arrangement of cations and the formation of various lattice defects in the initially well-ordered material. In this work, the order-disorder transition in Li- and Mn-rich layered oxides is studied in detail on a long-range atomic scale by X-ray and synchrotron radiation powder diffraction as well as on a very-local atomic scale by ^{6,7}Li nuclear magnetic resonance and X-ray absorption spectroscopy. A structural 're'-ordering was induced by a mild thermal treatment (150 °C – 300 °C) in discharged (lithiated) and charged (delithiated) electrodes, which resulted either in a partial recovery of the well-ordered pristine state or in an intensification of the structural degradation towards a spinel-type cation arrangement, respectively. The structural reordering processes thus obtained were again studied on a long-range and local atomic scale and correlated with the altered electrochemical properties. Furthermore, a highly electrochemically fatigued electrode (300 cycles) exhibiting a pronounced voltage fade was thermally treated in its discharged state. This experiment resulted again in a partial recovery of the initially well-orderd structure and the therewith associated electrochemical properties, including the re-increase of the mean charge and discharge voltages, i.e. resetting the voltage fade. Finally, the findings from all measurements were merged into a coherent model that is capable to explain the influence of the local cation ordering, lattice defects and the oxygen sublattice on the electrochemical properties, such as the oxygen redox activity and the voltage fade.

Acknowledgment

First of all, I want to thank my supervisor Prof. Dr. Helmut Ehrenberg who gave me the chance to do a PhD in his group, for his support, guidance, and valuable advice during this work. I would like to express my sincere gratitude to Dr. Björn Schwarz for his enthusiastic guidance and support. Several ideas in this thesis were emerged through our energetic discussions. I would also like to thank Dr. Sylvio Indris for teaching me the NMR technique and for providing helpful practical advices in order to conduct my experiments and data evaluation. In addition, I would like to thank Prof. Dr. Rolf Schuster for the interest in my work.

I also owe gratitude to my colleagues in Institute of Applied Materials – Energy Storage Systems for their support as well as the excellent and warm working atmosphere. Especially I want to thank Dr. Karin Kleiner for conducting the soft XAS measurements (ANKA) and the effective support in evaluating the data, Bettina Hunzinger and Lars Esmezjan for SEM imaging, Dr. Murat Yavuz for the the kind support at the powder diffraction beamline and data processing, and Dr. Thomas Bergfeldt for the elementary analysis. Furthermore, I want to thank Markus Schmitt (IBG) for the maintenance of the NMR spectrometer and repairing my 'crashed' NMR probes. I would like to thank Liuda Mereacre and my student research assistant Caroline Bender for their kind support and assistance in material synthesis, sample preparation and electrochemical characterization. I am also thankful for the great time and many sleepless nights spend with Angelina, Qiang, Murat, Christoph, Weibo, Heike, Geethu and Georg during the synchrotron beamtime in Hamburg and Barcelona.

The Financial support from the Deutsche Forschungsgemeinschaft DFG within the Research Collaborative Centre 595 'Electrical Fatigue in Functional Materials' (Project T3) is gratefully acknowledged. This work has also benefited from beamtime allocation by the High Resolution Powder Diffraction Beamline P02.1 and the Applied X-ray Absorption Spectroscopy Beamline P65 at PETRA III, DESY in Hamburg as well as the WERA Beamline for Soft X-ray Spectroscopy and Microscopy at the Karlsruhe synchrotron light source ANKA and the Materials Science and Powder Diffraction (MSPD) beamline at ALBA in Barcelona.

Finally, I would like to thank my girlfriend Anna and my parents for their kind support, love and confidence in me.

Contents

1. Motivation

In the recent two decades, rechargeable lithium ion batteries have conquered the commercial market for mobile energy sources, e.g. they are used in portable electronics and battery electric vehicles, due to their outstanding gravimetric and volumetric energy densities. Current research and development is focused on the reduction of the battery pack costs per kilowatt-hour as well as solving safety and lifetime issues in order to pave the way for an economic and efficient operation in electrified vehicles, for example. In order to optimize already established or potential next generation Li ion battery materials for longer lifetime, it is mandatory to gain knowledge about the occurring degradation processes during operation and storage. Therefore, a correlation between structure and electrochemical properties of the battery electrode materials is aspired, from which degradation mechanisms, lifetime expectancies, and improvement strategies can be derived.

Layered transition metal (TM) oxides such as the 'Li- and Mn-rich' layered oxides, formed as solid solutions between the end members Li_2MnO_3 and $LiTMO_2$ (TM = Ni, Co, Mn) (NCM) are promising candidates for next generation Li ion battery cathodes that offer high reversible capacities (>250 mAh/g) and higher safety together with reduced costs [1]. So far, a gradual decay of the mean charge and discharge voltage during electrochemical cycling called 'voltage fade' as well as a profound hysteresis between charging and discharging are major drawbacks of this material class. A gradual cation rearrangement towards a cubic $LiTM_2O_4$-type spinel via a highly defective metastable interim phase during cycling is supposed to cause these energy inefficiencies [2].

Unlike conventional $LiTMO_2$ cathode materials, the Li- and Mn-rich descendants present a pronounced 'formation' or often called 'activation' process in the initial charge, which is manifested by a long 'plateau' at around 4.5 V in the voltage vs. charge capacity curve. This formation process leads to a structural rearrangement including the loss of the initially highly ordered cation arrangement [3] and goes along with the depletion of electrochemical available lithium sites [4] as well as the partial loss of oxygen [5, 6]. Moreover, this initial formation process provokes a highly defective metastable structure, which is the onset for the gradual transformation towards

a spinel-type cation arrangement [7]. These defects can form in order to maintain the charge balance during charge/discharge, e.g. by the oxidation of the oxygen lattice [8] and the formation of peroxide species or oxygen dimers [9, 10]. Furthermore, they can compensate the resulting lattice strain during de/-lithiation such as by the formation of tetrahedral TMs [11, 12, 13, 14], Li/TM dumbbells [4, 12], oxygen vacancies [14, 15], Li^+/H^+-exchange [16], nano-twins [17, 18] and dislocations [19]. These defects are presumably inducing the voltage and capacity fade as well as the pronounced hysteresis in the Li- and Mn-rich cathode materials. However, so far a coherent picture regarding the decisive processes involved in the initial order-disorder transition as well as the subsequent far-reaching structural changes during cycling is still missing.

In order to emphasize the motivation and scientific issue of this work, two key observations are now briefly presented: A partially charged Li- and Mn-rich cathode sample (delithiated), which experienced the initial formation cycle, was exposed to a mild thermal treatment inducing a cation rearrangement in the highly defective metastable structure towards the thermal equilibrium. Surprisingly, a very similar effect on the electrochemical properties was found in comparison to a sample, which experienced many charge and discharge cycles. The result of this experiment is illustrated in Figure 1.1a. Here, the cell voltage vs. normalized discharge capacity curves are plotted for a fresh sample after formation as well as the electrochemically and the thermally fatigued sample. The voltage fade is clearly observable in both samples and leads to a decrease of the discharge voltage and therefore a loss of energy density, as highlighted by the area shaded in blue. In a second experiment, a highly cycled sample that demonstrates a pronounced voltage fade was thermally treated in a discharged state (lithiated). As apparent from Figure 1.1b, this induced a partial recovery of the initially high discharge voltage, i.e. the voltage fade could be reversed as emphasized by the green shaded area. Obviously, the involved processes are strongly depending on the sample's lithium content (state of charge) leading to a quite different modification of the electrochemical properties.

The motivation of this work is to get more insight into the influence of cation ordering and defects on the electrochemical properties. For this purpose, a Li- and Mn-rich NCM with a nominal composition of $Li_{1.2}Ni_{0.15}Co_{0.1}Mn_{0.55}O_2$ was transferred into a highly defective metastable state by the initial formation process. This order-disorder transition was studied in detail on the long-range atomic scale by X-ray powder diffraction (XRPD) as well as on a very-local atomic scale by ^{6}Li nuclear magnetic resonance (NMR) measurements and correlated with the modified electrochemical features. Moderate thermal treatments at temperatures ranging from 150 °C to 300 °C were con-

ducted on the highly defective metastable material (after formation) in order to induce a structural reordering towards the thermodynamic equilibrium. These studies were carried out for different states of charge (degrees of delithiation) as well as for electrochemically fatigued samples after 300 cycles. The therewith-induced structural changes were investigated by synchrotron radiation powder diffraction (SRPD), ^{6,7}Li NMR and X-ray absorption spectroscopy (XAS). The observed structural features were finally correlated with the evolution of the electrochemical characteristics and comprised in a model providing further insights in the mechanisms involved in the initial formation and the subsequent degradation processes.

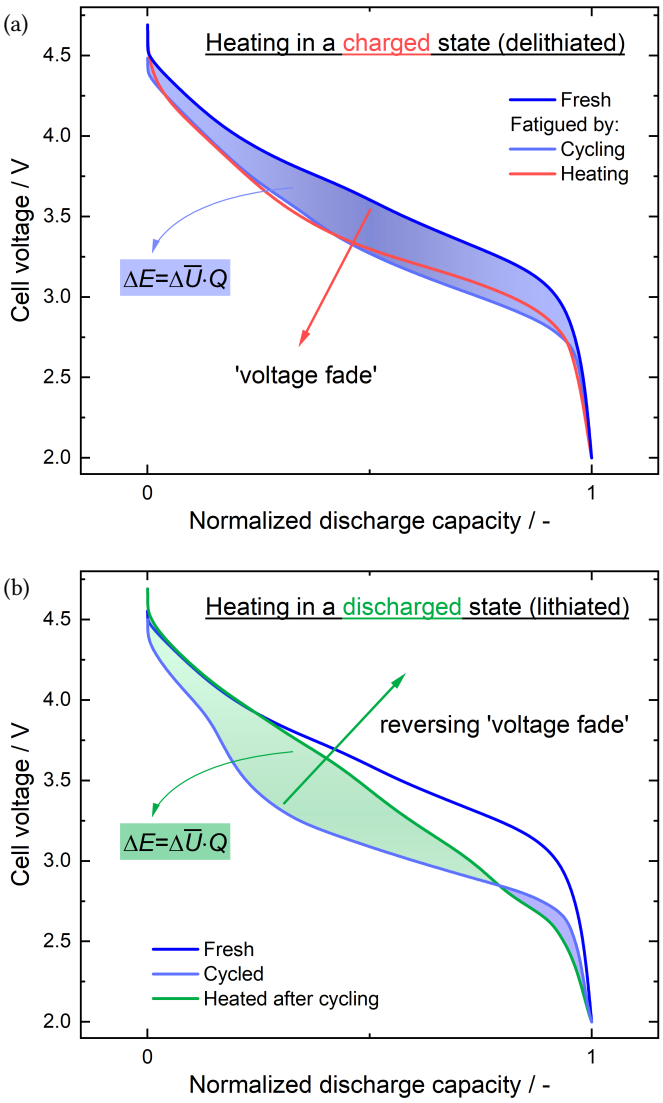

Figure 1.1.: Cell voltage vs. normalized discharge capacity of two key experiments regarding the thermal treatment of charged (a) and discharged (b) Li- and Mn-rich cathode samples.

2. Introduction

This chapter gives a brief introduction to the principle of lithium ion batteries (Section 2.1) and the corresponding cathode materials (positive electrode) used for this type of battery, in particular the Li- and Mn-rich materials (Section 2.2). Thereby the emphasis is put on the structural characteristics of these materials. A detailed presentation regarding the electrochemical properties will be given in the first part of the results section of this work (Section 5.1.1) on the basis of self-synthesized Li ion cathode materials with varying Li-*TM*-O compositions (*TM*=Ni,Co,Mn). Furthermore, terminologies regarding the electrochemical analysis are summarized in Section 2.3.

2.1. Lithium ion battery

Rechargeable batteries reversibly convert stored chemical energy into electrical energy during discharging and contrariwise during charging. The amount of electrical energy, which can be released by a battery depends on the quantity of transferred charge (capacity) and the potential difference between the two battery electrodes, named cathode and anode. Lithium has a low standard electrode potential, -3.04 V versus standard hydrogen electrode, as well as a high charge to molar mass ratio, and thus is an adequate candidate for high energy density batteries.
Although non-rechargeable (primary) lithium metal anode batteries, e.g. with manganese dioxide as opposing cathode material, were already commercialized in the 1970's, safety and lifetime issues prohibited the introduction of similarly designed rechargeable (secondary) lithium batteries [20]. Pure lithium metal anodes tend to form dendrites during electrochemical cycling, which leads to a gradual capacity fade as a result of irreversible reactions with the electrolyte and finally to short circuits between anode and cathode [21]. The replacement of the lithium metal anode with Li ion intercalation materials paved the way for the breakthrough of rechargeable Li ion batteries and led to the commercial launch in 1991 by Sony Corporation [20], using $LiCoO_2$ as cathode and non-graphitizable carbon as anode material, respectively. Due to the fact that lithium dendrite

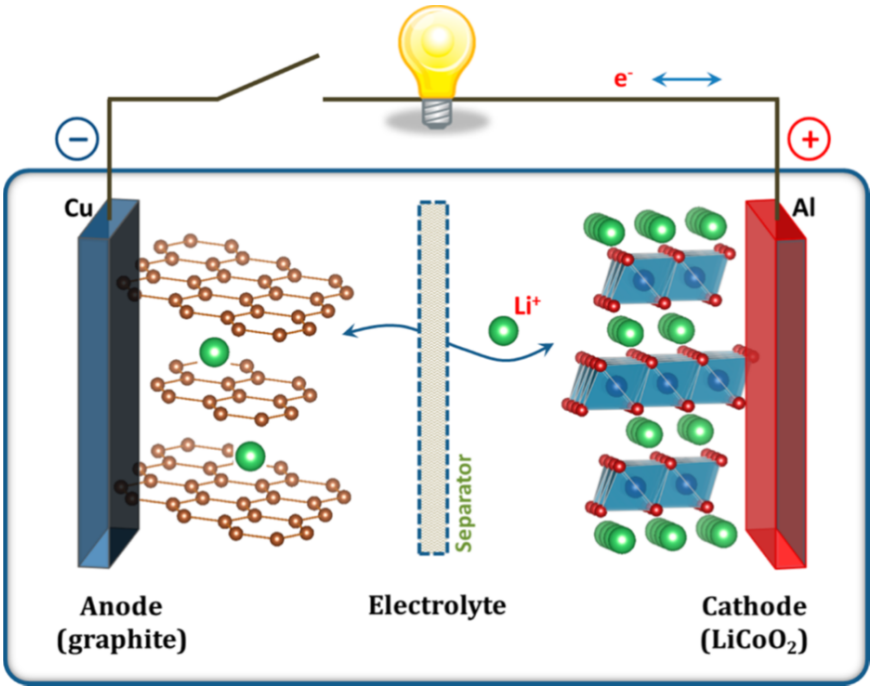

Figure 2.1.: Schematic illustration of a 'rocking chair' Li ion battery. Reprinted with permission from [22]. Copyright(2013) American Chemical Society.

growth and electrolyte decomposition are significantly reduced in this cell design, safety and cyclability are improved remarkably. The reached gravimetric energy densities were as high as 120–150 Wh/kg and therefore two to three times higher than those of usual Ni–Cd or Ni-MH batteries at that time.

A scheme of the $LiCoO_2$/graphite lithium ion battery is illustrated in Figure 2.1. It is composed of two electrodes, the graphite anode (negative electrode) and the $LiCoO_2$ cathode (positive electrode), which are deposited in a liquid Li ion conducting electrolyte. Anode and cathode side of the battery are commonly defined in direction of discharge, i.e. the 'electric energy releasing' process. A porous separator in between electronically isolates the two electrodes from each other. The pores within the cell stack are wet with liquid electrolyte, which subsequently enables the ionic Li^+ charge transport between the two electrodes. Current collectors on both electrodes finally provide the electronic contact to the appliance or charging device.

Common lithium ion batteries operate on the 'rocking chair' principle [23]: during the discharge step, Li ions are deintercalated from the anode Li host and intercalated into the cathode Li host, whereas the electrolyte provides the transport of ionic charge carriers between the two electrodes. The electron charge compensation of the two Li hosts is carried out by the electron flow through the

current collectors and the consumer device. Since this de-/intercalation processes are in principle highly reversible, the charging step proceeds vice versa.

The electrodes are usually fabricated in a wet mixing and coating process. Therefore the active electrode materials are dispersed together with a binder (typically polyvinylidene fluoride (PVDF)) and conductive additives (carbon black, graphite), for instance, with *N*-Methyl-2-pyrrolidone (NMP) as dispersing agent, coated on a current collector and compacted with a calender in order to adjust the electrode porosity. Finally, electrodes and separators are placed into the cell casing, e.g. in coin, pouch, prismatic or round cells, and wet with a liquid electrolyte. The liquid electrolytes are composed of a Li ion conducting salt, an organic solvent or a mixture of various solvents as well as electrolyte additives. As an example, the well-known LP30 electrolyte is composed out of 1 M lithium hexafluorophosphate ($LiPF_6$) in a 1:1 (w/w) solution of ethylene carbonate (EC) and dimethyl carbonate (DMC).

Recent research and development activities have been focused on the introduction of novel high energy density, low cost and environment-friendly cathode, anode and electrolyte materials such as the replacement of the liquid electrolyte with a solid electrolyte [24] and high capacity anode materials like the silicon-based anode materials instead of graphite [25]. In the following section, the electrochemical as well as the structural characteristics of layered transition metal oxide Li ion cathode materials will be pointed out in detail, in particular the Li- and Mn-rich layered oxides, which are promising candidates for high energy and low cost next generation cathode materials.

2.2. Lithium ion battery cathode materials

The profile of requirements for a suitable Li ion battery cathode material includes the following points [27, 28]: i) The potential difference vs. Li/Li^+ and the extractable lithium per formula unit and molar mass of the cathode material should be high in order to maximize the storable specific energy density. ii) The de/-intercalation processes should be highly reversible, i.e. the absence of irreversible structural changes, which is mandatory for a good battery cyclability. iii) Besides a high energy density, the power density plays an important role for the applicability. Therefore, a good electronic and ionic conductivity of the Li ion host material is crucial for a feasible current rate. iv) The oxidation potentials of the cathode should lie within the band gap of the used electrolyte. v) The material should be inexpensive, environment-friendly and should provide a good chemical, mechanical as well as thermal stability.

However, since not all requirements are exclusively provided by one material class, today's Li ion batteries are based on different cathode materials, which are selected on the base of the required profile of the specific application. Figure 2.2 shows an overview of different types of typical cathode materials and their specific discharge capacities as well as their potentials vs. Li/Li^+. The presented transition metal oxide and phosphate materials can be divided into three different groups according to the structural arrangement of the Li and TM ions in the anionic sublattice that form Li ion trans-

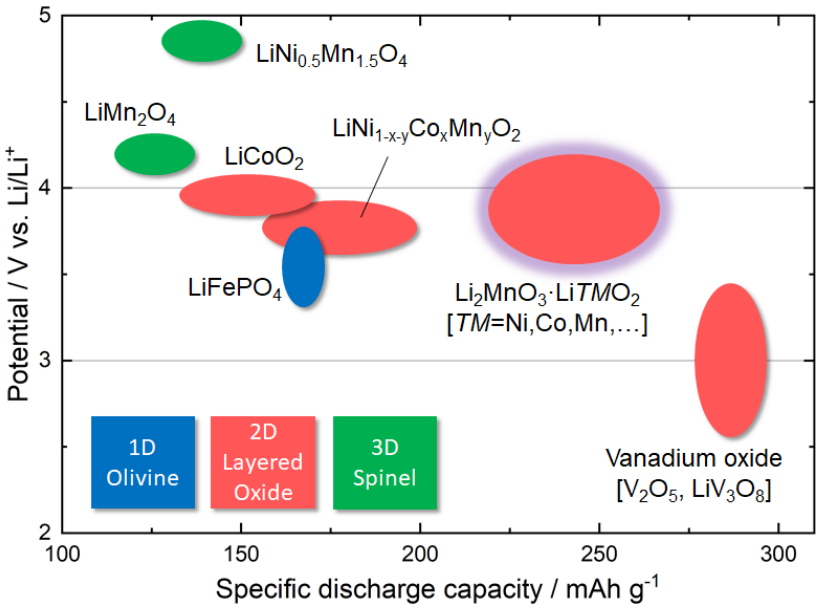

Figure 2.2.: Overview regarding the electrochemical properties and the structure of a selection of various Li ion battery cathode materials. Based on [26].

port channels of different dimensionality: The 1D olivine, the 2D layered oxide, and the 3D spinel materials. The Li*TM*O_2-type NCM (*TM*=Ni,Co,Mn) layered oxides are the state of the art Li ion cathode materials revealing higher reversible charge and discharge capacities than $LiCoO_2$ together with improved safety and lower costs. It is apparent that the Li- and Mn-rich materials (highlighted in purple) exhibit even higher energy densities (nominal voltage multiplied by specific capacity) and are therefore attractive for applications where batteries high in energy density are required. For this reason, they are often termed 'high energy' NCM cathodes (HE-NCM). Furthermore, this material composition exhibits a high manganese content, which is more abundant than nickel and cobalt. Therefore it is suitable for the utilization in high-volume and cost sensitive product segments, for instance, the automotive industry.

Li- and Mn-rich NCM cathode materials are described as solid solutions between x Li_2MnO_3 and (1-x) Li*TM*O_2 (*TM*=Ni,Co,Mn) [29, 30]. The corresponding unit cells of these end members are illustrated in Figure 2.3 and are now discussed in detail. As summarized in Table 2.1, the Li*TM*O_2-type layered oxide crystallizes in the trigonal α-$NaFeO_2$-type structure with space group $R\bar{3}m$, in which the octahedral sites of a slightly distorted cubic close packed (ccp) oxygen sublattice with an ABC stacking sequence (O3-type) are alternately occupied by transition metal ions (3a crystallographic site, TM layer) and lithium ions (3b crystallographic site, Li layer) [31]. This occupation sequence leads to a layered-type cation ordering and a slight rhombohedral distortion of the oxygen sublattice, due to the different bond lengths between Li-O and TM-O.

Table 2.1.: Basis of the unit cell (hexagonal axes) corresponding to the trigonal $LiCoO_2$ (Li*TM*O_2) structure (space group $R\bar{3}m$, International Tables for Crystallography number 166). a_h=2.82 Å, c_h=14.1 Å, γ_h=120° [32].

Atom	Wyckoff	x	y	z	Occupancy
Co	3a	0	0	0	1
Li	3b	0	0	0.5	1
O	6c	0	0	0.258	1

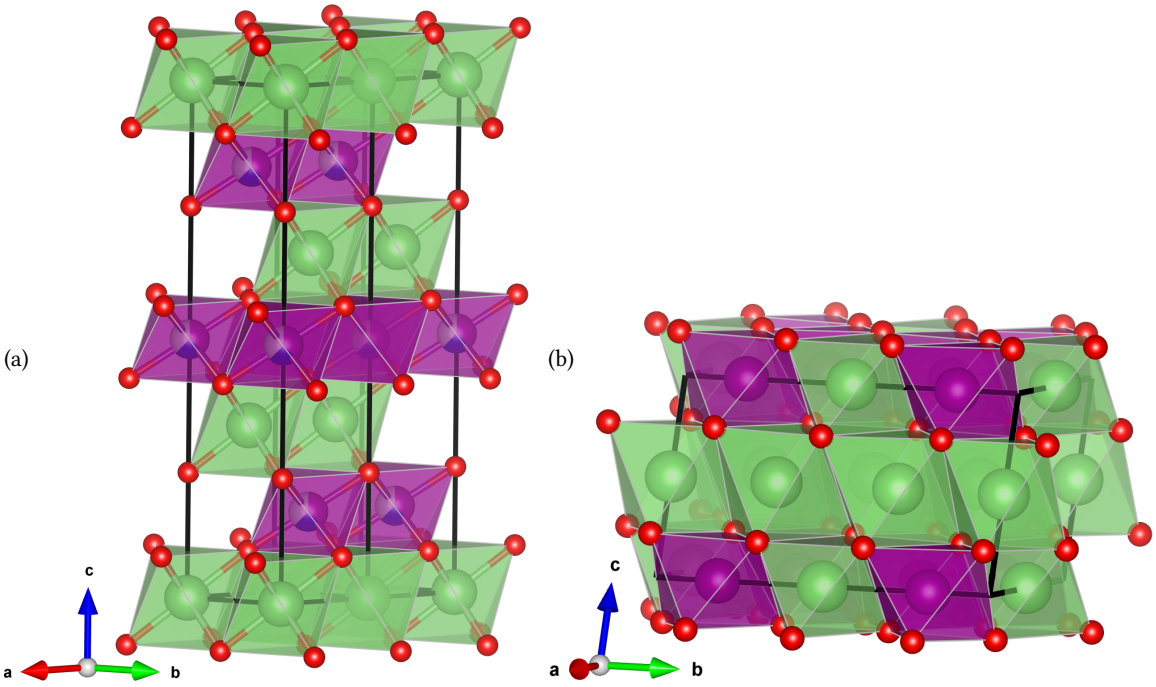

Figure 2.3.: Unit cells of (a) layered $LiNi_{0.375}Co_{0.25}Mn_{0.375}O_2$ ($R\bar{3}m$) and (b) monoclinic Li_2MnO_3 ($C2/m$). TM-O_6 octahedra in purple, Li-O_6 octahedra in green, oxygen atoms in red. Drawn in Vesta [33].

Table 2.2.: Basis of the monoclinic Li_2MnO_3 unit cell (space group $C2/m$, International Tables for Crystallography number 12). a_m=4.937 Å, b_m=8.532 Å, c_m=5.030 Å, β_m=109.46° [34].

Atom	Wyckoff	x	y	z	Occupancy
Li1	2b	0	0.5	0	1
Li2	2c	0	0	0.5	1
Mn	4g	0	0.16708	0	1
Li3	4h	0	0.6606	0.5	1
O1	4j	0.2189	0	0.2273	1
O2	8h	0.2540	0.32119	0.2233	1

The monoclinic Li_2MnO_3 with space group $C2/m$ (see Table 2.2) is structurally closely related to the $R\bar{3}m$ symmetry described above. It also possesses a slightly (now monoclinic) distorted ccp oxygen sublattice, but exhibits a modified cation composition and ordering. The alternative notation $Li[Li_{1/3}Mn_{2/3}]O_2$ already illustrates the partial substitution of Mn with Li in the TM layers in comparison to the pure $LiTMO_2$-type structure. Due to the rather high difference of the oxidation states of Li(+I) and Mn(+IV) and the corresponding ion radii of 0.74 Å and 0.54 Å [35], an in-plane Li-TM_6 'honeycomb' order forms within the TM layers in order to minimize the lattice strain [36], as illustrated in Figure 2.4. The periodic stacking of these well-ordered layers along the c axis leads to a lowering of the crystal symmetry (superstructure), either to the $P3_112$ symmetry[1] by creating a threefold screw axis or to the most common $C2/m$ symmetry by generating mirror planes along c, respectively [37]. This reduction of symmetry leads to the occurrence of additional superstructure reflections in the X-ray diffraction pattern, which are prominently emerging at low 2θ angles. The presence of these additional reflections is a strong indicator for the structural integrity of the honeycomb order on a long-range scale and will be used as such in the upcoming investigations.

The Li_2MnO_3 cathode materials typically come along with deviations from this ideal stacking sequence, i.e. stacking faults are introduced [37, 38]. These stacking faults are crucially influencing the electrochemical properties, in particular the extractable amount of Li per formula unit and therefore the accessible charge/discharge capacities, which are usually increasing with higher stacking fault density. The density of lattice defects can be tuned, for instance, by varying the synthesis temperature [39, 40]. However, pure Li_2MnO_3 as cathode material suffers from a poor reversible cyclability and the initially high charge capacities (>350 mAh/g) are not recovered in the subsequent discharge step, which makes it unattractive for commercial applications. This rapid degradation of the electrochemical properties can be explained by a profound modification of the structure during the first charge, including the loss of active Li sites [41].

[1] International Tables for Crystallography number 141

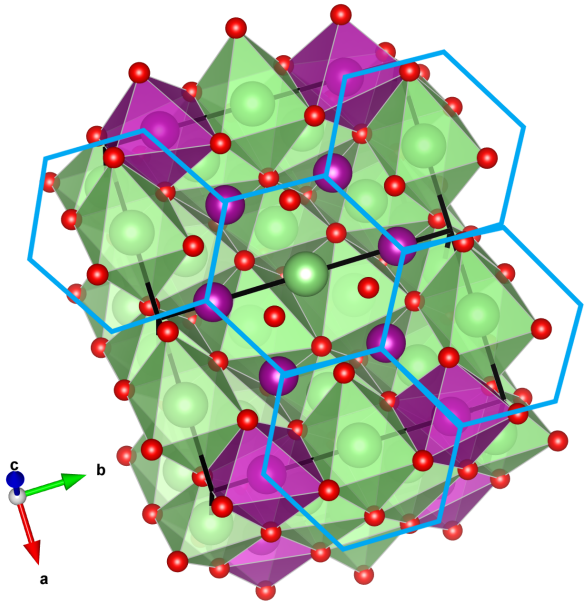

Figure 2.4.: Li-Mn_6 honeycomb ordering in the transition metal layer of monoclinic Li_2MnO_3. Mn-O_6 octahedra in purple, Li-O_6 octahedra in green, oxygen atoms in red.

It has been shown that the initially high capacity and the structural integrity of Li_2MnO_3 can be maintained to a large extend by the admixture of Li*TM*O_2 (*TM*=Ni,Co,Mn) [1, 42], i.e. the formation of solid solutions between these end members. In these single-phase solid solutions, the Li-TM_6 honeycomb ordering is not fully developed, due to the lower resulting Li:TM-ratio in the TM layers. This leads to a mixed Li/TM-TM_6-type honeycomb ordering within the TM layers, i.e. not all centers of the TM_6 honeycombs are occupied by Li ions. The here studied $Li[Li_{0.2}Ni_{0.15}Co_{0.1}Mn_{0.55}]O_2$ composition, for instance, possesses a Li:TM-ratio in the TM layers of 1:4 in comparison to 1:2 for pure Li_2MnO_3. Nevertheless, the formation of a long-range ordering (including stacking along *c*) is also present in Li_2MnO_3-based NCM solid solutions and hence the occurrence of additional superstructure reflections in the X-ray diffraction pattern. However, these reflections are now attenuated in intensity.

In contrast to the picture of the formation of solid solutions between the end members Li_2MnO_3 and Li*TM*O_2, which has been described so far there are other publications that claim to have found evidence for a composite material, in which domains of Li_2MnO_3 are finely dispersed within a $R\bar{3}m$ matrix [43, 44, 45, 46]. It could be shown that the size of these domains strongly depends on the synthesis route/conditions as well as on the composition itself [44, 47]. The non-conformance in literature regarding the description of the micro-/nanostructure of Li- and Mn-rich layered

oxides might be due to slight differences in the individually prepared materials, for instance, the composition, the synthesis route as well as the temperature profile during heating. However, based on findings from electron microscopic and spectroscopic investigations a single-phased solid solution is suggested for the commercially available TODA HE5050 Li- and Mn-rich NCM cathode material, which was also used in this work [29]. Therefore, the single phase model will be adopted for the hereinafter conducted analysis and discussion of the obtained results, respectively. A more detailed discussion regarding the structural analysis of the long- (diffraction) and short-range (NMR) atomic ordering and the correlation with electrochemical features will be carried out in Sections 5.1.2 and 5.1.3. This also includes a comparison of the features with the end members, in order to highlight the special characteristics of the solid solution 'combinations' of Li_2MnO_3 and $LiTMO_2$.

As already emphasized in the motivation of this work, the very-local 'de'-arrangement of the initially well-ordered cations plays a crucial role for the electrochemical features of the Li- and Mn-rich NCM cathode materials. These structural modifications can be either reversible, for instance represented by the electrochemical hysteresis or irreversible, like the initial formation or the voltage fade. The continuous cycling with high degrees of delithiation leads to a gradual structural transformation towards a cubic crystal symmetry. One possible 'end state' cation arrangement scenario in the ccp oxygen sublattice is the cubic spinel-type cation ordering, for example represented by the $LiMn_2O_4$ spinel ($Fd\bar{3}m$). The unit cell of this spinel is illustrated in Figure 2.5. As apparent from Table 2.3, Mn is occupying the octahedral 16*d* crystallographic site, which represents half of the available octahedral sites in the oxygen framework. The arrangement of Mn in the cubic spinel structure

Table 2.3.: Basis of the cubic $LiMn_2O_4$ spinel unit cell, origin choice 2 (space group $Fd\bar{3}m$, International Tables for Crystallography number 227). a_s=8.2383 Å, [48]. The 16*c* site is vacant in the pristine state, but can be occupied by Li via electrochemical insertion.

Atom	Wyckoff	x	y	z	Occupancy
Li1	8*a*	0.125	0.125	0.125	1
Li2	16*c*	0	0	0	0
Mn	16*d*	0.5	0.5	0.5	1
O	32*e*	0	0	0.263	1

occurs in a three-dimensional manner without a clear cation separation in TM and Li layers (2D), respectively. The tetrahedral 8*a* site is occupied by lithium and as already indicated in Table 2.3 lithium can also occupy the empty octahedral sites (16*c* site), for instance in electrochemically overlithiated $Li_{1+x}Mn_2O_4$ and $Li_{1+x}Ni_{0.5}Mn_{1.5}O_4$ spinels [49, 50, 51, 52, 53]. The electrochemically induced overlithiation results in a two-phase transition from cubic spinel ($Fd\bar{3}m$) to a tetragonal symmetry ($I4_1/amd$)[2], which can be observed by a flat voltage profile (plateau) around 3.0 V in the electrochemical data. The tetragonal distortion of the crystal lattice originates from the reduction of manganese from +IV to +III and the thereof resulting anisotropic Jahn-Teller distortion of the TM-O_6 octahedra.

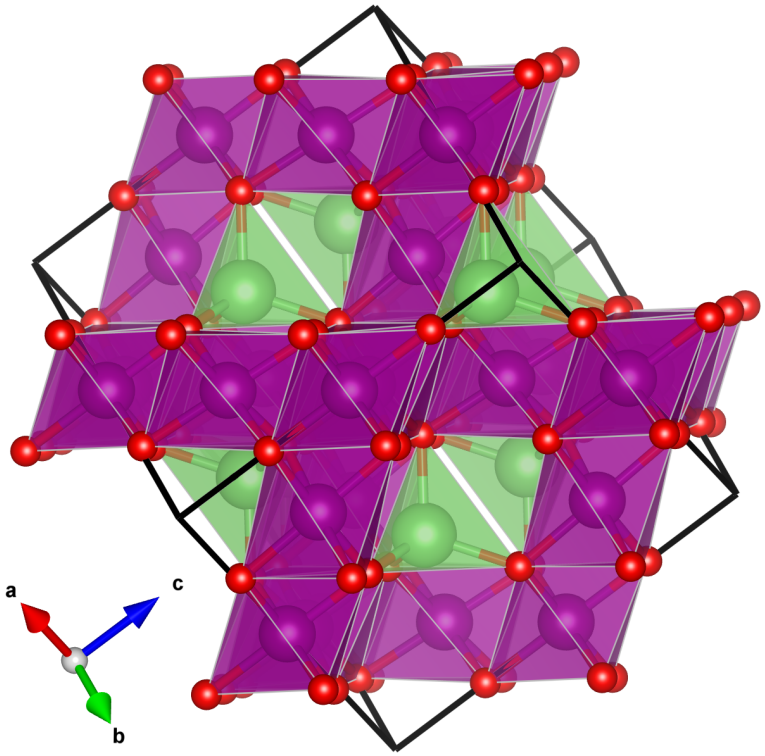

Figure 2.5.: Unit cell of cubic $LiMn_2O_4$ spinel ($Fd\bar{3}m$). Mn-O_6 octahedra in purple, Li-O_4 tetrahedra in green, oxygen atoms in red.

The spinel-type cation ordering can also be derived from a half-lithiated layered $Li_{0.5}TMO_2$-type oxide by the migration of 1/4 of the TM ions from the TM layers to the Li layers in combination with the migration of Li ions from octahedral into tetrahedral sites. These migration processes are likely occurring in layered oxide cathode materials during long-term electrochemical cycling or can be

[2]International Tables for Crystallography number 141

induced by heating of (partially) electrochemically delithiated states. For the Li- and Mn-rich NCM cathode materials, this transformation towards a cubic spinel-type cation arrangement requires the densification of the crystal lattice, which includes the release of oxygen from the surface and the migration of Mn and Li ions from the surface into the bulk, respectively. The densification is mandatory in order to remove excess oxygen and to reoccupy Li_{TM} sites, which were introduced by the Li_2MnO_3 'component' and is demonstrated by Equation 2.1

$$Li_{0.4}TM_{0.8}O_2 \xrightarrow{\text{Densification}} 0.2O_2 \uparrow + Li_{0.4}TM_{0.8}O_{1.6} \text{ (i.e. } LiTM_2O_4\text{)}. \tag{2.1}$$

This leads to a decrease of the O/TM ratio from 2.5 for the Li- and Mn-rich NCM material to 2, which can be either dedicated to a layered $LiTMO_2$-type structure or to a cubic $LiTM_2O_4$-type spinel, respectively.

2.3. Terminologies of the electrochemical analysis

Full cell setup: A full cell Li ion battery is characterized by an *in operando* design of the battery cell close to the real application, for example with a graphite anode and $LiCoO_2$ cathode. The cell potential is determined by the (open circuit) potential difference between the cathode and anode material.

Half cell setup: In a half cell Li ion battery, an anode or cathode material is cycled against a lithium metal counter electrode in order to focus the electrochemical investigations on the material to be examined. The cell potential is determined by the (open circuit) potential difference between the inserted anode/cathode and the Li potential. In this work, the half cell setup is used for all experiments.

dQ/dV plot: The differential capacity plot represents the first derivative of the galvanostatic curve against the cell voltage. This type of plot emphasizes the single redox processes occurring during charging and discharging.

Galvanostatic cycling: In this type of electrochemical characterization method the battery cell is cycled between an upper (end of charge) and a lower (end of dicharge) cut-off voltage with a constant current (CC).

C-rate: The C-rate describes the ratio between the applied (specific) current and the (specific) capacity of a battery cell and thus points to the expected duration for charge/discharge of a battery cell. For example, a battery with a capacity of 1 Ah and an applied current of 2 A will be charged/discharged in half an hour. However, at very high rates the extractable/inserted capacity is significantly lower than for lower rates due to kinetic reasons.

Specific capacity/energy: The specific capacity and energy describes the extractable charge/energy per unit mass (gravimetric) or volume (volumetric) related to a complete battery cell including passive components (cell casing, current collectors, electrode additives, etc.) or a single active component, e.g. the anode and cathode material. In this work, the specific numbers are always related to the active material only.

SEI: The solid electrolyte interphase (SEI) describes the passivation layer on the active material particles, which is composed of reaction products from the electrolyte with the active material and is predominantly formed during the first cycle (formation). This layer is (ideally) permeable for Li ions and electronically insulating, which prevents a further decomposition of the electrolyte. The SEI formation is very prominently occurring on the anode and its integrity is crucial for the

long-term cyclability of a Li ion battery. However, due to crack formation in the SEI or the diffusion of transition metals from the cathode to the anode (TMs act as catalysts), a further growth of the SEI is facilitated. Thus, more and more Li ions are trapped in the SEI leading to loss of capacity and increased SEI thickness leads to a rise of the internal cell resistance. The respective SEI on the cathode side is termed cathode electrolyte interphase (CEI).

Formation: The first electrochemical cycle of a Li ion battery typically presents a slightly different voltage profile as well as a low coulombic efficiency (discharge capacity divided by charge capacity). This can be attributed to the formation of a SEI and a CEI when the electrolyte is in a unstable voltage range during charging/discharging and is simultaneously accessible to electrons at the electrodes. During a charge step, the electrolyte decomposes and precipitates at low potentials (reduction) on the anode and at high potential on cathode (oxidation). These processes are also 'consuming' Li ions, which are irreversibly trapped in these interphases and thus are not longer accessible for the energy storage process (loss of capacity). In addition, the active materials itself (anode and cathode) can feature an irreversible structural modification in the first cycle, which leads to different voltage profiles and charge/discharge capacities in the following cycles. In this work, the majority of the observed features in the formation cycle can be attributed to structural changes in the investigated cathode materials, since lost Li ions can be reintroduced by the oversized Li reservoir on the anode side (lithium metal).

Electrochemical hysteresis: The electrochemical hysteresis describes the path dependency of the electrode/cell potential, i.e. the difference of the potential during charge and discharge. Similar to the magnetic hysteresis, the electrochemical hysteresis leads to a loss of (electrical) energy in each charge/discharge cycle. The hysteresis can be rate-dependent, e.g. due to ohmic losses (polarization), and/or rather rate-independent, e.g. due to reversible structural changes (structural hysteresis).

***ex situ* measurements:** This type of measurement procedure describes, for instance, the structural characterization of a cathode sample outside the location of operation (battery cell). In order to study the structural changes, for example induced by charging, the sample needs to be extracted from the cell case. In contrast, *in situ* measurements are conducted while changing the physical condition(s), e.g. cell voltage and temperature. These studies are often carried out in customized environments in order to obtain ideal measurement conditions and are not fully representing the real operating conditions (*in operando*). In this work, all experiments are executed *ex situ*.

3. Scope of work

The primary objective of this work is the correlation of the electrochemical features with modifications the in short- and long-range atomic ordering in the studied Li- and Mn-rich cathode material. Of great interest are in particular the order-disorder transition in the initial formation cycle, the reinstallation of a well-ordered state by heating of lithiated samples (discharged) as well as the cation rearrangement towards a more cubic spinel-type symmetry in electrochemically and thermally fatigued samples (heating of a delithiated state). In the following, the tasks of this work are briefly summarized.

Order-disorder transition during formation: The electrochemical features regarding the first cycle (formation) of the Li- and Mn-rich 50:50 material ($Li_{1.2}Ni_{0.15}Co_{0.1}Mn_{0.55}O_2$) was studied in detail and compared with its end members Li_2MnO_3 and NCM as well as a 30:70 solid solution. For the structural characterization, samples with selected charge/discharge states along the voltage profile of the first cycle were prepared and analyzed *ex situ* by X-ray powder diffraction (XRPD) including Rietveld refinement of the obtained diffraction patterns and ^{6}Li MAS NMR spectroscopy. In order to obtain high quality ^{6}Li NMR spectra the samples were self-synthesized and enriched with the ^{6}Li isotope. The results are presented in Section 5.1.

Thermal treatment of samples after formation in various states of charge: In this work package, the impact of a mild thermal treatment on highly defective metastable materials (after formation) in three charging states, 2.0 V - 4.2 V - 4.7 V, was carried out, respectively. Thereby, the temperature was varied from 150 °C to 300 °C. The structural changes were studied by synchrotron radiation powder diffraction (SRPD) including Rietveld refinement of the obtained diffraction patterns and ^{7}Li MAS NMR spectroscopy, and finally correlated with the modified electrochemical properties. Here, the commercial 'HE5050' material (TODA) was chosen due to the high amount of samples needed for the experiments and the higher cycling stability of the commercial cathode material, respectively. It possesses the same nominal composition as the self synthesized 50:50 material. The results are presented in Sections 5.2-5.4.

Thermal treatment of samples of electrochemically fatigued samples: In the introductory experiment (see Chapter 1) it could be emphasized that the voltage fade present in a highly cycled sample can be reversed by a thermal treatment. In order to obtain a more detailed insight into the degradation processes during cycling as well as into the reordering processes during heating, the structural changes after 300 cycles and after the heat treatment were studied using SRPD and ^{7}Li MAS NMR spectroscopy and correlated with the corresponding electrochemical data. The results are presented in Section 5.5.

Mass loss of cathodes during heating: In order to track the thermal stability and a potential oxygen loss of the cathode materials during heating, thermogravimetric analysis (TGA) was performed on samples at different charging states. Furthermore, the determined mass loss of the electrodes in the listed heating experiments above was evaluated and an estimation of the released amount of oxygen from the cathode was carried out. The results are presented in Section 5.6.

Scannung electron microscopy: Thermally treated cathodes were analyzed regarding alterations of their particle surface or morphology. Therefore, scanning electron microscopy (SEM) images of a pristine 'HE5050' electrode as well as of electrodes after heating and post thermal cycling were taken. Since a significant dissolution of TMs from the surface of the heated electrodes was expected during the post thermal cycles, SEM and energy-dispersive X-ray spectroscopy (EDX) were conducted on the respective lithium metal anodes used for these cycles. The results are presented in Section 5.7.

X-ray absorption spectroscopy: Finally, the local geometric and electronic structure was investigated in detail using hard and soft X-ray absorption spectroscopy. Therefore, the modifications after formation and after the thermal treatment process were monitored at the transition metal and the oxygen K-edges. Furthermore, radial distribution functions (RDF) of the investigated elements were derived from the EXAFS oscillations. The results are presented in Section 5.8.

4. Experimental

4.1. Synthesis of ^{6}Li-enriched layered oxide cathode materials

^{6}Li-enriched pure Li_2MnO_3 and NCM ('323'-ratio, $LiNi_{0.375}Co_{0.25}Mn_{0.375}O_2$) cathode materials as well as their 50:50[1] ($Li_{1.2}Ni_{0.15}Co_{0.1}Mn_{0.55}O_2$) and 30:70[2] ($Li_{1.13}Ni_{0.228}Co_{0.152}Mn_{0.489}O_2$) solid solutions were synthesized using a sol-gel method inspired by the synthesis route from Xu et al. [54]. The procedure was carried out as follows: citric acid monohydrate (≥99%, VWR) as chelating agent was dissolved in type-1 ultrapure water while constantly stirring. Lithium, nickel (≥98%, Aldrich), cobalt (≥98%, Alfa Aesar) and manganese (≥99%, Aldrich) acetate precursors were added according to the intended stoichiometric composition. The concentration of the citric acid solution was 0.5 mol/L, the molar ratio of citric acid to metal ions 1.5:1, respectively. The ^{6}Li acetate precursor was prepared from 95 at.-% ^{6}Li-enriched lithium metal chunks (Aldrich). The metal chunks were dissolved in ultrapure water and an excess amount of acetic acid was added to the solution. Then, the solvents were evaporated using a rotary evaporator until a white lithium acetate powder was obtained. The powder was further dried under vacuum conditions at 120 °C for 24 h and stored in a dry argon atmosphere afterwards.

After dissolving the acetates, the pH value of the solution was adjusted to 7.0 via the addition of aqueous ammonia. Excess water was evaporated while stirring continuously at 80 °C, until a viscous gel was obtained. This gel was transferred to a porcelain ceramic evaporating dish and was further dried at 120 °C in a muffle furnace (L5/12, Nabertherm) for 12 h. Afterwards, the gel was calcined in air at 450 °C for 6 h (+1 h heat-up time, ≅ 7 K/min) in a muffle furnace (L5/12, Nabertherm) in order to remove the organic species. The cooldown occurred without further control of the temperature by turning off the furnace. Then the precursor powder was ground in a mortar, filled into an alumina crucible and finally tempered in a tube furnace (CTF18/300, Carbolite) at 900 °C for 12 h (+5 h heat-up time ≅ 3 K/min) in a continuous stream of oxygen gas.

[1] Equal to $0.5Li_2MnO_3 \cdot 0.5$NCM323.

[2] Equal to $0.3Li_2MnO_3 \cdot 0.7$NCM323

The cooldown-rate was adjusted to 3 K/min until a temperature of 450 °C was reached; below the cooldown occurred without further control. The '6-Li_2MnO_3' active material powder was directly used after the 450 °C step in order to enhance the electrochemical properties. A high structural defect density typically increases the amount of electrochemically extractable lithium [39, 40]. The typical batch size was 8 g of active material product and all active material powders were used as received. The final cation stoichiometries were determined using ICP-OES (inductively coupled plasma - optical emission spectrometry). The results are shown in Table B.1 and confirmed the expected values within the range of error. For clarity, all materials and their compositions used in this work are summarized in Table 4.1.

Table 4.1.: Overview table of the materials and their compositions used in this work.

Abbreviation	Composition	Source	Comments
6-50:50	$Li_{1.2}Ni_{0.15}Co_{0.1}Mn_{0.55}O_2$	self-synthesized	95 at.-% ^{6}Li-enriched
HE5050	$Li_{1.2}Ni_{0.15}Co_{0.1}Mn_{0.55}O_2$	TODA America	
6-Li_2MnO_3	Li_2MnO_3	self-synthesized	95 at.-% ^{6}Li-enriched
6-NCM	$LiNi_{0.375}Co_{0.25}Mn_{0.375}O_2$	self-synthesized	95 at.-% ^{6}Li-enriched
6-30:70	$Li_{1.13}Ni_{0.228}Co_{0.152}Mn_{0.489}O_2$	self-synthesized	95 at.-% ^{6}Li-enriched
LMO	$LiMn_2O_4$	Aldrich	spinel
LNMO	$LiNi_{0.5}Mn_{1.5}O_4$	Aldrich	spinel

4.2. Electrochemical characterization and thermal treatment

For the preparation of the cathode electrode sheets, a *N*-Methyl-2-pyrrolidone (NMP)-based slurry of 87% (w/w) active material (AM), 7% (w/w) polyvinylidene fluoride as binder (PVDF, Solvay Solef 5130) and 6% (w/w) carbon black as conductive agent (CB, Timcal Super C65) was prepared as follows: The active material and carbon black were ground in acetone, until a homogeneous slurry was obtained. Then, the slurry was dried and the residual powder was added to a 4.11% (w/w) PVDF-NMP solution. This slurry was stirred on a magnetic stirrer at approximately 1000 rpm for 1 h. Afterwards, the slurry was die-coated on an aluminum foil, dried overnight at 80 °C and calendered to a coating thickness of about 30 µm (approx. 5 mg/cm² active material).
The electrochemical characterization was carried out in CR2032-type coin cells, assembled in an argon-filled glovebox (O_2 < 5 ppm, H_2O < 5 ppm) using ∅ 12 mm electrode sheets, two layers

of Celgard 2325 as separator, 150 µL electrolyte and a 250 µm thick lithium foil as anode (99.9%, MTI). The electrolyte (LP 30, BASF) was composed of 1 M lithium hexafluorophosphate ($LiPF_6$) conducting salt in a 1:1 (w/w) solution of ethylene carbonate (EC) and dimethyl carbonate (DMC). The cells containing ^{6}Li cathodes were prepared with a ^{6}Li-enriched electrolyte and lithium anode, respectively. Therefore, a 1 M electrolyte solution was prepared with $^6LiPF_6$ (98%, 95 at.-% ^{6}Li, Aldrich) in a 1:1 (w/w) solution of EC/DMC (BASF). ^{6}Li anodes were prepared from ^{6}Li-metal chunks (95 at.-% ^{6}Li, Aldrich).

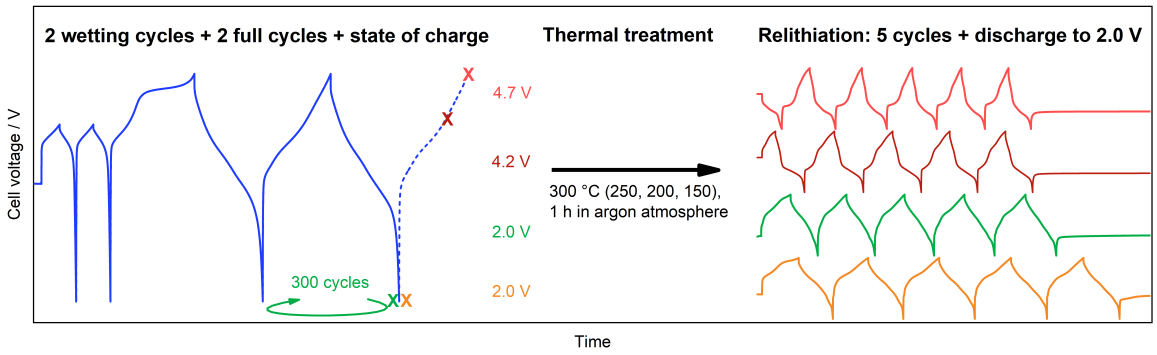

Figure 4.1.: Scheme of the electrochemical protocol and the thermal treatment procedure.

The electrochemical characterization and thermal treatment of the commercial 'HE5050' active material was carried out as illustrated in Figure 4.1. The cells were cycled first two times between 4.1 V and 2.0 V (wetting cycles), then two times between 4.7 V and 2.0 V (formation + after formation cycle) and finally adjusted to either 2.0 V (discharged/lithiated sample), 4.2 V (half charged/lithiated sample) or 4.7 V (charged/delithiated sample). All tests were carried out with a rate of C/10 (1C = 290 mAh/g) at 25 °C with a VMP3 potentiostat (BioLogic). In order to reduce the duration for the preparation of electrochemically fatigued samples, e.g. with 300 cycles, the rate was increased to C/5 after the first four cycles (2 x wetting, formation, after formation). The last two cycles were carried out in a fresh cell (new anode, electrolyte, etc.) with C/10 in order to identify the degradation features, which can be dedicated to the cathode material exclusively.
The cycled electrodes were carefully extracted from the cell stack within the glovebox and washed with dimethyl carbonate (DMC) in order to remove electrolyte residues. For the thermal treatment, the electrodes were placed in a sealable glass tube and transferred from the glovebox into a pre-heated tubular oven (Büchi B-585). The experiments were carried out at temperatures of 150 °C, 200 °C, 250 °C and 300 °C for one hour, respectively. Additionally, the glass tube was connected to

a vacuum gas manifold (Schlenk line) with a pressure relief valve in order to ensure a pressure compensation during heating. After 1 hour the glass tube was directly removed from the tubular oven and after a cool down to room temperature the samples were stored again inside the glovebox. In order to determine a potential mass loss after heating, the electrodes were weighed before as well as after the thermal treatment (the error was calculated according to the specifications of the used balance). For the post thermal electrochemical characterization (relithiation) the electrodes were once more assembled into coin cells, cycled five times and finally discharged to 2.0 V. In order to investigate the reproducibility, three samples of each combination (temperature and degree of delithiation) were electrochemically characterized. For post mortem characterization, the cathode was again extracted from the coin cell within the glovebox, rinsed with DMC and dried afterwards. The cells containing the ^{6}Li-enriched materials as well as $LiMn_2O_4$ (LMO) and $LiNi_{0.5}Mn_{1.5}O_4$ (LNMO) spinel reference materials were cycled between 4.3 V and 2.0 V (LMO), 4.8 V and 2.0 V ('6-NCM', '6-Li50:50', '6-30:70') as well as between 5.0 V and 2 V (LNMO, '6-Li_2MnO_3') for two cycles with C/50 (1C = 290 mAh/g). The samples for the post mortem characterizations (NMR, XRPD) were prepared similarly according to the aforementioned procedure.

4.3. X-ray and synchrotron radiation powder diffraction

The self-synthesized ^{6}Li materials were characterized using a STADI-P laboratory X-ray diffractometer (STOE) with a molybdenum anode (λ = 0.70932 Å), a germanium-111-monochromator and a Mythen 1K detector (Dectris). The data collection was carried out in transmission geometry using ∅ 0.5 mm glass capillaries. *Ex situ* synchrotron radiation powder diffraction (SRPD) experiments of the HE5050 samples were performed in ∅ 0.5 mm glass capillaries at the high resolution beamline P02.1 [55] at PETRA III, DESY, at about 60 keV (λ = 0.2072 Å)[3]. A 2D flat panel detector (Perkin Elmer amorphous silicon detector) with an exposure time of 60 seconds was used for obtaining the diffraction images. Fit2D [56] was used for data conversion from 2D images to 1D data points (intensity vs. scattering angle).

The Caglioti parameters (U, V, W) describing the impact of the experimental setup on the reflection profile shape and half widths were determined using a LaB_6 standard. Finally, the Rietveld

[3]Exact wavelengths used for Rietveld refinement: First beamtime in Nov. 2016: 0.207166(3) Å. Second beamtime in Oct. 2017: 0.207221(3) Å, includes the pristine and highly cycled HE5050 samples (300cyc, +heated, +relithiated).

refinements were carried out using the FullProf suite [57] (ver. 07/2017). The standard deviations of the refined parameters have been multiplied with the Bérar-Lelann factor [58]. Powder diffraction and NMR measurements were performed on the identical sample. Therefore, the electrode coating was mechanically removed from the aluminum substrate and the obtained powder was transferred into NMR rotors and glass capillaries. The preparation took place within the glovebox for the self-synthesized ^{6}Li materials and outside the glovebox for the 'HE5050' samples, respectively.

4.4. Nuclear magnetic resonance spectroscopy

Within this work, ^{6}Li as well as ^{7}Li magic angle spinning (MAS) nuclear magnetic resonance (NMR) spectroscopy were carried out for the characterization of the local lithium environments. The arguments for and against each lithium isotope regarding the resulting quality of the spectra are discussed briefly in the following. The typically very broad and featureless resonances in solid state NMR spectra can be narrowed by spinning the sample container with a high frequency inside the magnetic field (B_0). Hereby, the spinning axis is tilted by the magic angle θ_m (54.7°) with respect to the direction of B_0. However, the MAS leads to the presence of spinning sidebands in the spectra, which may overlap with the main resonances. The distance of the spinning sidebands Δ_{sb} with respect to the corresponding main resonance is given by Equation 4.1

$$\Delta_{sb} = n \cdot \frac{f_{spin}}{f_L}, \tag{4.1}$$

where n is the sideband number (± 1, 2, 3, ...), f_{spin} is the spinning frequency and f_L the Larmor frequency of the observed nucleus. When comparing the Larmor frequencies of the ^{6}Li nucleus (29.4 MHz) and the ^{7}Li nucleus (77.7 MHz) in a 4.7 T field, it is apparent that the resulting distance of the spinning sidebands is higher in the ^{6}Li spectra. A spinning frequency of 67 KHz leads to first sideband distances of ±2279 ppm (^{6}Li) and ±862 ppm (^{7}Li), respectively. Since the NMR spectra of Li-TM-O battery materials typically demonstrate a NMR shift of 0-2300 ppm [59], the ^{6}Li MAS NMR enables a better identification of the main resonances as well as a more straightforward quantitative analysis of the spectra. These theoretical considerations are clearly illustrated in Figure 4.2. However, the natural abundance of the ^{6}Li isotope is only 7.59 at.-%, requiring a ^{6}Li-enrichment of the material in order to obtain a high-resolution spectrum in an adequate amount of time (approx. 20 h). This was carried out by synthesis of ^{6}Li-enriched cathode materials and the usage of a ^{6}Li-enriched anode and electrolyte.

For ^{6}Li MAS NMR spectroscopy, a Bruker Avance 200 MHz spectrometer (4.7 T) with ∅ 1.3 mm zirconia rotors and a spinning frequency of 67 kHz was used. The experiments were performed at 283(1) K with a rotor synchronized Hahn-echo pulse sequence ($\pi/2$-τ-π-τ-acquisition, with $\tau = 1/f_{\mathrm{spin}}$), a $\pi/2$ pulse length of 0.95 µs and a recycle delay of 0.1 s at a frequency of 29.475 MHz. An aqueous 1 M ^{6}LiCl solution was used as the reference for the chemical shift (0 ppm). All spectra were normalized according to the number of scans and the sample mass. Analogously, the acquisition of the ^{7}Li spectra was carried out at a frequency of 77.82 MHz, a $\pi/2$ pulse length of 0.6 µs and a recycle delay of 0.2 s without further cooling of the probe. An aqueous 1 M LiCl solution was used as the reference for the chemical shift. In order to enhance the quantitative comparability, all measurements were carried out with the respective electrode-coating powder (active material, binder, carbon). For data processing and analysis MestreNova (ver. 6.0.2, Mestrelab Research) was used.

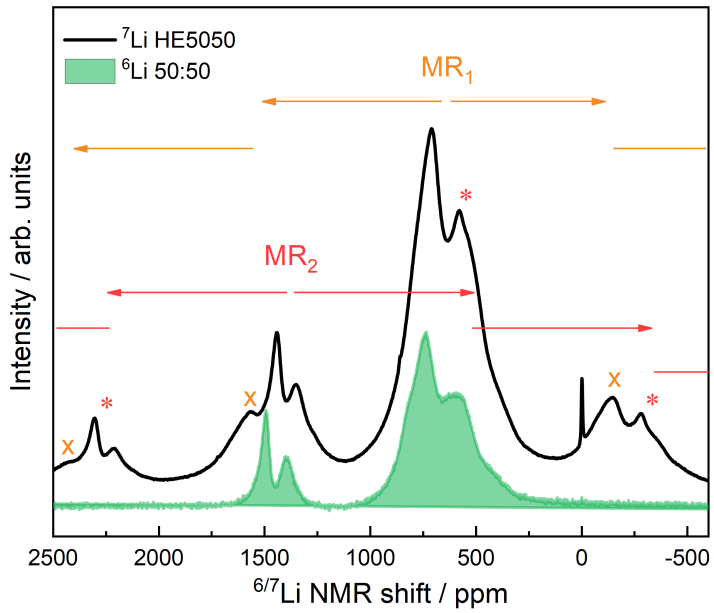

Figure 4.2.: Comparison of the ^{6}Li and ^{7}Li NMR spectra from cathode samples with the same stoichiometry ($Li_{1.2}Ni_{0.15}Co_{0.1}Mn_{0.55}O_2$), but different lithium isotope. The spinning sidebands (±861 ppm) of the ^{7}Li NMR spectrum are highlighted by the arrows. Here, the sidebands '×' belong to the main resonance group 1 (MRG_1), the sidebands '∗' to the main resonance group 2 (MRG_2), respectively. The slight shift of the ^{6}Li spectrum towards higher values can be ascribed to a lower acquisition temperature (active cooling of the probe to 283 K).

4.5. Thermogravimetric analysis

Thermogravimetric analysis (TGA) was performed using a STA Jupiter 449C thermal analyzer (Netzsch), which was set up in an argon filled glovebox. Therefore, electrode coatings of a pristine 'HE5050' sample as well as of samples after formation, charged to 2.0 V, 4.2 V and 4.7 V, respectively were mechanically removed from the aluminum substrates in argon atmosphere and packed into alumina crucibles. Afterwards, the samples were heated with 5 K/min up to 500 °C in a dynamic argon atmosphere (20 mL/min). The data processing was carried out using the Proteus Analysis software (ver. 6.0.0, Netzsch).

4.6. Scanning electron microscopy

Scanning electron microscopy (SEM) images were taken from the pristine 'HE5050' electrode as well as of the electrodes after heating and relithiation. Furthermore, the corresponding lithium anodes (used for the five relithiation cycles) were characterized using SEM and energy-dispersive X-ray spectroscopy (EDX). Therefore, a FE-SEM Merlin microscope (Carl Zeiss) with an attached Quantax XFlash 6|60 EDX spectrometer (Bruker) was used. The cathode samples were rinsed with DMC in order to remove electrolyte residues. The lithium anodes were characterized as received. All samples were placed on an adhesive carbon pad and mounted on a transfer-system, which enables the transport of the samples to the SEM within inert argon atmosphere. The SEM images were captured with the in-lens detector and the applied acceleration voltage is specified directly in the microscopy image. EDX measurements were carried out by hyper-mapping an area of approx. 1.5x1.1 mm^2. For the subsequent quantitative elementary analysis only the elements of interest (C, F, P, O, Mn, Ni, Co) were considered.

4.7. Hard and soft X-ray absorption spectroscopy

Hard X-ray absorption spectroscopy (XAS) experiments of the 'HE5050' electrode samples were carried out at the applied X-ray absorption spectroscopy beamline P65 at PETRA III, DESY. The spectra of Ni, Co and Mn K-edges were recorded in transmission mode and the reference spectrum for energy correction was simultaneously collected using the corresponding transition metal foil. The data was processed and analyzed using Athena [60] (included in the Demeter-package, ver. 0.9.25). Additionally, soft XAS measurements at the oxygen K-edge were performed at the

WERA beamline for soft X-ray spectroscopy and microscopy at the Karlsruhe synchrotron light source ANKA. The spectra were recorded using total electron yield (TEY) and fluorescence yield (FY) mode. Energy calibration (using a NiO reference), dark current subtraction, division by I_0, background subtraction and data normalization were performed.

The sample preparation was carried out as follows: In an argon filled glovebox, the samples to be characterized were rinsed with DMC to remove the electrolyte and dried. For hard XAS measurements the electrodes were placed on an adhesive Kapton tape, the aluminum substrate was removed and a second Kapton tape was placed on top. The samples used for the soft XAS experiments were kept intact, mounted on the sample holder and directly transferred to the beamline in a transfer-vessel filled with argon gas.

5. Results

5.1. Formation of Li- and Mn-rich NCMs

This section focuses on the comparison regarding the structure and electrochemical properties of the end members Li_2MnO_3 and Li*TM*O_2 (here, $LiNi_{0.375}Co_{0.25}Mn_{0.375}O_2$, '323'-ratio) as well as their solid solutions, especially the 50:50 composition ($Li_{1.2}Ni_{0.15}Co_{0.1}Mn_{0.55}O_2$). For this composition the order-disorder transition in in the first cycle (formation) is investigated in detail on the long-range atomic scale by X-ray powder diffraction (XRPD) as well as on a very-local atomic scale by ^{6}Li nuclear magnetic resonance (NMR) measurements.

5.1.1. Electrochemical characterization

Figure 5.1a shows the cell voltage vs. specific capacity plot of the initial formation cycle starting from pristine material, the cycle after formation as well as the 10th cycle of the self-synthesized ^{6}Li-enriched '6-50:50' cathode material. For a better illustration of the individual redox processes occurring during charging and discharging, the corresponding derivative of the capacity (dQ/dV) vs. cell voltage is plotted in Figure 5.1b. In the initial charge of the pristine material, the first peak with maximum value located at about 4.0 V ('NC') also found for conventional NCM cathode materials is attributed to the oxidation of the transition metal ions Ni and Co from +II/+III states to +IV [61, 62, 63, 64]. It is assumed that manganese is already in +IV in the pristine material. A charge capacity of 115 mAh/g is reached until 4.4 V, which is close to the theoretical value of 127 mAh/g under the assumption that all Ni and Co ions have been oxidized to +IV. So far, the electrochemical delithiation (charging) process can be considered to be reversible and thus the initial state can be reached again by lithiating (discharging) the material [65, 66].
The second part of the initial charge is dominated by an extended 'plateau' at 4.5 V corresponding to the so called 'formation' or 'activation' of the Li- and Mn-rich NCM, which includes the partial loss of the initial electrochemical and structural features, i.e. order-disorder transition. These

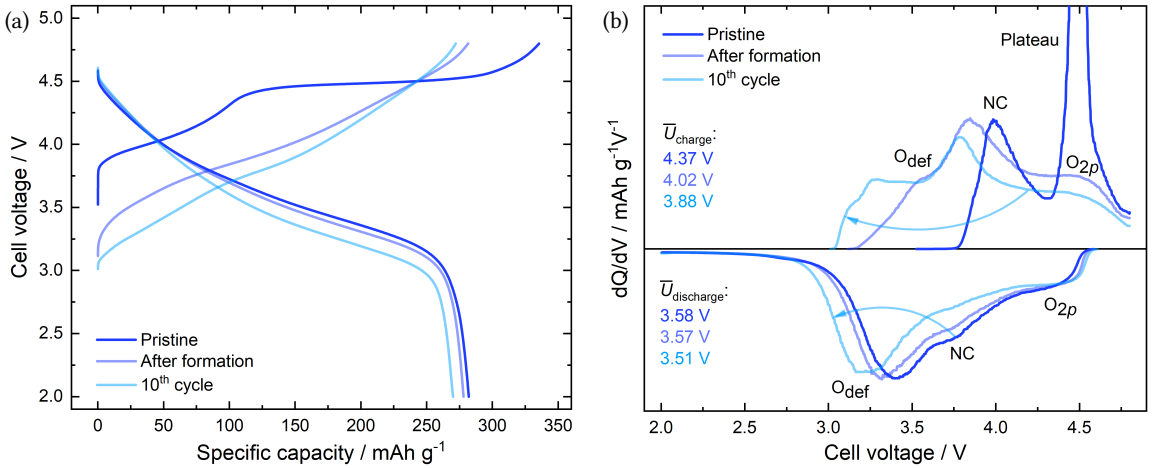

Figure 5.1.: Cell voltage vs. specific capacity (a) and the corresponding differential capacity (dQ/dV) plot (b) of the first, second and tenth cycle of the '6-50:50' cathode material cycled between 4.8 V and 2.0 V using a C/50 rate. The arrows in (b) illustrate the decay of the mean charge/discharge voltage (voltage fade). Labels: 'NC' – Ni/Co redox activity, 'O_{2p}' – oxygen 2*p* band, 'O_{def}' – defect-associated oxygen redox activity.

irreversible modifications are most clearly indicated by the absence of the 'plateau' for further charge/discharge cycles and the disappearance of the $C2/m$ superstructure reflections in the corresponding diffraction pattern as will be shown later on. Since the transition metal ions reach an oxidation state of +IV at about 4.4 V, further charge compensation during the 'plateau' is now carried out by the oxidation of the oxygen. This process is described by the reversible formation of electron holes in the oxygen 2*p* band [5, 67] as well as the irreversible partial release of oxygen from the crystal lattice, either as a gas and/or by reaction with the surrounding electrolyte especially beyond the 'plateau' >4.5 V [5, 6, 68, 69]. Overall, the first charge reaches a capacity of 335 mAh/g at 4.8 V.

Due to the irreversible structural modifications a reduction process corresponding to the 'plateau' of the initial charging is no longer identifiable. Instead, two newly occurring processes are emerging during discharge in addition to the reduction peak 'NC': i) the reduction peak at around 4.3 V, which is commonly ascribed to the annihilation of electron holes in the oxygen 2*p* band ('O2*p*'), which are formed during the 'plateau' [5, 8, 67]; and ii) the new low-voltage process at around 3.3 V, which is dedicated to a reversible anionic $O^{2-/n-}$-contribution [2, 8, 11, 70, 71]. Interestingly, this anionic redox process is exclusively appearing in the Li-rich materials and its emergence is obviously directly connected with the initial formation process, which leads to a highly defective material with

a modified electronic structure, i.e. newly formed electron energy states are occupied. Therefore, this redox process is termed defect-related oxygen contribution 'O_{def}' in this work[1]. As a concluding remark, this low-voltage process was initially ascribed to the $Mn^{3+/4+}$ redox activity in a layered $LiMnO_2$-like structure, which is supposed to form during formation [72, 73, 74, 75]. However, recent evidence disproved this mechanism, for instance, by investigating the evolution of the manganese oxidation state during the formation using X-ray absorption spectroscopy [63, 76, 77]. Based on the findings obtained in this work, a more detailed discussion on the proposed $LiMnO_2$ formation will be carried out in Chapter 6.

Af the end of discharge, a discharge capacity of 282 mAh/g at 2.0 V is reached leading to an irreversible capacity loss (1^{st} charge capacity - 1^{st} discharge capacity) of 53 mAh/g. This can be mainly attributed to the loss of electrochemically active lithium sites [4] besides 'electron-releasing' side reactions during charge, for instance, the release of oxygen. In the second charging cycle, the onset voltage of the first oxidation peak is lowered to 3.3 V. It represents the newly formed reversible anionic redox process 'O_{def}', continued by 'NC' and 'O_{2p}'. The same processes can be observed during the second discharge in reversed order. After 10 cycles, the region 'O_{def}' becomes more prominent at the expense of high-voltage region 'NC' (blue arrows) in the charge as well as in the discharge step. As can be seen from the calculated mean charge and discharge voltages provided within the dQ/dV plot, this leads to a decrease of the mean voltages with increasing number of cycles and is commonly termed as voltage fade/decay. At the same time, the discharge capacity only decreased slightly from 278 mAh/g in the cycle after formation to 270 mAh/g in the 10^{th} cycle, respectively. As will be shown later in Section 5.5, these degradation processes are directly correlated to a gradual structural transformation towards a more cubic spinel-type cation arrangement.

In order to get a more detailed picture on the electrochemical features of Li and Mn-rich NCMs, the electrochemical characterization was repeated for the pure '6-Li_2MnO_3' and '6-NCM' materials as well as a 30:70 solid solution ('6-30:70'). The results are summarized in Figure 5.2. As can be seen from the cell voltage vs. specific capacity plot of a '6-Li_2MnO_3' electrode (Figure 5.2a), the first charge starts with a strong rise of the voltage. Then, a rather long and pronounced 'plateau'

[1] It should be noted that the initial order-disorder transition might affect the entire charge compensation mechanism, due to a modified electronic structure and a clear separation of the single redox processes is rather difficult. For instance, Assat et al. [2, 8] suggested a reversible $O^{2-/n-}$ redox activity throughout the entire voltage window. However, this work focuses on the rather 'strong' modifications of the electrochemical and structural features in order to emphasize the main idea of this study and to interpret the here obtained results, respectively.

is followed until reaching the charge cut-off voltage at 5.0 V. Here, the first part of the charge up to 4.5 V can be attributed to the oxidation of residual Mn^{3+} to an oxidation state of +IV. The presence of Mn^{3+} in the pristine material can be ascribed to an oxygen deficiency, which prevents a full oxidation of manganese to +IV [78, 79]. Similar to the electrochemical curve of the '6-50:50' material after the initial formation cycle, the subsequent charge and discharge steps of '6-Li_2MnO_3' reveal a completely different progression of the voltage in comparison to the initial charge. Most interesting is the appearance of redox peaks at around 3.0/2.8 V during charge/discharge (Figure 5.2b), which are very similar to the redox activity in a $LiMn_2O_4$ spinel [80]. This observation strongly indicates a profound structural rearrangement on the 'plateau' towards a $Mn^{3+/4+}$ redox active spinel. In the literature, this process is described by an irreversible transformation towards a spinel-type cation arrangement, e.g. like in the $LiMn_3O_4$-like defect spinel [41, 81], the release of lattice oxygen [82] and the redox activity of manganese and oxygen in the post formation cycles [41, 83].

Next, the electrochemical characterization of the non Li-rich '6-NCM' (Li/TM=1) with a nominal composition of $^6LiNi_{0.375}Co_{0.25}Mn_{0.375}O_2$, is shown in Figure 5.2c+d. Here, the charge/discharge is dominated by the reversible oxidation/reduction of cobalt and nickel ('NC') as well as the formation of electron holes in the oxygen 2*p* band ('O_{2p}')[2] at high voltages. In contrast to the so far presented Li-rich materials, the formation cycle does not indicate a considerable irreversible electrochemical or structural modification of the initial state. The electrochemical characterization of the '6-30:70' cathode powder with a nominal composition of $^6Li_{1.13}Ni_{0.228}Co_{0.152}Mn_{0.489}O_2$ is shown in Figure 5.2e+f. It is apparent that the initial charging curve reveals a higher contribution of nickel and cobalt to the charge compensation ('NC') during delithiation as well as a shorter 'plateau' than the charging curve of the '6-50:50' sample. Furthermore, the corresponding dQ/dV plot demonstrates a smaller contribution of the newly formed redox process 'O_{def}' and a higher contribution of the process 'NC' in the charge and discharge step, in comparison to the '6-50:50' material. Similar to the second cycle of the '6-50:50' material, an onset of the voltage fade is already present in the second cycle as highlighted by the green arrow.

The obtained charge/discharge capacities as well as the mean charge/discharge voltages of the

[2] The formation of electron holes in the oxygen 2*p* band induces a huge mechanical stress and phase instability in 'classical' layered oxides, such as the $LiCoO_2$. This results in a strong capacity fade, e.g. induced by the formation of cracks in the particles or the release of oxygen [67]. For this reason, the end of charge voltage is set close to the end of the oxidation peak 'NC' in the commercial application.

examined materials are summarized in Figure 5.3. From graph (a) it can be seen that the initial charge capacity as well as the irreversible capacity loss increases with higher Li/TM ratios. This observation is directly related to the drop of the mean charge voltage in the second charge (after formation) in comparison to the initial charge (formation) as indicated by the green arrow in graph (b). Furthermore, also the mean voltage between charge and discharge (hysteresis) significantly increases with higher Li/TM ratios. The origin of the electrochemical hysteresis can be explained by different lithium site energies for delithiation and lithiation, respectively. Thus, a path-dependency is present, which is caused by the reversible migration of TM ions, e.g. to tetrahedral sites or former octahedral Li sites in the Li layers during charge and discharge. Therefore, the environments of the Li sites are varied continuously (structural hysteresis), which results in different site energies[3] [12, 14]. However, the structural alterations during cycling are partially irreversible leading to a gradual decrease of the Li site energies (voltage fade) and probably also of the availability of electrochemically active Li sites (capacity loss).

In summary, it can be noted that the initial capacity loss as well as the present electrochemical degradation after formation (voltage and capacity fade) is prominent in pure '6-Li_2MnO_3' and almost absent in pure '6-NCM'. However, the electrochemical properties of the '6-30:70' and '6-50:50' materials cannot be described by a simple linear combination of the according electrochemical properties of the end members '6-Li_2MnO_3' and '6-NCM'. As can be seen from a comparison of the gravimetric energy densities in Figure 5.4, the '6-50:50' sample reveals the highest charge and discharge energies in the cycle after formation. It is interesting to observe that the high energy density is significantly falling off for higher Li/TM ratios, like for the pure '6-Li_2MnO_3'. Nevertheless, the 10^{th} cycle of the '6-50:50' cathode powder already presented a clearly apparent drop of the mean charge/discharge voltages and the capacity (see Figure 5.1). These observations lead to the hypothesis that the high initial energy density is achieved at the cost of the long-term stability. The significant electrochemical and structural modifications of pure '6-Li_2MnO_3' towards a $LiMn_2O_4$-like spinel during the formation cycle are just 'postponed' in the high-energy 50:50 composition, i.e. the structure is in a metastable state. This hypothesis will be evaluated in the following sections by investigating the material's response to long-term electrochemical cycling as well as thermal treatment, respectively.

[3] Here it should be noted, that the aforementioned mechanism may overlap with a 'polarization hysteresis', e.g. due to Li ion concentration gradients and ohmic losses, especially at high current densities. By contrast, the structurally induced hysteresis in Li- and Mn-rich NCMs is also present at near-zero currents.

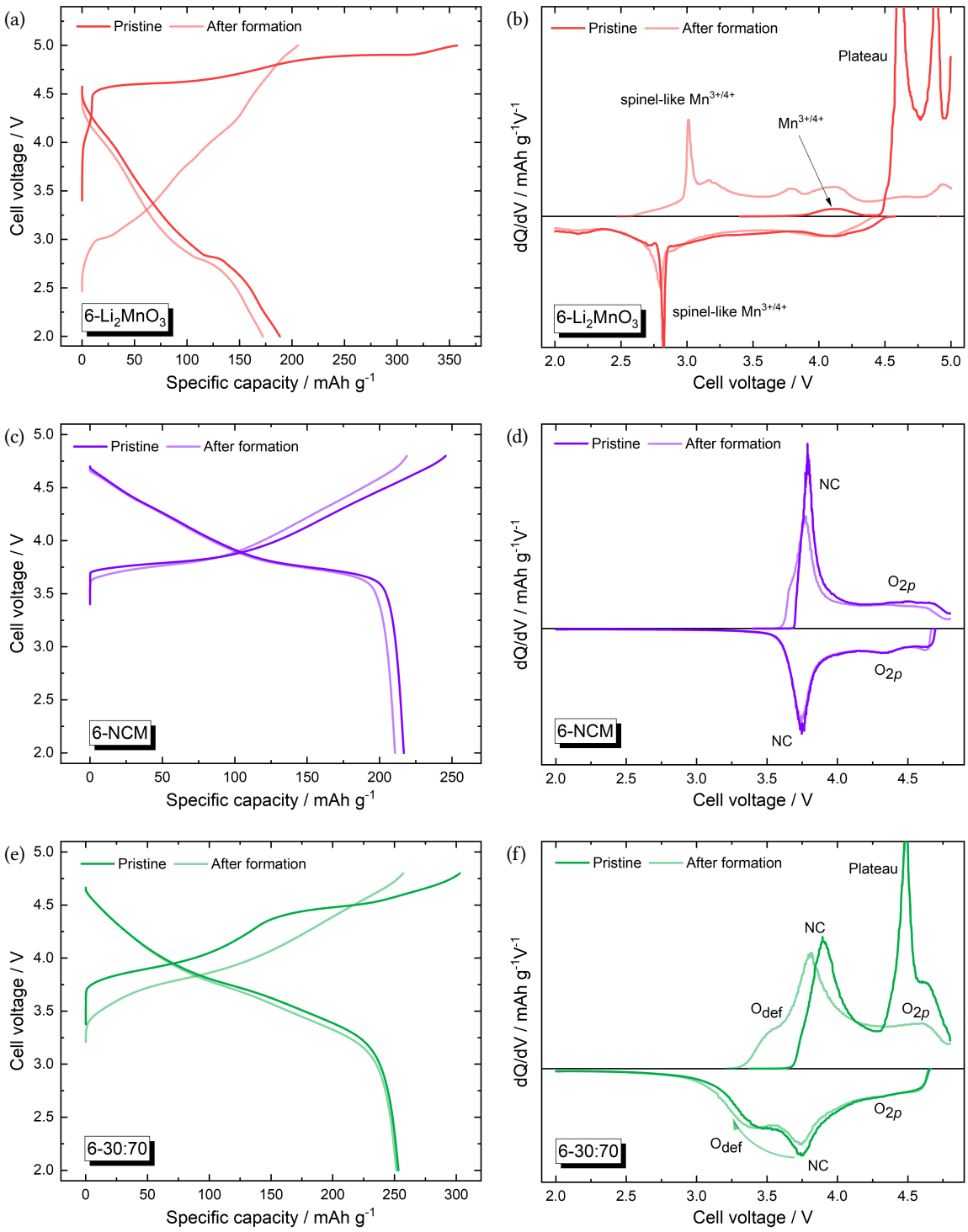

Figure 5.2.: Cell voltage vs. specific capacity (a, c, e) and the corresponding differential capacity (dQ/dV) plots (b, d, f) of the '6-Li_2MnO_3', '6-NCM' and '6-30:70' layered oxide cathode materials. Labels: 'NC' – Ni/Co redox activity, 'O_{2p}' – oxygen 2*p* band, 'O_{def}' – defect-associated oxygen redox activity.

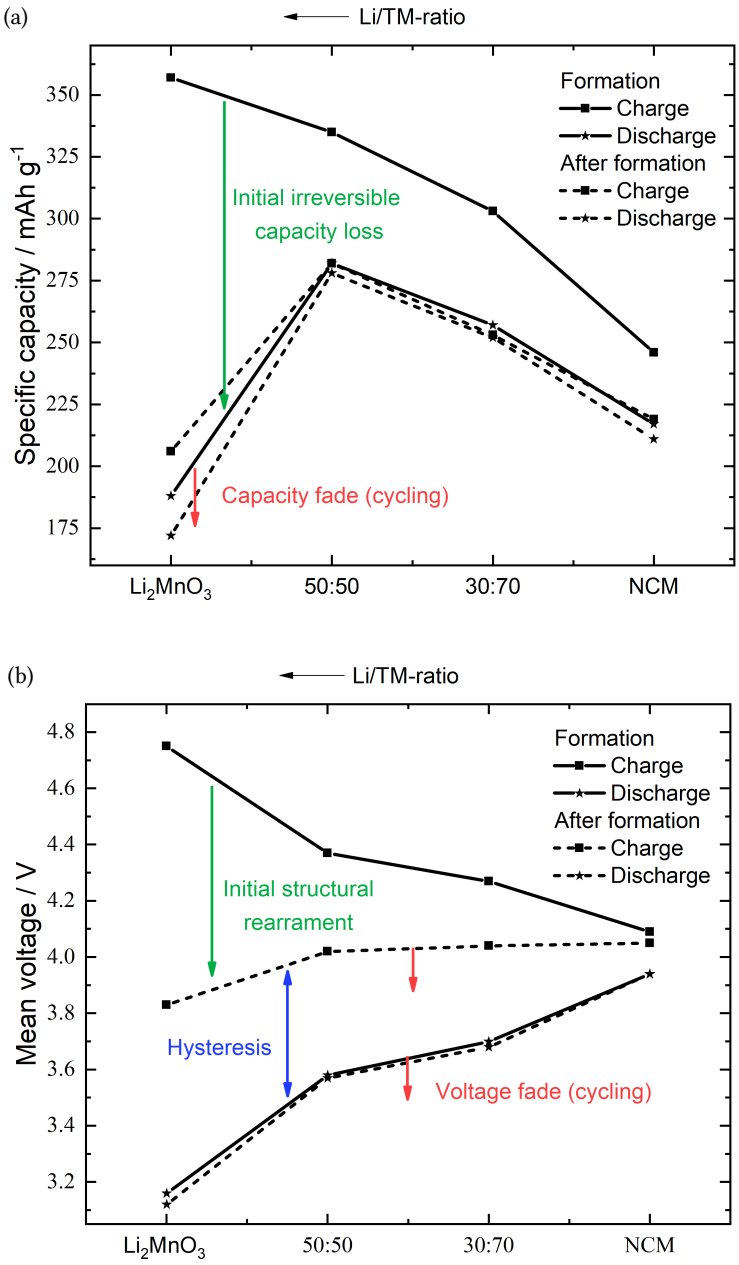

Figure 5.3.: Specific charge/discharge capacities (a) as well as the mean charge/discharge voltages (b) of the self-synthesized materials obtained from the formation cycle and the cycle after formation, respectively. Additionally, the degradation processes associated with Li- and Mn-rich materials are highlighted. The lines are inserted as a guide for the eye.

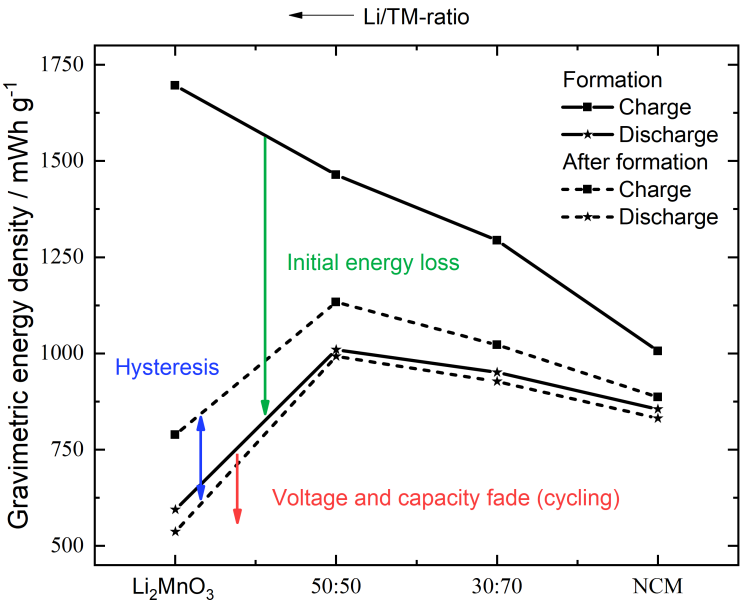

Figure 5.4.: Specific charge/discharge energies of the self-synthesized materials obtained from the formation cycle and the cycle after formation, respectively. Additionally, the degradation processes associated with Li- and Mn-rich materials are highlighted. The lines are inserted as a guide for the eye.

5.1.2. X-ray powder diffraction

Figure 5.5a shows the X-ray powder diffraction patterns of the sol-gel synthesized materials with varying composition and in particular considerably different Li/TM ratios. The pure '6-NCM' layered oxide powder (purple pattern) crystallizes in the trigonal α-$NaFeO_2$-type structure with space group $R\bar{3}m$. Here, the octahedral sites of the rhombohedrally distorted oxygen framework are alternately occupied by lithium (3*b* sites) and transition metal ions (3*a* sites) in a well separated manner as has been shown in Section 2.2. When the Li/TM ratio is greater than 1, the TM sites are partially substituted by Li ions leading to a Li/TM-TM_6-type honeycomb ordering in the TM layers and the occurrence of additional monoclinic $C2/m$ superstructure reflections. These are predominantly appearing in the low 2θ range (9-13°) as emphasized by Figure 5.5b. The intensities and the profile shapes of these reflections strongly depend on the percentage of Li ions in the TM layers, the degree of ordering within the TM layers as well as the variations in the stacking sequence (stacking faults) along the *c* axis. The latter factor leads to an asymmetric 'Warren-shaped'

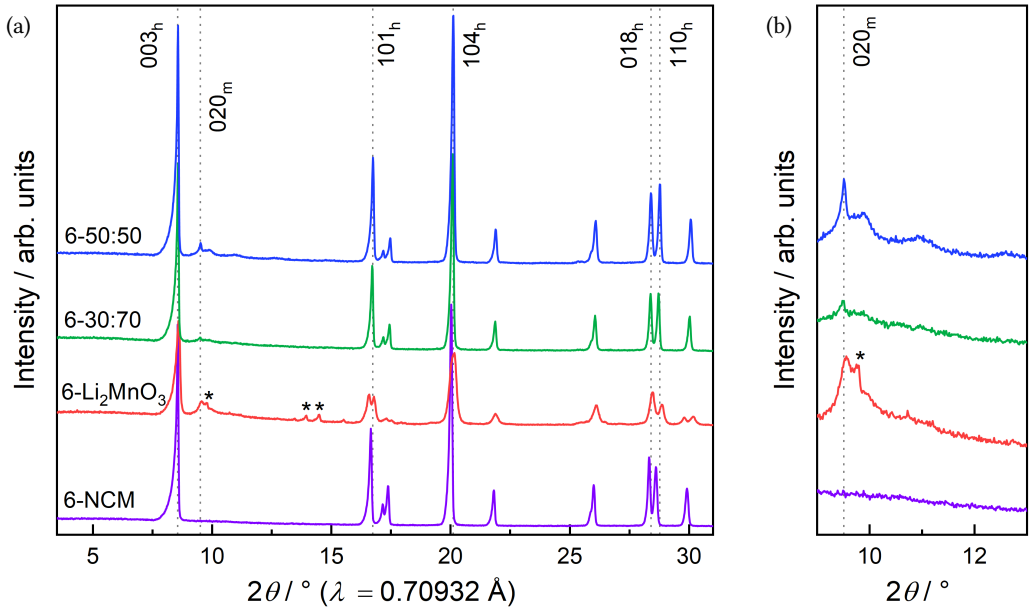

Figure 5.5.: X-ray powder diffraction patterns (a) of the '6-Li_2MnO_3' and '6-NCM' electrode powders as well as their '6-30:70' and '6-50:50' solid solutions. The $C2/m$ superstructure reflections are emphasized in (b). *Li_2CO_3-associated reflections with space group $C2/c$ (International Tables for Crystallography number 15). Reflection-subscripts: m – monoclinic setting, h – hexagonal setting.

profile broadening, with a characteristic gently sloping flank on the right side of the reflections [37, 44]. Furthermore, it is obvious that the $C2/m$ superstructure reflections are more pronounced for compositions with higher Li/TM ratios, as expected from the considerations above.
In order to follow the structural changes occurring within the initial formation cycle on a long-range atomic scale, *ex situ* X-ray diffraction patterns of electrode powders with defined charge/discharge voltages along the voltage profile of the first cycle were recorded. The results are presented in Figure 5.6. The complementary characterization of the very-local Li environment will be presented in the next section using ^{6}Li MAS NMR spectroscopy. As apparent from the first three diffraction patterns, the intensity of the $C2/m$ superstructure reflections only declines slightly until 4.4 V, indicating that the integrity of the long-range honeycomb ordering is almost unchanged. As a concluding remark, the decrease of the Li occupancy in the TM layers does not necessarily lead to a lowering of the $C2/m$ superstructure reflection intensities, since lithium does not considerably contribute to the diffraction process of X-ray radiation. The disappearance of these reflections can be rather described by a slight displacement of the TM ions and/or a change of their positions in the lattice (migration). Thus, the integrity of the long-range honeycomb ordering might not directly be affected by the removal of Li ions to a certain extend.
Furthermore, a comparison of the half widths of the neighboring reflections 018_h and 110_h indicates an increasing anisotropic lattice strain in hexagonal c direction (variations of the lattice parameter c_h). This anisotropic strain leads to a pronounced broadening of c_h-dependent reflections, e.g. the aforementioned 018_h reflection and will be verified by Rietveld refinement later on. When the cell voltage is increased above 4.4 V, the 'plateau' is present in the electrochemical data. From Figure 5.6b it is apparent that the increase of the voltage to 4.5 V leads to a significant decline of the $C/2m$ superstructure intensity and at the end of charge (4.8 V) these reflections are totally absent. As indicated by the gradual broadening of the 018_h reflection during charge, the anisotropic lattice strain increases with a higher degree of delithiation reaching a maximum at 4.8 V. During the subsequent discharge step, this reflection broadening, respectively the anisotropic strain decreases again. Most interestingly, there is no reappearance of the $C/2m$ superstructure reflections at the end of discharge, which clearly proves the irreversible loss of the long-range Li/TM-TM_6 honeycomb ordering and thus an order-disorder transition during the irreversible formation process on a long-range atomic scale. The respective post formation X-ray diffraction patterns of the end members '6-Li_2MnO_3' and '6-NCM' as well as of the '6-30:70' powder are attached in Figure C.6.

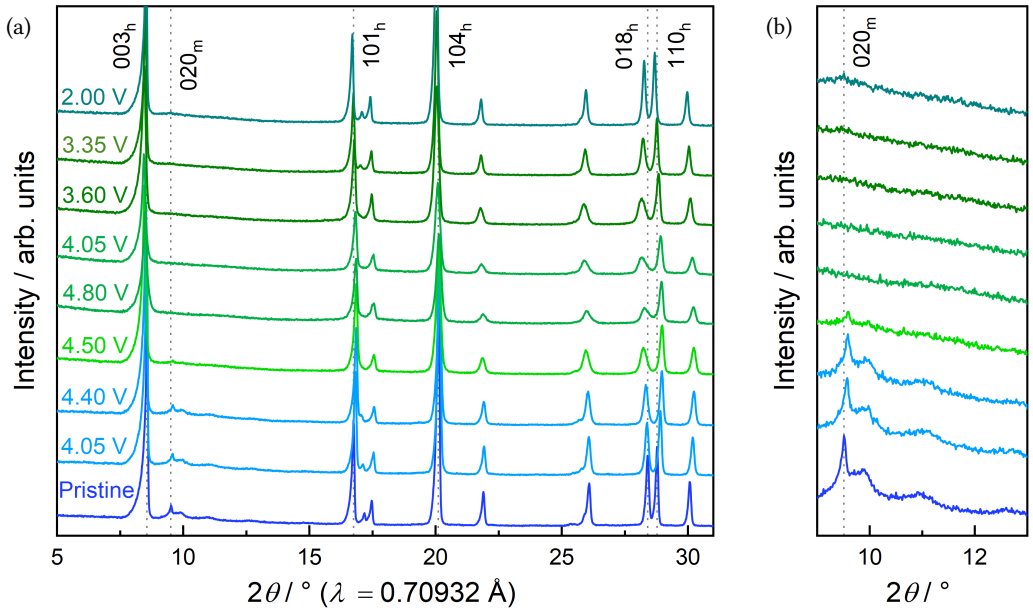

Figure 5.6.: *ex situ* X-ray powder diffraction patterns (a) of '6-50:50' electrode powders, which were charged/discharged to defined voltages along the voltage profile of the first cycle (formation). The evolution of the $C2/m$ superstructure reflections is emphasized in (b). Reflection-subscripts: m – monoclinic setting, h – hexagonal setting.

For a more detailed analysis of the diffraction data Rietveld refinement was carried out in order to follow the evolution, for instance, of the lattice parameters and the lattice strain. The results and the underlying structural model are presented in the following. Even though the diffraction pattern of the pristine '6-50:50' material clearly shows additional monoclinic $C2/m$ reflections, a structural model based on the rhombohedral $R\bar{3}m$ lattice was used for crystallographic simplicity and in order to emphasize the alteration of the refined structural parameters. This model is titled 'Model A' and is defined as follows (a summary of the atom positions and the refined parameters is shown in Table 5.1):

i) One single layered oxide $R\bar{3}m$ phase (space group 166).

ii) The starting composition was set to $Li_{1.2}Ni_{0.15}Co_{0.1}Mn_{0.55}O_2$.

iii) The lattice parameters a_h and c_h (h = hexagonal setting) as well as the z coordinate z_O of the oxygen site (6c) were refined.

iv) Depending on the state of charge, the Li occupancy was adapted according to the reached charged/discharge capacities in the electrochemical data (parameter d in Table 5.1. The determined capacity was completely attributed to lithium ion extraction/insertion,

neglecting side reactions. The Li and TM layers were delithiated equally with the same percentage.

v) The migration of nickel ions from the TM layers to the Li layers was described by a direct exchange of one Ni from the 3*a* site with one Li from the 3*b* site (parameter *e* in Table 5.1). Since with XRD elements with similar electron density as Ni, Co and Mn cannot be clearly distinguished from each other, nickel was chosen as representative in the structural model, due to the rather similar ion radius as compared to Li^+. The actual migration of cobalt and manganese to the Li layers is of course still possible and cannot be evaluated by this method. The overall Ni content was fixed according to the chemical formula. In order to simulate a lattice densification (migration of transition metals from the particle surface into former Li sites of the TM layers along with the release of oxygen), the Mn occupancy on the 3*a* site was refined independently. The cobalt occupancy on the 3*a* site was fixed according to the nominal composition. The oxygen occupancy on the 6*c* site was fixed to full occupation.

vi) The average apparent size as well as the average maximum strain σ_{max} were refined (parameters *Y* and *X* in FullProf). Furthermore, an anisotropic strain model for a hexagonal setting (strain model 8) was introduced in order to capture the variation of the lattice parameter c_h with a Gaussian distribution.

viii) The Rietveld refinements were carried out using the FullProf package. Here, the peak profile was described by a pseudo-Voigt function (profile function 7, T-C-H pseudo-Voigt) and the Caglioti parameters (*U*, *V*, *W*), which describe the impact of the experimental setup on the reflection profile shape and half widths were determined using a LaB_6 standard. The background of the diffraction pattern was fitted using a linear interpolation between selected data points in non-overlapping regions. The superstructure reflections in the low 2θ range (9-13°) were excluded from the refinement (excluded region).

Figure 5.7 shows selected refined parameters of various defined states of charge/discharge within the formation cycle of the '6-50:50' material. The delithiation of the material up to a voltage of 4.4 V, which can be considered to be a fully reversible process, leads to a decrease of the lattice parameter a_h and an increase of c_h. The decrease of a_h can be explained by the oxidation of the TM ions and thus a decrease of the ion radii. The lattice parameter c_h strongly depends on the Li occupancy in the Li layers (3*b*). The delithiation of these layers leads to a repulsive force between the now directly opposing oxygen layers and thus to an elongation of the lattice along the c_h axis.

Table 5.1.: 'Model A': On the $R\bar{3}m$ symmetry based structural model used for the Rietveld refinement of diffraction patterns belonging to '6-50:50' cathode samples. Refined parameters are tagged with *. d - degree of lithiation, e - exchange of Li/Ni.

Atom	Wyckoff	x	y	z	Occupancy
Li1	3a	0	0	0	$(0.2{\cdot}d)+e^*$
Ni1	3a	0	0	0	$0.15-e^*$
Co	3a	0	0	0	0.1
Mn	3a	0	0	0	0.55^*
Li2	3b	0	0	0.5	$(1{\cdot}d)-e^*$
Ni2	3b	0	0	0.5	$0+e^*$
O	6c	0	0	0.258^*	1

With further delithiation between 4.4 V and 4.8 V, the c_h parameter remains almost unchanged. The evolution of the c_h parameter reveals a 'dip' at 4.8 V, which is induced by the electron hole formation in the oxygen 2p band and thus leads to a lowering of the repulsion force between the oxygen layers [67]. Interestingly, when the electrode is charged beyond 4.4 V ('plateau'), the refined Ni occupancy in the Li layers (3b) increases significantly from 0(1)% at 4.4 V up to 11(1)% at the end of charge (4.8 V). As already indicated by the broadening of the 018_h reflections in the diffraction patterns, the average maximum strain σ_max and its c_h anisotropy continually increase during charge. The anisotropy is induced by a variation of the c_h parameter within the material and might be due to a non-homogeneous delithiation of the material resulting in a different local density of Li atoms, either from grain to grain or even within a grain. In the subsequent discharge step, the lattice parameters are shifting back towards of their initial values. The Ni occupancy in the 3b site decreases to 5(1)% at 2.0 V suggesting a partially irreversible migration of transition metals from the TM layers into the Li layers within the formation cycle [84]. This migration process is supposed to be directly related to the electrochemical features of Li-and Mn-rich NCMs such as hysteresis (reversible migration) and voltage fade (irreversible migration) [12]. Last, the lattice strain decreases again and finally is close to the initial value, which indicates a homogeneous relithiation of the lattice.

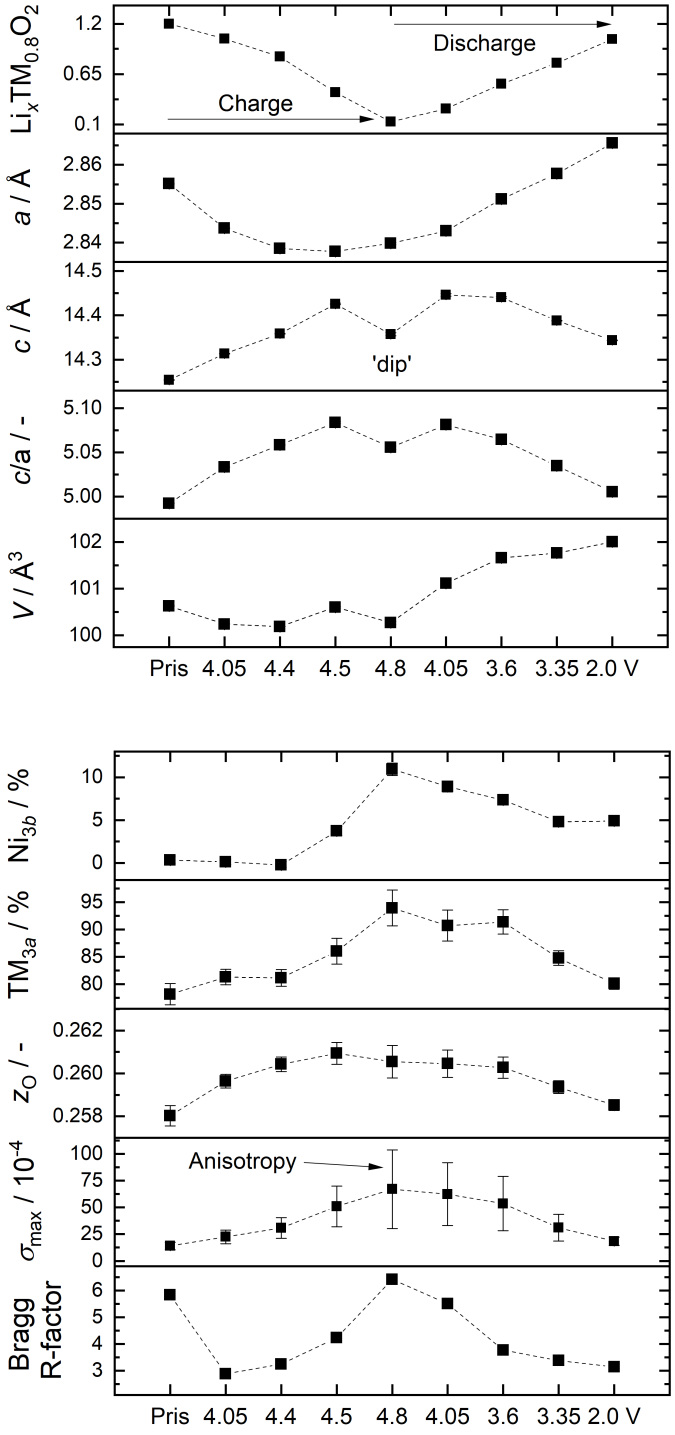

Figure 5.7.: A selection of refined values belonging to the *ex situ* diffraction patterns of '6-50:50' electrodes, which were charged/discharged to defined voltages along the voltage profile of the first cycle (formation). The Rietveld refinement bases on 'Model A' (see Table 5.1), which includes a pattern analysis with one layered oxide phase ($R\bar{3}m$). The dashed lines are inserted as a guide for the eye. $3a$ – TM layer, $3b$ – Li Layer, z_O – z coordinate of the oxygen $6c$ site, σ_{max} – average maximum strain and c_h anisotropy (vertical bars).

5.1.3. ^{6}Li MAS NMR

In this section, the changes regarding the very-local atomic structure of the '6-50:50' cathode material are investigated using ^{6}Li NMR spectroscopy. The measurements were performed on the same electrode powders, which were used for the *ex situ* diffraction experiments. Before the results are shown, the different lithium environments are explained on the basis of the spectrum of the pristine '6-50:50' powder, the end members '6-Li_2MnO_3' and '6-NCM' as well as the '6-30:70' powder, respectively.

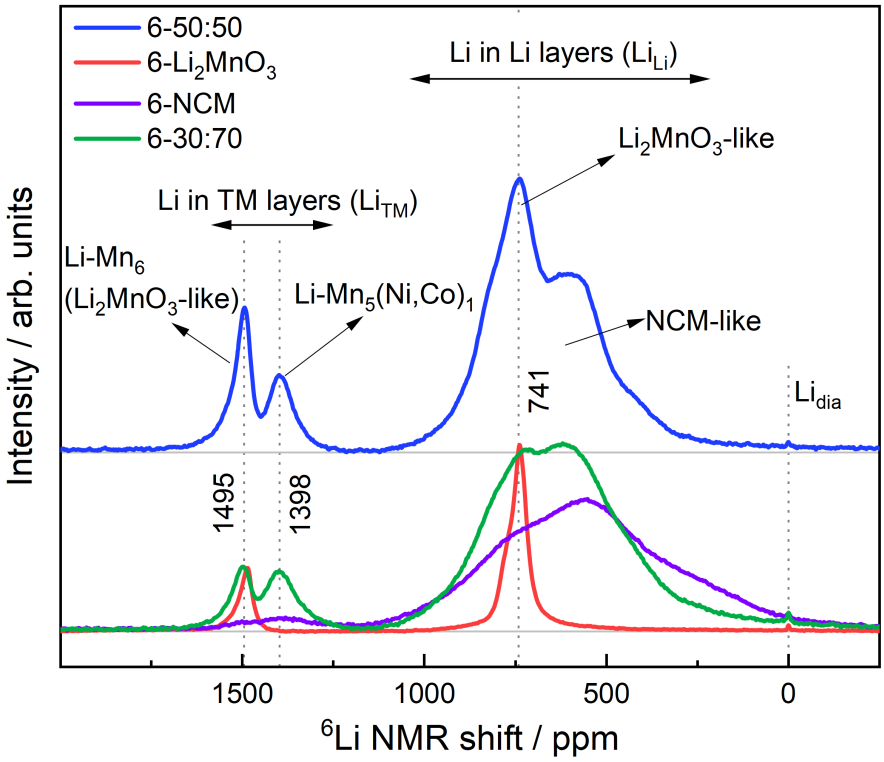

Figure 5.8.: ^{6}Li MAS NMR spectrum of the '6-50:50' powder with a detailed assignment of the individual resonances. The spectra of the end members '6-Li_2MnO_3' and '6-NCM' as well as of the '6-30:70' sample are drawn to support the assignment of the resonances. For presentation purposes the spectrum of the '6-Li_2MnO_3' sample is not drawn to scale. Li-Mn_6 / Li-Mn_5(Ni,Co)$_1$ – Li in the TM layers connected to 6 Mn / 5 Mn + 1 Co,Ni ions via 12 Li-O-TM interactions in the first coordination shell with bond angles of approximately 90°.

As can be seen from Figure 5.8, the ^{6}Li MAS NMR spectrum of the pristine '6-50:50' sample reveals three main groups of lithium environments:

i) The resonance around 0 ppm, which represents diamagneticaly embedded lithium Li_{dia}, e.g. LiOH, Li_2CO_3, components of the cathode electrolyte interphase (CEI) and/or residues of the electrolyte salt ($LiPF_6$).

ii) The group between 300 ppm and 1000 ppm belongs to Li in the Li layers (Li_{Li}) in a paramagnetic environment (TMs with unpaired *d* electrons). From the spectra of pure '6-Li_2MnO_3' and '6-NCM' it can be deduced that the spectrum of the '6-50:50' powder is composed of a rather sharp resonance around 741 ppm (Li_2MnO_3-like) and a broad resonance with with a large variety of different Li environments in the first and second coordination shell, rather similar to the spectrum of pure '6-NCM' (NCM-like) [4, 85]. A summary of the different nearest-neighbor configurations is appended in Table C.2.

iii) The second paramagnetic group between 1300 ppm and 1550 ppm belongs to Li in the TM layers (Li_{TM}). The rather sharp resonances at 1495 ppm (Li_2MnO_3-like) and 1398 ppm can be directly attributed to the well-ordered Li-Mn_6 (1495 ppm) and Li-Mn_5(Ni,Co)$_1$ (1398 ppm) honeycomb environments [4, 86, 87]. Here, the Li ions are surrounded by 6 TM ions (both in the TM layer) via 12 Li-O-TM bonds with a bond angle of about 90°. Determined by integration of the particular areas, this group represents 18% of the overall lithium content (integration of the areas), which is very close to the theoretical value of 17% received from the nominal composition (0.2 out of 1.2 Li).

Figure 5.9 shows the evolution of the ^{6}Li MAS NMR spectra for specified states of charge/discharge on the voltage curve belonging to the initial formation cycle of the '6-50:50' material. As apparent from the decline of the resonance intensities in spectra of the first two partially delithiated samples during charging (4.05 V and 4.4 V), the delithiation takes place in both paramagnetic groups of resonances, i.e. in the Li and in the TM Layer. The initially well-separated Li_{TM} resonances start to broaden indicating a slight modification of the very-local Li-TM_6 ordering until a charging voltage of 4.4 V. These observations are well in agreement with a slight decrease of the $C2/m$ superstructure reflections intensities up to a charging voltage of 4.4 V in the corresponding diffraction patterns (see Figure 5.6).

The spectrum of the '6-50:50' sample that has been charged to 4.5 V, which corresponds to a partially delithiated state approximately in the middle of the 'plateau', shows profound changes concerning both groups of paramagnetic resonances. The intensity of the resonances associated with the

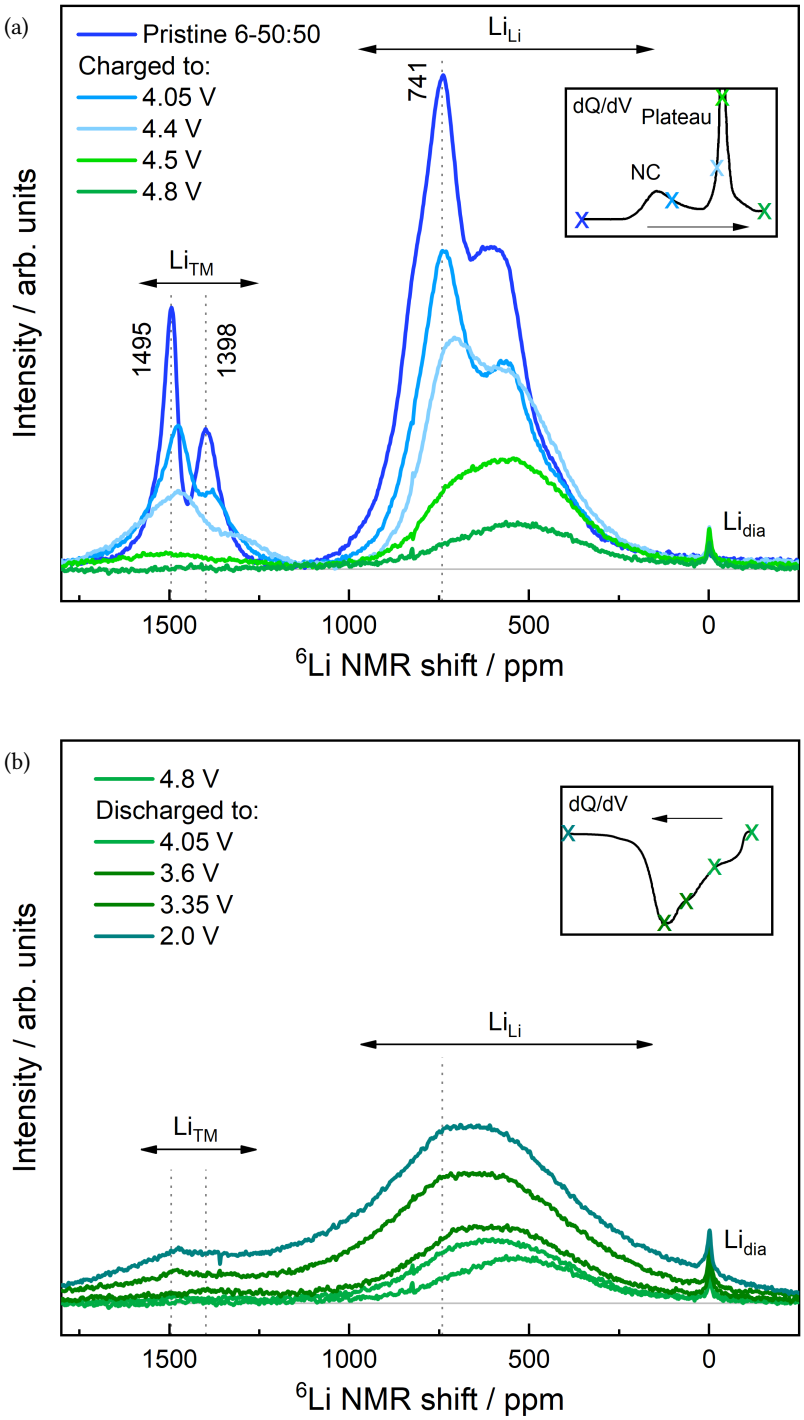

Figure 5.9.: ^{6}Li MAS NMR spectra of '6-50:50' samples, which were charged (a) and (b) discharged to defined voltages along the voltage profile of the first cycle (formation). The insets show the related dQ/dV plots with labels corresponding to voltages at which NMR spectra were acquired. Li_{TM} – Li in TM layer, Li_{Li} – Li in Li layer.

lithium in the TM layers decreased significantly close to zero value and a clear distinction of these Li environments is no longer apparent. As can be seen from the resonances corresponding to lithium in the Li layers, the signal at 741 ppm disappears at a charging voltage of 4.5 V indicating the (full) delithiation or a profound structural modification of Li_2MnO_3-like environments. Accordingly, all resonances, which can be linked to well-ordered lithium environments vanished. By reaching the end of charge (4.8 V), the Li_{TM} signal completely vanished, which indicates an entire delithiation of the TM layers. This observation matches well with the disappearance of the $C2/m$ superstructure reflections in the corresponding diffraction patterns (see Figure 5.6) and altogether indicates the loss of the distinct honeycomb ordering on a long-range as well as on a very-local atomic scale. At the end of charge, a broad signal associated with NCM-like environments remains and represents approximately 12% of the initially available lithium content in the pristine sample. Generally, the center of the Li_{Li} resonance has moved gradually towards lower NMR shift values during charging. Two possible explanations for this observation might be the oxidation of nickel to the diamagnetic +IV state[4] and/or the diffusion of lithium from octahedral into tetrahedral sites, respectively [14, 86]. However, a preferred delithiation of distinct Li environments, which are associated with higher NMR shift values, might be also a suitable explanation.

In the subsequent discharge step, both layers are relithiated without the return of the well-ordered Li environments, which are represented by the 741 ppm, 1398 ppm and 1495 ppm signals. Overall, the NMR spectra show a profound general peak broadening and an overlap of the former clearly distinguishable resonances of the Li and TM layers, respectively. This can be explained by the irreversible order-disorder transition during the initial charge ('plateau') and thus the creation of a large variety of new Li environments (defects) particularly in former well-ordered Li_2MnO_3-like environments. This leads to a rather large variety of NMR shifts.

At the end of the formation cycle, approximately 84% of the initial Li content has been relithiated (derived from the integrals of the NMR spectra). This is well in accordance with the value derived from the electrochemical data (86%). The progression of the Li content within the formation cycle is illustrated in Figure 5.10a. The values are derived from the electrochemical data as well as from the integrals of the ^{6}Li NMR spectra. As emphasized by the red arrow, the first cycle shows a significant path-dependency of the de-/lithiation process induced by an irreversible structural rearrangement along with the depletion of electrochemically available Li sites (purple arrow).

[4] The decline of the amount of unpaired *d* electrons in the transition metal ions leads to a lowering of the 'paramagnetic character' in the Li environment and thus to a shift of the NMR signal/s towards lower values.

In Figure 5.10b the evolution of the Li content during charging is plotted individually for the Li and the TM layer, respectively. Apparently, the Li extraction takes place in both layers from the beginning. Based on this observation, an exclusive delithiation of the Li_{TM} sites, for instance, on the 'plateau' can be excluded at this point. However, the major part of Li_{TM} sites are depleted on the 'plateau', which might lead to a high lattice strain and finally to the collapse of the honeycomb ordering in the TM layers.

Taken together, the investigations focusing on the initial formation process of a Li- and Mn-rich NCM clearly presented the irreversible structural transition from a well-ordered towards a highly defective material, which can be associated with the 'plateau' in the voltage profile of the first charge. As aforementioned, this is indicated by the disappearance of the $C2/m$ superstructure reflections as well as the distinct ^{6}Li NMR resonances, which both correspond to the Li/TM-TM_6 honeycomb ordering in the TM layers, respectively on a different atomic scale. This newly formed highly defective material is in a metastable state, which exhibits an additional reversible anionic low-voltage redox process ('O_{def}') and a gradual decrease of the mean charge and discharge voltages with increasing number of cycles, respectively.

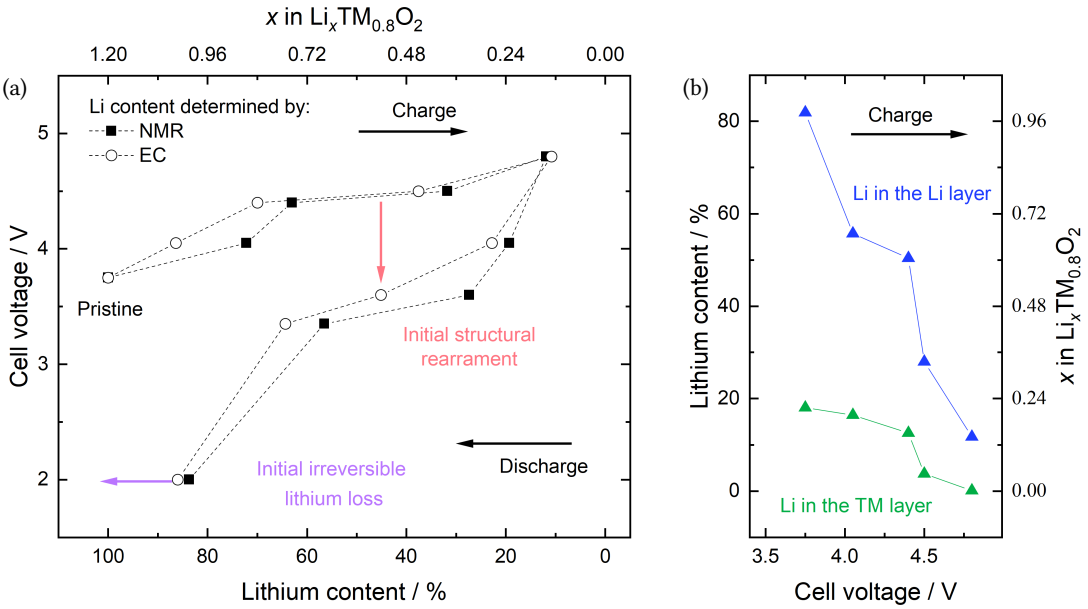

Figure 5.10.: Correlation of the cell voltage with the lithium content throughout the formation cycle (a). The lithium content was determined on the basis of the reached charge/discharge capacity neglecting side reactions (label 'EC') as well as by the integration of the corresponding NMR spectrum (label 'NMR'). The data point of the pristine sample was placed according to the onset voltage of the first oxidation peak (3.75 V) in the electrochemical data. Graph (b) shows the evolution of the lithium content during charge individually for the Li and the TM layer. Therefore, the peak areas of the Li_{Li} and the Li_{TM} resonances were integrated separately.

5.2. Thermal treatment of discharged samples (2.0 V)

In this section, the influence of a thermal treatment on discharged 'HE5050' cathode samples (2.0 V) is investigated. These samples experienced the initial formation cycle and thus are featuring a highly defective metastable structure. The impact of the thermal treatment was studied in detail by characterizing the electrochemical properties as well as the structure (diffraction and NMR) starting with the highest temperature of 300 °C. In a further series of experiments, the procedure was repeated with temperatures of 150 °C, 200 °C and 250 °C in order to follow the temperature dependence of the processes occurring during heating. As a remark, the commercial 'HE5050' (TODA) was chosen for the following investigations due to the high amount of samples needed for the experiments and the higher cycling stability of the commercial cathode material, respectively. The reproducibility of the heat treatment as well as a summary of all cells regarding the discharge capacity and the mean charge/discharge voltage is presented in the Appendix A.1.

5.2.1. Electrochemical characterization

Figure 5.11a shows the cell voltage vs. specific capacity of the formation cycle and the cycle after formation as well as the first and fifth cycle after the heating step (post thermal) of the commercially available Li- and Mn-rich 'HE5050' cathode material. The corresponding dQ/dV vs. cell voltage curves are plotted in Figure 5.11b. As apparent from the graphs, the 'HE5050' material shows similar electrochemical characteristics like the self-synthesized '6-50:50', which has the same stoichiometry but is probably prepared by a different synthesis route and heating procedure. A comparison of 'HE5050' and '6-50:50' regarding the first two cycles is appended in Figure C.4. During the initial charge, the first oxidation peak 'NC' located at about 4.0 V is attributed to the oxidation of the transition metal ions Ni and Co from +II/+III states to +IV delivering a capacity of 106 mAh/g until 4.4 V. The second part of the charging curve with an extended 'plateau' at 4.5 V belongs to the oxidation of the oxygen and an irreversible formation of the Li- and Mn-rich NCM. This induces a loss of the initial electrochemical and structural features of the pristine material as has been clearly demonstrated in the last section (Section 5.1). In summary, the overall charging step possesses a capacity of 305 mAh/g until 4.7 V.

In the first discharge, there is no reduction process corresponding to the 'plateau' present, due to the irreversible structural modifications. Instead, the two newly occurring redox processes

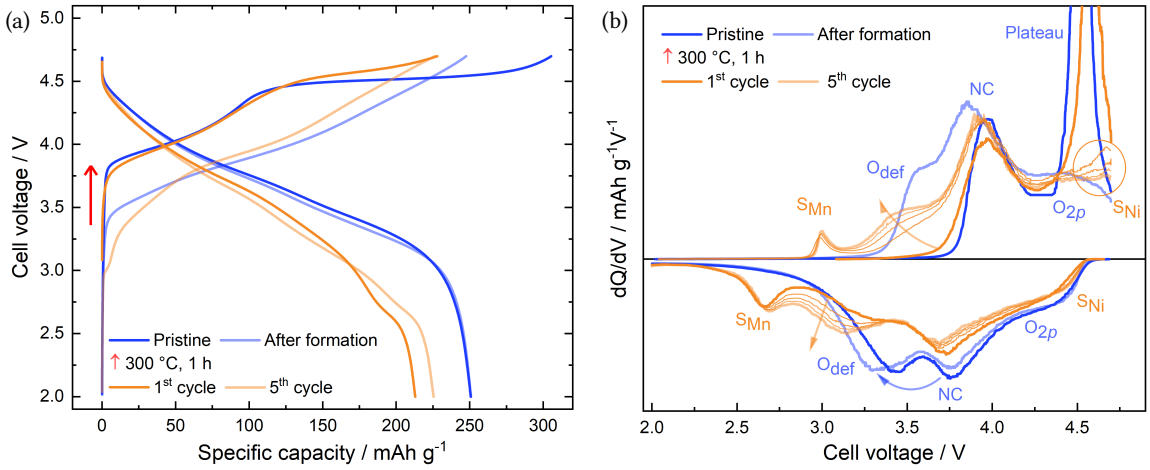

Figure 5.11.: Cell voltage vs. specific capacity (a) and the thereof derived differential capacity (dQ/dV) plot (b) corresponding to the thermal treatment experiments of discharged 'HE5050' cathode samples (2.0 V). The measurements were carried out with a rate of C/10 and an end of charge and discharge voltage of 4.7 V and 2.0 V, respectively. Labels: 'NC' – Ni/Co redox activity, 'O_{2p}' – oxygen 2*p* band, 'O_{def}' – defect-associated oxygen redox activity, 'S_{Mn}'/'S_{Ni}' – Mn/Ni redox activity in a LNMO-like spinel.

with maximum peak position around 4.3 V ('O_{2p}') and 3.3 V ('O_{def}') are present in addition to the reduction peak 'NC', which was already observable during the initial charge. At the end of discharge a capacity of 251 mAh/g is reached, which leads to a capacity loss of 54 mAh/g. In the subsequent cycle after formation, the onset-voltage of the first oxidation peak is lowered to 3.3 V. It represents the defect-associated anionic redox contribution 'O_{def}', followed by 'NC' and 'O_{2p}'. Analogously, these processes are occurring in reversed order in the second discharge. Also the 'HE5050' sample reveals a decrease of the mean charge/discharge voltages with increasing numbers of cycles (voltage fade) as can be seen by comparing the discharge curves of the formation cycle and the cycle after formation. The low-voltage region 'O_{def}' becomes more prominent at the expense of high-voltage region 'NC' leading to a decrease of the mean voltage as highlighted by the blue arrow.

A discharged electrode (2.0 V) after formation was heated at 300 °C for 1 h in argon atmosphere, reinserted in a fresh coin cell and electrochemically characterized for five further cycles (post thermal). The most surprising observation emerging from the first post thermal charge is the reoccurrence of the 'plateau' at about 4.5 V and thus indicates the (partial) recovery of initially well-ordered structure of the pristine material. Generally, the electrochemical features are very

similar to the pristine material: The first oxidation process 'NC' starts again at 3.7 V compared to 3.3 V for the sample after formation and is attributed to the oxidation of Ni and Co to +IV. Until 4.4 V a charge capacity of 112 mAh/g is reached, which is similar to the 106 mAh/g reached in the initial charge. This is followed by a less pronounced and shorter 'plateau' in comparison to the initial charging curve leading to an overall charge capacity of 226 mAh/g. Analogous to the formation cycle of the pristine material, the 'plateau' vanishes after the first post thermal charge. Instead, the redox processes 'O_{def}' and 'O_{2p}' reappear again in the following charge and discharge steps.

Interestingly, the first post thermal discharge and also the following cycles show an additional redox process ('S_{Mn}') at around 2.7/3.0 V (charge/discharge). The second post thermal charging curve as well as the following cycles after heat treatment reveal another newly arising oxidation peak (S_{Ni}) around 4.5-4.7 V as highlighted in the graph by the orange circle. The corresponding reduction peak is probably overlapping with the reduction peak 'O_{2p}'. These findings strongly suggest the reversible de-/lithiation of a second phase, which has very similar electrochemical features as a $LiNi_{0.5}Mn_{1.5}O_4$-type spinel (LNMO). As will be shown in detail in Section 5.3, the high-voltage peak 'S_{Ni}' is associated with the redox activity of $Ni^{2+/4+}$ and the low-voltage peak with $Mn^{3+/4+}$ in a cubic spinel-type environment. The existence of a second phase with a cubic symmetry after the thermal treatment of a discharged sample will be confirmed by the evaluation of the diffraction measurements following this section. As indicated by the arrows in the dQ/dV plot, region 'O_{def}' develops a stronger contribution to the capacity during the five post thermal cycles and overcompensates the capacity loss at region 'NC' (voltage fade). This leads to an increase of the discharge capacity from 213 mAh/g to 225 mAh/g within five cycles.

5.2.2. Synchrotron radiation powder diffraction

Figure 5.12 shows the *ex situ* synchrotron radiation powder diffraction (SRPD) patterns of the pristine 'HE5050' cathode powder as well as that of the samples after formation, heating and relithiation (post thermal cycles). Additionally, selected refined parameters will be presented in Figure 5.17 in Section 5.2.5 later on. Similar to the '6-50:50' material, weak $C2/m$ superstructure reflections are apparent in the low 2θ range around 2.8° for the pristine material. However, the reflections are less pronounced in comparison to the pattern of the self-synthesized material as (see appendix Figure C.5). This indicates a less pronounced honeycomb ordering on a long-range atomic scale within the commercial 'HE5050' material [44].

After the formation cycle, the diffraction pattern clearly reveals structural changes, which are ascribed to the irreversible structural modifications during the 'plateau': The $C2/m$ superstructure reflections disappeared and thus the long-range Li/TM-TM_6 honeycomb ordering. Furthermore, a comparison of the half widths of the neighboring reflections 018_h and 110_h indicates a strong anisotropic lattice strain in direction of c_h (variations of the c_h parameter). The refined Ni content in the Li layers increases from 0.8(3)% in the pristine sample to 4.7(6)% in the sample after formation.

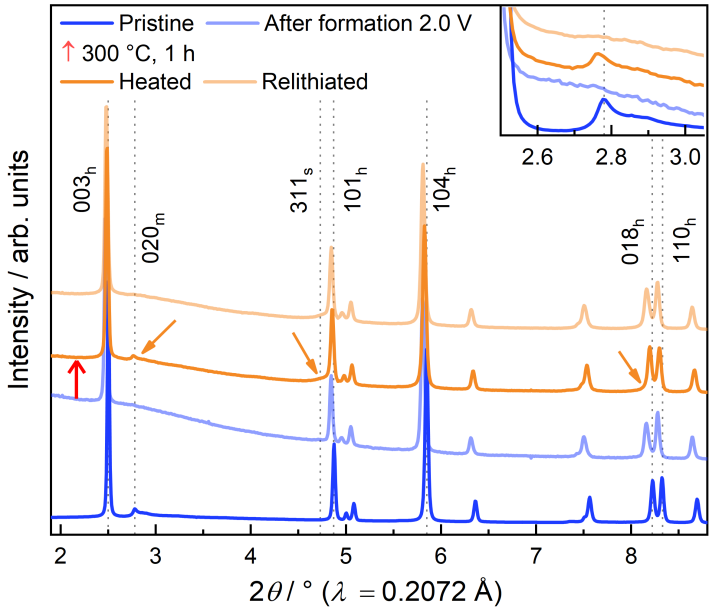

Figure 5.12.: SRPD patterns corresponding to the thermal treatment experiments of discharged (2.0 V) 'HE5050' cathode samples. The $C2/m$ superstructure reflections (represent the long-range honeycomb ordering) are magnified in the inset. Reflection-subscripts: m – monoclinic setting, h – hexagonal setting, s – spinel.

This suggests an irreversible TM migration from the octahedral sites of the TM layers (3*a*) to the octahedral sites of the Li layers (3*b*) during the formation cycle.

After heating at 300 °C for 1 h, three major changes are apparent in the diffraction pattern highlighted by the orange arrows: i) The most striking observation is the reappearance of the $C2/m$ superstructure reflections as clearly shown in the inset of Figure 5.12. This finding explicitly points to the (partial) recovery of the Li/TM-TM_6 honeycomb ordering on a long-range perspective. ii) The half width of the 018_h reflection is narrowed again suggesting a reduction of the c_h-anisotropic lattice strain. iii) Some reflections reveal a specious asymmetric broadening most clearly seen for the 110_h reflection. The structural analysis of the diffraction data attributed the origin of the 'broadening' to the formation of a second phase, which can be assigned to a cubic spinel with $Fd\bar{3}m$ symmetry. Since the exact composition of the newly formed phase cannot be derived from the data, for simplification the $LiMn_2O_4$ spinel is used hereinafter for Rietveld refinement. Of course, this phase may also contain cobalt and/or nickel. The phase content of $LiMn_2O_4$ in the sample after heating was refined to 16(3)% (w/w), with an average apparent domain size of approximately 4 nm. After heating, a mass loss of 2.2(6)% (w/w) was determined for the electrode coating, which includes the active material, binder and carbon, respectively. Commonly the observed mass loss in layered oxide cathode materials during heating is ascribed to oxygen release with a simultaneously occurring structural phase transition towards an oxygen-poor phase, for instance, the observed spinel formation [88].

After the five post thermal cycles (relithiation), similar changes appear in the diffraction pattern as already discussed for the diffraction pattern of the pristine sample after formation including the disappearance of the $C2/m$ superstructure reflections. However, the nano-spinel phase is still present (refined to 14(3)% (w/w), 5 nm). This observation is well in agreement with the reversible redox activity of a LMNO-type spinel represented by the redox peaks 'S_{Mn}' and 'S_{Ni}' in the electrochemical data (see Figure 5.11).

5.2.3. ^{7}Li MAS NMR

As shown in Figure 5.13, the ^{7}Li MAS NMR spectrum of the pristine 'HE5050' powder consists of three groups of lithium environments. The diamagnetic resonance around 0 ppm and the two paramagnetic groups between 300 ppm and 1000 ppm (Li in Li layers) and between 1300 ppm and 1500 ppm (Li in TM layers). However, the main resonances are strongly overlapping with several spinning sidebands from all three groups, which complicates the quantitative analysis (detailed discussion in Section 5.1.3). For this reason, the NMR spectra are qualitatively discussed based on the evolution of: i) the rather sharp peaks at 711 ppm, 1351 ppm and 1442 ppm associated with the well-defined Li coordinations in a highly ordered environment similar to that in pure Li_2MnO_3 and ii) the broad resonance ranging from 300-1000 ppm associated with a large variety of different Li environments similar to those in pure NCM (see Figure 5.8).

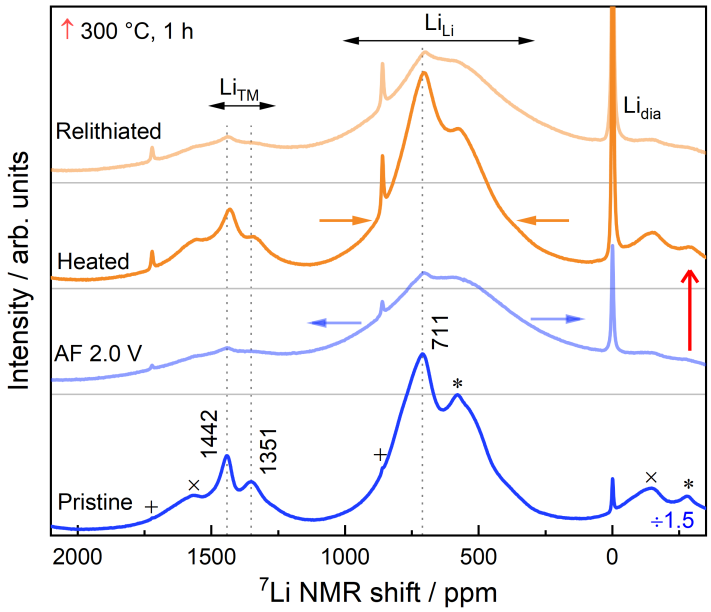

Figure 5.13.: ^{7}Li MAS NMR spectra corresponding to the thermal treatment experiments of discharged 'HE5050' samples (2.0 V). Labels: Li_{Li} – Li in Li layers, Li_{TM} – Li in TM layers, Li_{dia} – diamagnetic embedded lithium. The spinning sidebands (±861 ppm) are shown exemplarily in the spectrum of the pristine sample: + (Li_{dia}), × (Li_{Li}) and ∗ (Li_{TM}). For presentation purposes the intensity of the spectrum belonging to the pristine sample is damped by factor 1.5.

After the formation (light blue spectrum, AF 2.0 V), the resonances are significantly broadened as emphasized by the blue arrows, due to the loss of local ordering, i.e. an order-disorder transition. Associated therewith is the creation of many different Li environments particularly in previously well-ordered Li_2MnO_3-like environments. This observation is in good agreement with the loss of the long-range Li/TM-TM_6 honeycomb ordering after formation, which has already been proved by the disappearance of the $C2/m$ superstructure reflections in the corresponding diffraction pattern (see Figure 5.12). The distinct peaks at 1442 ppm and 1352 ppm, which are associated with the Li-Mn_6 and Li-Mn_5(Ni,Co)$_1$ honeycomb ordering in the transition metal layers, almost vanished. Whether these Li_{TM} sites remain primarily unoccupied after formation or whether their environment has changed considerably is not clearly apparent, since the Li_{TM} resonances strongly overlap with the spinning sidebands from the Li_{Li} resonances. However, the high resolution ^{6}Li MAS NMR spectrum of the '6-50:50' sample clearly shows the relithiation of the TM layer at the end of the first cycle, although without a distinct ordering (shown previously in Figure 5.9).

Very interestingly, the thermal treatment of a sample after formation led to a pronounced reappearance of the Li_{TM} resonances at 1442 ppm and 1351 ppm. These are directly related to the local Li-TM_6 honeycomb ordering in the TM layers. In conjunction with the return of the 711 ppm resonance, this clearly indicates the (partial) recovery of the well-ordered pristine state in the entire bulk material. In contrast to the results from the diffraction and electrochemical measurements, the NMR spectrum shows no direct evidence for the formation of a second phase (spinel). From the superimposition of the spectra of the pristine sample and the sample after heating it is apparent (see Figure 5.16b, will be shown in Section 5.2.5), that the Li_{TM} peak areas have a decreased contribution to the overall spectrum in the sample after heating. Additionally, a slight broadening of the Li_{Li} resonance remained after the heat treatment. These observations suggest a non-completed restoration of the pristine ordering, most probably due to the irreversible loss of lithium after formation.

After the five post thermal electrochemical cycles (relithiation), the ^{7}Li NMR spectrum is again similar to that of the sample after formation including the loss of local ordering and an overall peak broadening. Here as well, no direct indication for a lithiated spinel phase was found. The spectral features that can be ascribed to the spinel lithium sites are supposed to be 'buried underneath' the broad Li_{Li} resonance of the layered phase [4, 85].

5.2.4. ^{6}Li MAS NMR

In order to obtain a more detailed picture on the changes of the local Li environments after heating the thermal treatment experiments were repeated with the self-synthesized '6-50:50' cathode powder and high resolution ^{6}Li MAS NMR spectra were obtained as shown in Figure 5.14. It is apparent that the Li_{TM} resonances are less pronounced in the spectrum of the sample after heating and a slight broadening of the Li_{Li} resonances remained in comparison to the spectrum of the pristine sample. An integration of the spectra revealed that about 84% of the initial lithium content is present in the sample after formation and 82% in the sample after heating, respectively.
These results clearly illustrate the non-completed restoration of the pristine well-ordered state, which is well in agreement with the corresponding diffraction patterns in Figure 5.14b. The intensity of the $C2/m$ superstructure reflections is significantly damped, which indicates a high stacking fault density of the 'honeycomb layers' along the c axis and/or the non-completed restoration of the

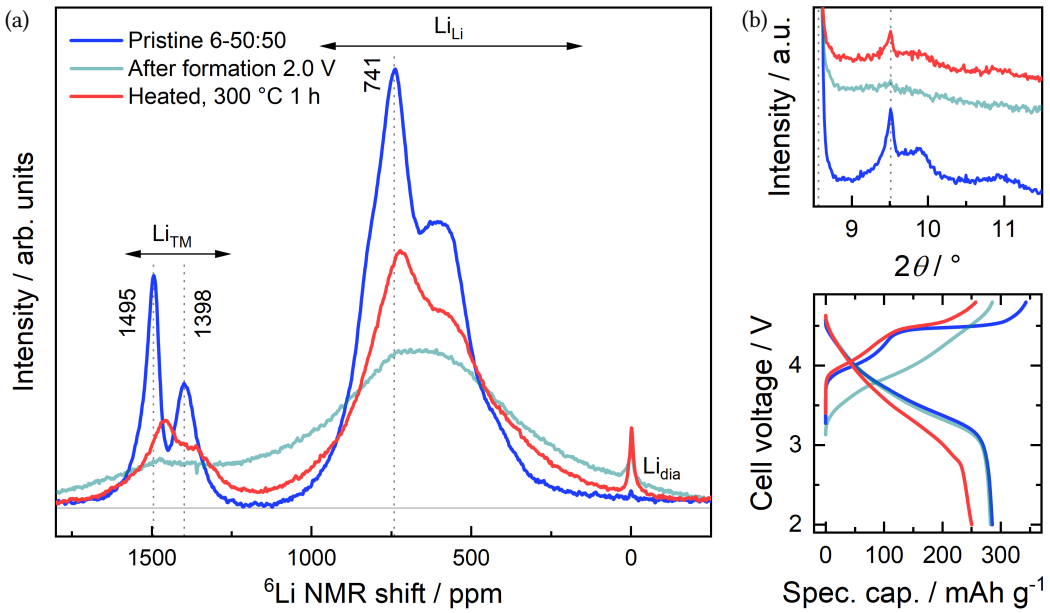

Figure 5.14.: ^{6}Li MAS NMR spectra (a) belonging to the thermal treatment experiments of self-synthesized discharged '6-50:50' samples (2.0 V). Labels: Li_{Li} – Li in Li layers, Li_{TM} – Li in TM layers, Li_{dia} – diamagnetic embedded lithium. The magnification of the $C2/m$ superstructure reflections of the corresponding diffraction patterns (λ=0.70932 Å) and the electrochemical data (cycled with C/50, 4.8 V - 2 V) of the samples are shown in (b). The diffraction patterns showing an extended 2θ range are appended in Figure D.7.

Li/TM-TM_6 ordering within the TM layers. However, these features are not surprising, due to the lithium loss within the initial formation cycle (capacity loss). Overall, these structural modifications are strongly correlated with the occurrence of a shorter and less pronounced ‘plateau’ in the first post thermal cycle of the heated sample in comparison to the initial charging curve of the pristine sample as shown in Figure 5.14b. In contrast, the first part of the charging curve is rather similar in both samples.

5.2.5. Electrochemical and structural changes below 300 °C

The so far presented results strongly suggest the partial recovery of the pristine well-ordered state in a discharged sample after heating at 300 °C for 1 h. However, the irreversible loss of lithium after formation results in a lithium deficiency in the material, which prevents a full restoration of the pristine state. Instead, a small fraction of a Li-poor spinel is formed within the layered $R\bar{3}m$ matrix to compensate the Li deficiency and to provide lithium for the restoration of the Li-rich main phase, respectively.

In order to get a detailed picture concerning the reordering processes and the onset temperature of the spinel formation, the heating experiments were repeated at a temperature of 150 °C, 200 °C and 250 °C, respectively. The results of the electrochemical characterization (first and fifth cycle post thermal cycles) are presented in Figure 5.15. As apparent from the dQ/dV plot of the first post thermal cycle (b), the peak area belonging to the anionic defect-related oxygen contribution ('O_{def}') is continuously declining with increasing temperature. Obviously, this process is directly correlated with the rising emergence of the 'plateau' at 4.5 V, i.e. a disappearance of the 'O_{def}' peak area after thermal treatment goes along with a reappearance of the 'plateau' at 4.5 V. Until 250 °C, the restoration of the electrochemical features towards the initial pristine state is not linked to the formation of a redox active spinel phase as suggested by the absence of the redox peaks 'S_{Mn}' and 'S_{Ni}'. As evident from the fifth post thermal cycle (d), the majority of the capacity loss after thermal treatment can be allocated to the redox process 'O_{def}' and is increasing for higher temperatures.

The observations in the electrochemical data are further supported by the corresponding diffraction patterns in Figure 5.16a, where no indication for the nucleation of a second phase is found up to 250 °C. Instead, a gradual recovery of the local ordering can be observed as indicated by: i) the continuous narrowing of the ^{7}Li NMR resonances (highlighted in Figure 5.16b), ii) the decrease of the refined lattice parameters a_h and c_h towards the initial values of the pristine material (Figure 5.17), iii) the decrease of the refined lattice strain and its c_h-anisotropy (highlighted by the red arrows), and iv) a very weak reoccurrence of the 020_m superstructure reflection.

From these findings it can be concluded, that the initial ordering of the Li- and Mn-rich material is gradually restored on a very-local scale below 300 °C. The dominant process might be the thermally induced 'healing' of defects, i.e. a kind of 'annealing' process. This might include, for example, the depletion of tetrahedral sites that are partially occupied by lithium and/or transition metal ions after formation [11, 12, 13]. These structural modifications are directly correlated with the gradual

disappearance of the redox peak 'O_{def}' and the reoccurrence of the 'plateau' in the first post thermal charge. As aforementioned, this is followed by a more profound reorganization (disorder-order transition) on a long-range atomic scale at 300 °C including the segregation into a Li-rich and a Li-poor phase (spinel).

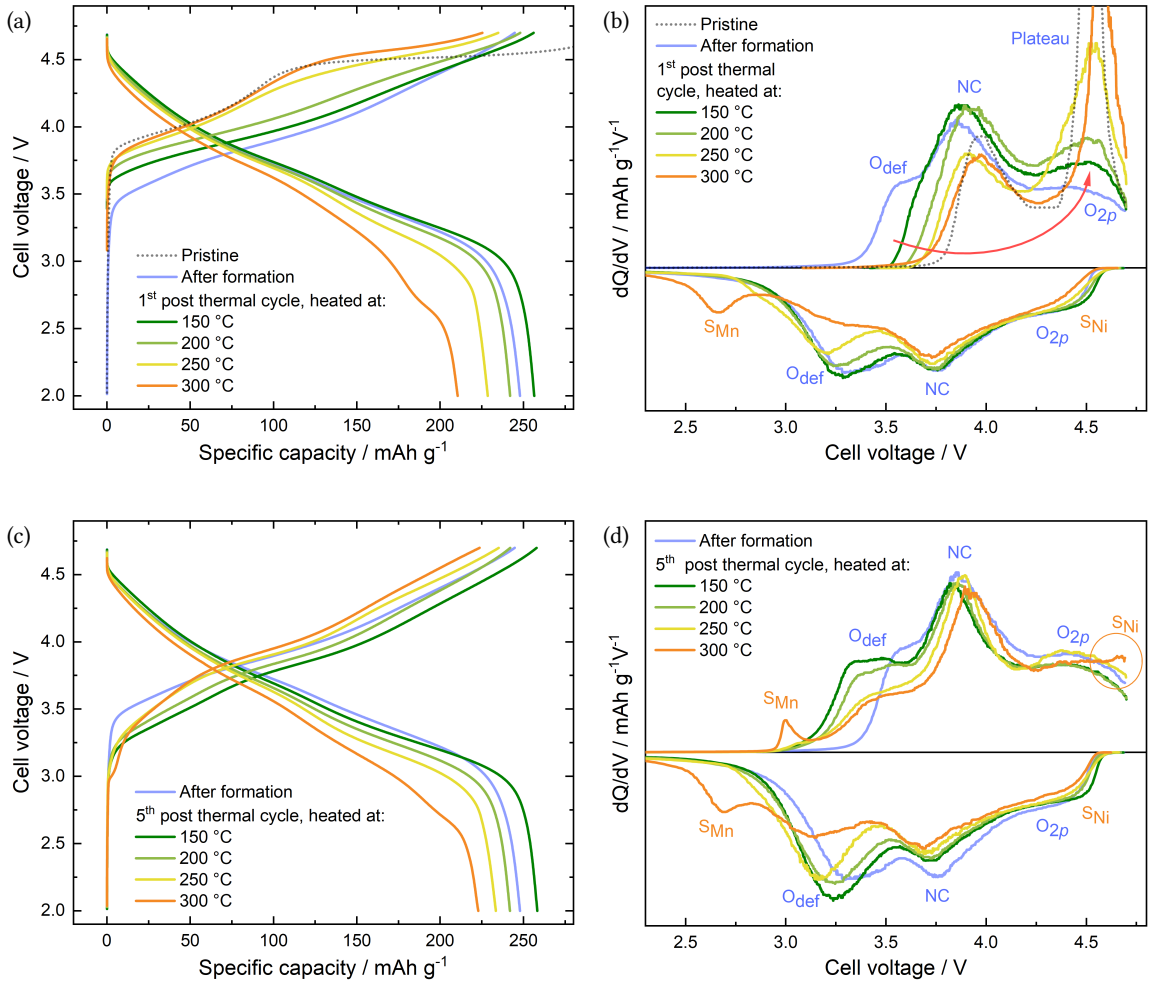

Figure 5.15.: Thermal treatment of discharged 'HE5050' samples (2.0 V) at various temperatures ranging from 150 °C to 300 °C: Cell voltage vs. specific capacity plots of the first (a) and fifth (c) post thermal cycles and the thereof derived dQ/dV plots (b,d). Labels: 'NC' – Ni/Co redox activity, 'O_{2p}' – oxygen 2*p* band, 'O_{def}' – defect-associated oxygen redox activity, 'S_{Mn}'/'S_{Ni}' – Mn/Ni redox activity in a LNMO-like spinel.

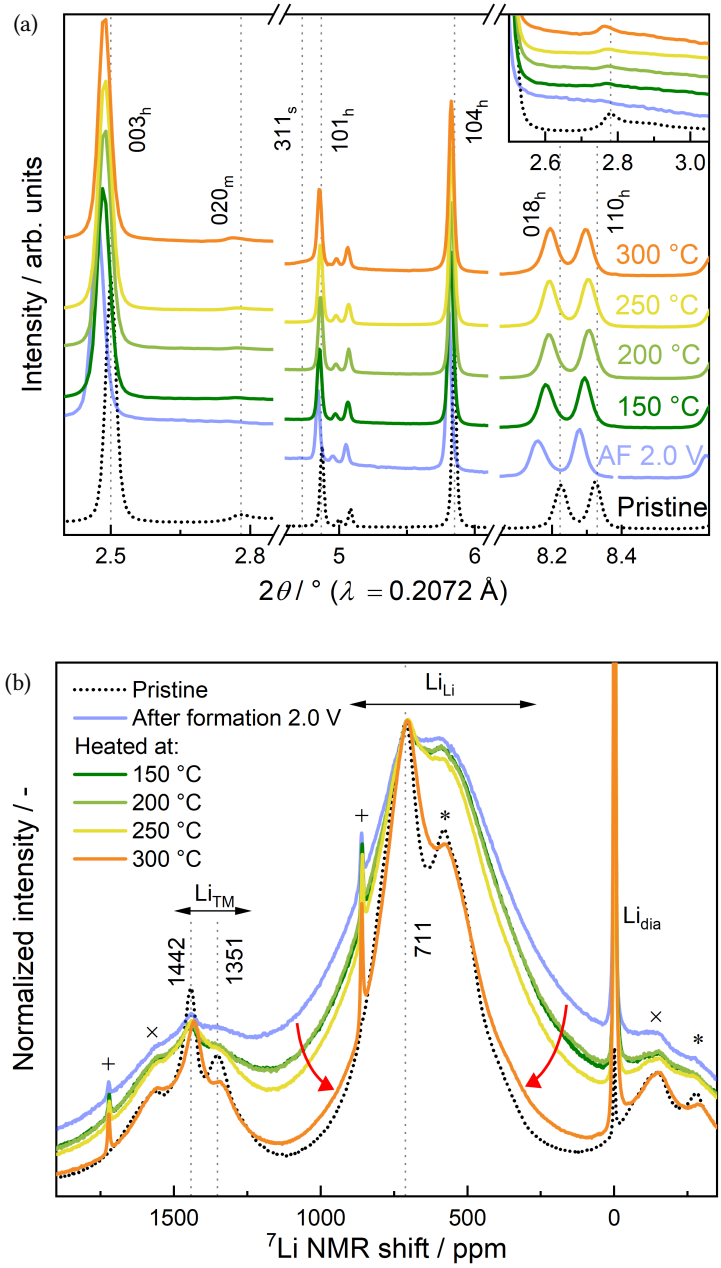

Figure 5.16.: Structural analysis regarding the thermal treatment experiments of discharged 'HE5050' samples (2.0 V) at various temperatures from 150 °C to 300 °C: *ex situ* SRPD patterns (a) with a magnification of the $C2/m$ superstructure reflections in the inset and *ex situ* ^{7}Li MAS NMR spectra (b) normalized with respect to the 711 ppm peak height. Reflection-subscripts: m – monoclinic setting, h – hexagonal setting, s – spinel. Labels NMR: Li_{Li} – Li in Li layers, Li_{TM} – Li in TM layers, Li_{dia} – diamagnetic embedded lithium. The spinning sidebands (±861 ppm) are shown exemplarily in the spectrum of the pristine sample: + (Li_{dia}), × (Li_{Li}) and ∗ (Li_{TM}).

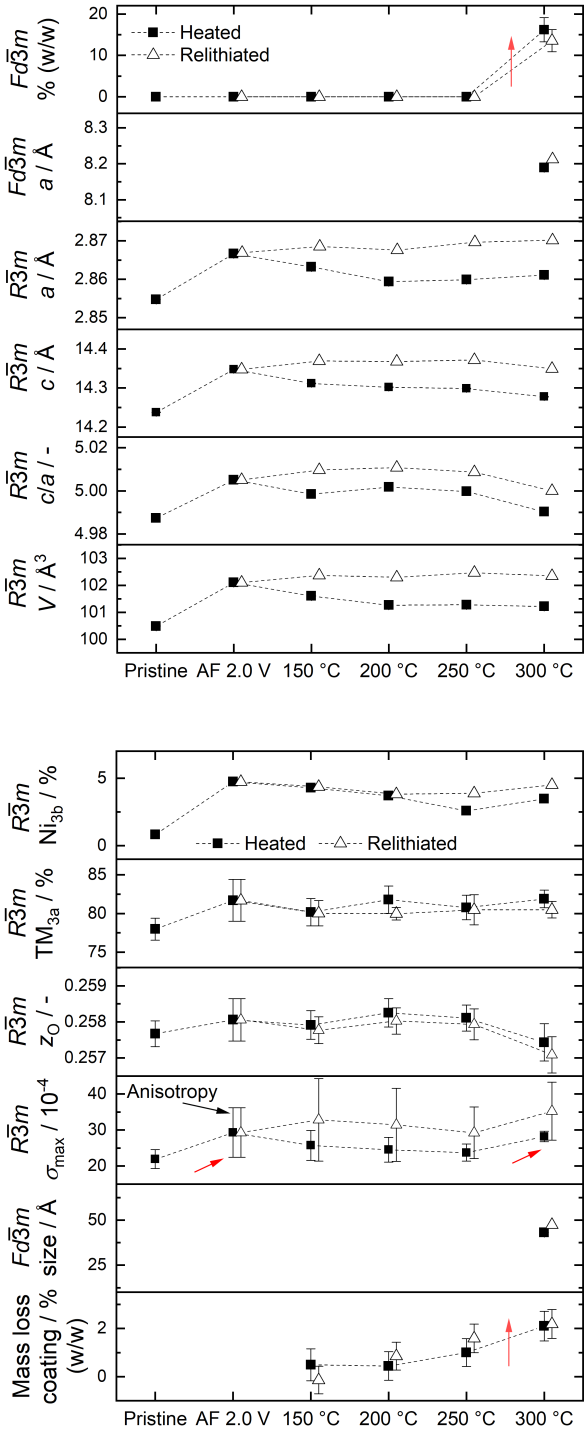

Figure 5.17.: Selected parameters from the Rietveld refinement corresponding to the thermal treatment experiments of discharged 'HE5050' samples (2.0 V) at various temperatures ranging from 150 °C to 300 °C. The underlying structural model (Model SR_{ox}) of the refinement is described in Section 5.3.3. The dashed lines are inserted as a guide for the eye. $3a$ – TM layer, $3b$ – Li Layer, z_O – z coordinate of the oxygen $6c$ site, σ_{max} – average maximum strain and c_h anisotropy (vertical bars).

5.3. Thermal treatment of samples charged to 4.7 V

In this section, the impact of a thermal treatment on charged 'HE5050' cathode samples (4.7 V) is investigated. These samples also experienced the initial formation cycle and thus are featuring a highly defective metastable structure combined with a high degree of delithiation. The influence of the thermal treatment was studied in detail by characterizing the electrochemical as well as the structural alterations (SRPD and NMR) starting with the highest temperature of 300 °C. Special emphasis is put on the development of a suitable structural model for the Rietveld refinement of the emerging spinel-related reflections in the diffraction patterns. In a further series of experiments, the procedure was repeated with temperatures of 150 °C, 200 °C and 250 °C in order to follow the temperature dependence of the processes occurring during heating.

5.3.1. Electrochemical characterization

As shown in Figure 5.18, the thermal treatment of a charged electrode after formation at 300 °C for 1 h led to a strong degradation of the electrochemical properties, similar to those of highly cycled samples [89]. As highlighted by the red arrow in Figure 5.18a, the first post thermal discharge curve (red dotted line) starts at a lower voltage of 3.2 V. Thus, the discharge directly started in the 'O_{def}' region and skipped the reduction processes 'O_{2p}' and 'NC', respectively. This is followed by two reduction peaks at 2.7 V ('S_{Mn}') and 2.1 V ('S_{Mn2}'), which again can be attributed to the lithiation of a LNMO-like spinel including an active $Mn^{3+/4+}$ redox couple. The origin of 'S_{Mn2}' will be discussed below on the basis of the LNMO spinel reference shown Figure 5.19. The discharge capacity significantly decreased from 247 mAh/g before to 122 mAh/g after heating, which suggests a profound loss of electrochemically active Li sites after thermal treatment.

The subsequent charging step begins with the oxidation peak 'S_{Mn}', which has its peak maximum at a cell voltage of 3.0 V, followed by one comparably weak oxidation peak at 3.9 V ('NC') and one above 4.3 V ('S_{Ni}'), which were absent in the preceding discharge step. Overall, a charge capacity of 171 mAh/g is reached leading to an 'overcapacity' of 49 mAh/g, since only 122 mAh/g were discharged (lithiated) before. As it is apparent from the dQ/dV plot, this 'overcapacity' is mainly originating from the high-voltage region 'S_{Ni}', which is associated with the $Ni^{2+/4+}$ redox activity and the de-/lithiation of a cubic LNMO-like Li environment. This observation is surprising, since there is no indication that nickel (+IV in the charged state) has been reduced within the first post thermal discharge. Accordingly, nickel would be rather incapable of being oxidized in the

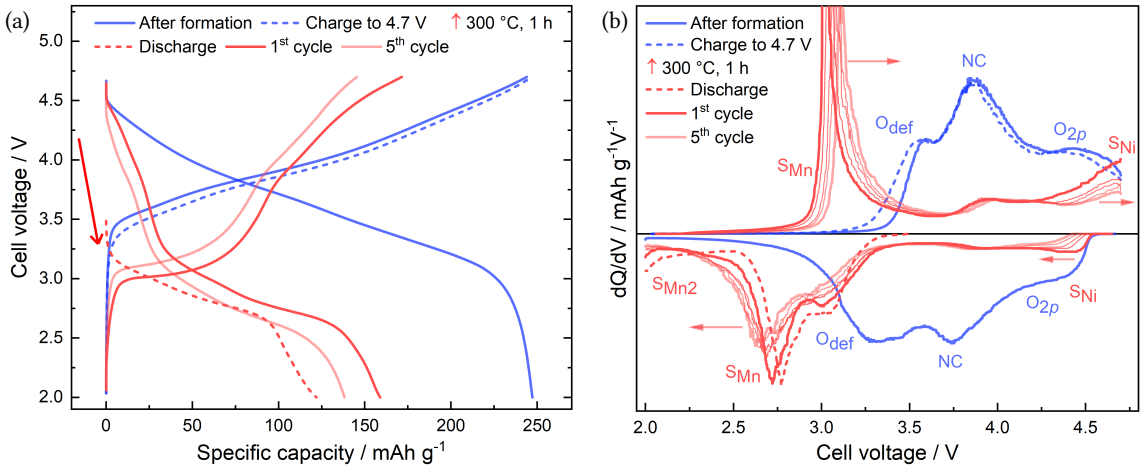

Figure 5.18.: Cell voltage vs. specific capacity (a) and the thereof derived differential capacity (dQ/dV) plot (b) corresponding to the thermal treatment experiments of charged 'HE5050' cathode samples (4.7 V). Cycling parameters: C/10, 4.7 V - 2 V. Labels: 'NC' – Ni/Co redox activity, 'O_{2p}' – oxygen 2*p* band, 'O_{def}' – defect-associated oxygen redox activity, 'S_{Mn2}'/'S_{Mn}'/'S_{Ni}' – Mn/Ni redox activity in a LNMO-like spinel.

subsequent charge. These findings lead to the conclusion, that Ni must have been reduced from +IV to +II during the heating procedure. Results of X-ray absorption spectroscopy measurements (see Section 5.8.1) support this conclusion by showing a clear shift of the Ni K-edge towards lower absorption energies and therefore a reduction of the oxidation state after thermal treatment. The charge compensation for this reduction process is carried out by the release of oxygen, which will be discussed in detail in Section 5.6. After the five post thermal cycles, the electrode exhibits a continued decline of the charge and discharge capacities along with an increasing overpotential as indicated by the divergence of the charge and discharge potential levels of the redox peaks 'S_{Mn}' and 'S_{Ni}' in the dQ/dV plot (highlighted by the red arrows).

In order to determine the existence of a high-voltage activity beyond 4.7 V, the upper cut-off voltage was increased to 5.3 V as shown in the dQ/dV plot in Figure 5.19. In the first post thermal cycle (after the preceding discharge), broad oxidation/reduction peaks appear at around 4.7/4.5 V followed by electrolyte decomposition ('ED') beyond 5.1 V. These findings correlate well with the electrochemical characteristics of the $LiNi_{0.5}Mn_{1.5}O_4$ (LNMO) spinel reference (purple area), which crystallizes in the cubic $Fd\bar{3}m$ symmetry[5]. Here, the high-voltage redox activity of $Ni^{2+/4+}$

[5] Strictly speaking the 'disordered' LNMO spinel. The 'ordered' version has the $P4_332$ symmetry [90] (International Tables for Crystallography number 212).

is associated with the reversible de-/lithiation of tetrahedral 8*a* Li sites and the low-voltage activity of $Mn^{3+/4+}$ with the (reversible) de-/lithiation of octahedral 16*c* Li sites, respectively. Since the Li occupancy of the 16*c* sites involves a Jahn-Teller active $Mn^{3+/4+}$ redox couple, this leads to a distortion of the Mn-O_6 octahedron accompanied by a tetragonal distortion of the cubic cell. This is commonly described as 'overlithiation' and leads to a rather fast electrochemical degradation of the material [51, 52]. The small reduction peak at 2.1 V ('S_{Mn2}') can be attributed to the formation of a second tetragonal phase, which corresponds to the lithiation of LNMO-domains with a pronounced Ni/Mn-disorder [53, 91]. As indicated by the absence of the corresponding oxidation peak, this phase is highly unstable and slowly transforms to the first tetragonal phase, for instance, during a resting period.

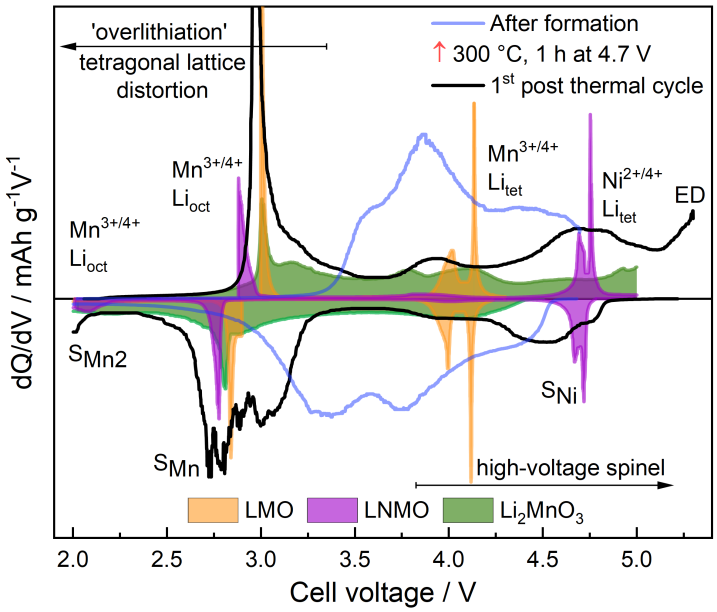

Figure 5.19.: High-voltage extended dQ/dV plot of a 'HE5050' electrode, which was thermally treated in the charged state (4.7 V). The sample was cycled between 5.3 V and 2.0 V with a rate of C/10. For comparison, the 2nd-cycle redox peak positions of $LiMn_2O_4$ (LMO), $LiNi_{0.5}Mn_{1.5}O_4$ (LNMO) and '6-Li_2MnO_3' reference materials are incorporated (not true to scale). They were cycled with a rate of C/50 (1C = 290 mAh/g). Labels: 'S_{Mn2}'/'S_{Mn}'/'S_{Ni}' – Mn/Ni redox activity in a LNMO-like spinel, ED – electrolyte decomposition.

5.3.2. Synchrotron radiation powder diffraction

From the *ex situ* synchrotron radiation diffraction pattern of the charged sample after formation (AF 4.7 V) in Figure 5.20 it can be seen that the pattern of the charged material can still be well described with a rhombohedral $R\bar{3}m$ setting. Thus, the delithiation itself does not induce a long-range alteration of the crystal structure, for example, towards a lithium-poor phase. The even more pronounced broadening of the 018_h reflection (light blue pattern) in comparison to the discharged sample indicates an increase of the lattice strain along with a strong c_h-anisotropic component after the delithiation of the layered lattice. This observation is confirmed by the corresponding results from the Rietveld refinement as will be shown in Figure 5.28 in Section 5.3.5.

After the thermal treatment at 300 °C for 1 hour, clearly visible 'shoulders' appeared at the 003_h and the 101_h reflections. These 'shoulders' can be ascribed to the 111_s and the 311_s reflections of an additional nano-sized spinel phase, which was already observed in the diffraction patterns of discharged samples after heating (see Section 5.2.2). The phase content was refined to 49(5)% (w/w) and further increased to 64(4)% (w/w), after the material had been relithiated. The average apparent domain sizes were refined to approximately 5 nm. A closer look at the 222_s and 400_s reflections reveals that these show a much lower size-induced broadening than the 111_s and

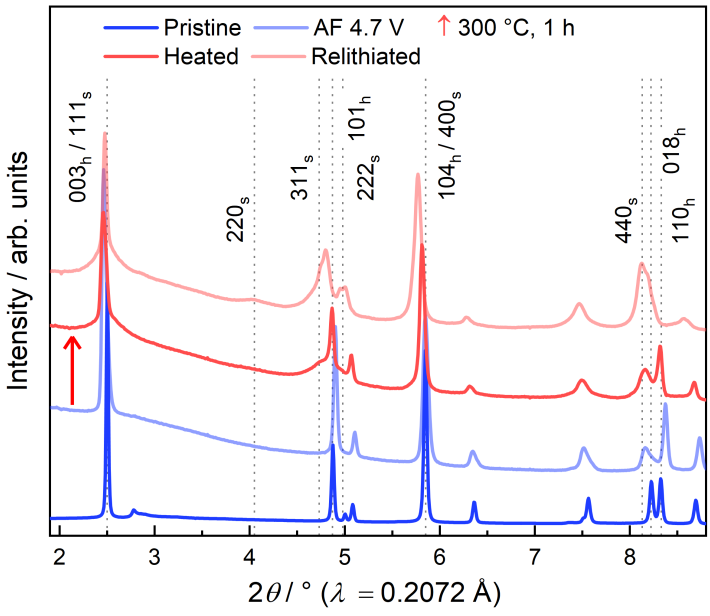

Figure 5.20.: SRPD patterns corresponding to the thermal treatment experiments of charged (4.7 V) 'HE5050' cathode samples. Reflection-subscripts: h – hexagonal setting, s – spinel.

311_s reflections for example. Interestingly, these narrower reflections are strongly related to the oxygen sublattice. In order to include this observation in the structural model, the profiles of the oxygen-associated reflections were refined individually with a Lorentzian-type broadening. The extended model led to an improvement of the fit quality and is discussed in detail in the next section (Section 5.3.3). These results can be interpreted by the local formation/nucleation of nano-sized domains with a spinel-type cation arrangement, which are coherently embedded within a continuous oxygen matrix. The nano-domains and the matrix share the same (slightly distorted) cubic closed packed (ccp) oxygen sublattice, which explains the absence of a size-induced broadening in the oxygen-associated reflections. Overall, these finding are well in agreement with the analysis of the corresponding electrochemical data, where a LNMO-like redox activity was found after the thermal treatment (redox processes 'S_{Mn}' and 'S_{Ni}'). However, no indication was found for the presence of a tetragonal phase in the relithiated sample, which is typical for electrochemically overlithiated LMO/LNMO-type spinels [51, 53].

5.3.3. Structural model of the additional spinel phase

In this section the underlying structural model for the Rietveld refinement of thermally and electrochemically fatigued samples is discussed in detail with a primary focus on the refinement of the additional spinel phase. Therefore, the development of the structural model is demonstrated exemplarily on the basis of the diffraction pattern of a charged 'HE5050' sample (4.7 V), which was heated (300 °C, 1 h) and relithiated (post thermal cycling). As already presented before, the diffraction pattern of this sample clearly shows the presence of a nano-sized spinel phase and thus represents a perfectly suited example for the refinement procedure.

First, the $LiMn_2O_4$ spinel with space group $Fd\bar{3}m$ was added as a second phase to the existing one-phase ($R\bar{3}m$) model 'Model A' as already described in Table 5.1 in Section 5.1.2. The refinement was carried out using additional parameters concerning the second phase (compare Table 5.2): the lattice parameter a_s, the coordinates of the oxygen 32*e* site, the exchange of Li/Mn on the 8*a*/16*d* sites and the parameters associated with the microstructure (size and strain). This two-phase model ($R\bar{3}m$ + $Fd\bar{3}m$) is now titled 'Model B'. Figure 5.21 shows the measured SRPD pattern (red) in

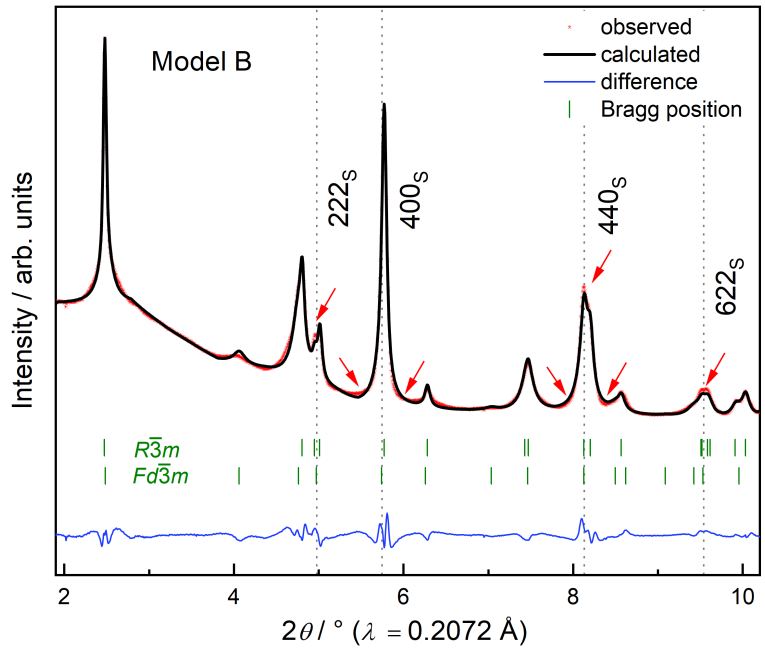

Figure 5.21.: Exemplary Rietveld refinement of the SRPD pattern belonging to a charged 'HE5050' sample (4.7 V) after heating and relithiation using 'Model B'. The deviations between the experimental data and the simulated pattern are highlighted by the red arrows. Reflection-subscripts: s – spinel.

Table 5.2.: 'Model B' and 'Model B_{SRox}': Basis and occupancies of the additional $Fd\bar{3}m$ phase used for refinement of diffraction patterns belonging to highly electrochemically/thermally fatigued samples. Refined parameters are tagged with *. f - exchange of Li/Mn.

Atom	Wyckoff	x	y	z	Occupancy
Li1	8a	0.125	0.125	0.125	1-f*
Mn1	8a	0.125	0.125	0.125	0+f*
Li2	16d	0.5	0.5	0.5	0+f*
Mn2	16d	0.5	0.5	0.5	1-f*
O	32e	0.26232*	0.26232*	0.26232*	1

comparison with the calculated pattern (black) and the resulting difference of the intensities (blue). A closer look at the highlighted reflections reveals (dotted reference lines), that the calculated size- and strain-induced broadening of these reflections is too pronounced (red arrows). As already mentioned before, these reflections are strongly associated with the oxygen sublattice and are shared by the cubic and the trigonal phase. Since their half widths are rather narrow in comparison to other spinel-related reflections, the oxygen sublattice of the nano-sized spinel phase is obviously not significantly affected by the size-induced reflection broadening. This can be interpreted as a coherently embedded nano-sized spinel phase (domains) sharing the same oxygen sublattice as the $R\bar{3}m$ matrix. Or in other words, on the basis of one coherent (slightly distorted) close cubic packed (ccp) oxygen lattice, the cation ordering varies locally with either a more spinel-type or a more layered-type cation arrangement, respectively.

In order to improve the initial 'Model B', individual profile parameters (Lorentzian-type profile broadening) for the 222_s, 400_s, 440_s and 622_s reflections were introduced in a modified model, labeled 'Model B_{SRox}'. In the FullProf suite, this was realized by the addition of 'special reflections' to the program code of the second phase. The resultant calculated pattern as well as the corresponding discrepancy to the measured pattern (blue line) is shown in Figure 5.22. A comparison of selected refined parameters is presented in Table 5.3. Most importantly, the determined spinel content increases noteworthy ('Model B' to 'Model B_{SRox}') from 52(4)% to 64(4)% (w/w), which clearly emphasizes the impact of the selected microstructural model on the evaluation of the experimental data of such an intergrown layered-spinel system. A visual comparison of the two models regarding the $Fd\bar{3}m$ phase is given in Figure 5.23.

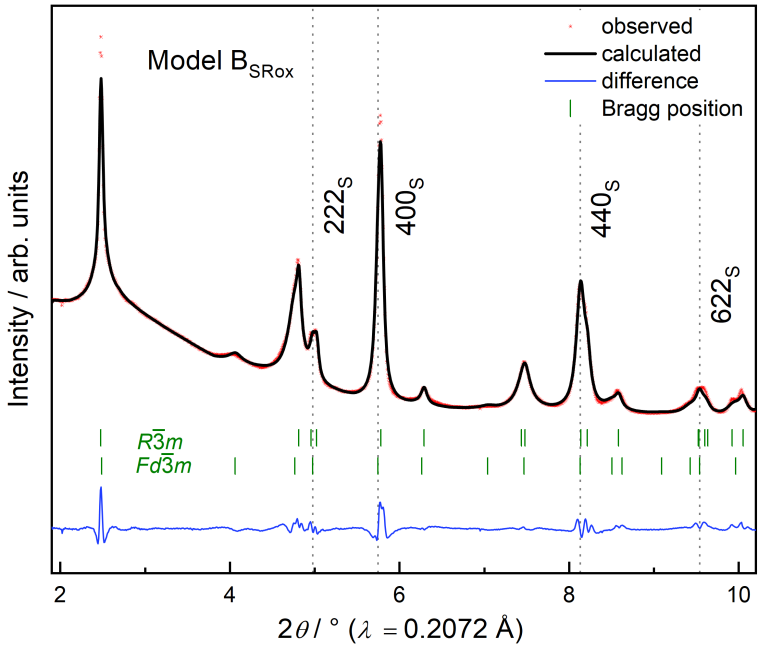

Figure 5.22.: Exemplary Rietveld refinement based on the enhanced 'Model B_{SRox}' of the SRPD pattern belonging to a charged 'HE5050' sample (4.7 V) after heating and relithiation. Reflection-subscripts: s – spinel.

Table 5.3.: Comparison of selected refined parameters using 'Model B' and 'Model B_{SRox}, obtained from the Rietveld refinement of SRPD patterns belonging to a charged 'HE5050' sample (4.7 V) after heating and relithiation.

	Model B		Model B_{SRox}	
χ^2	1.01		0.817	
Phase	$R\bar{3}m$	$Fd\bar{3}m$	$R\bar{3}m$	$Fd\bar{3}m$
Bragg R-factor	2.98	3.21	3.83	3.44
Phase fraction / % (w/w)	48(4)	52(4)	36(4)	64(4)
σ_{max} ⟨anisotropy⟩ / 10^{-4}	80 ⟨8⟩	28	82 ⟨10⟩	34
Average apparent size / Å	-	52	-	46

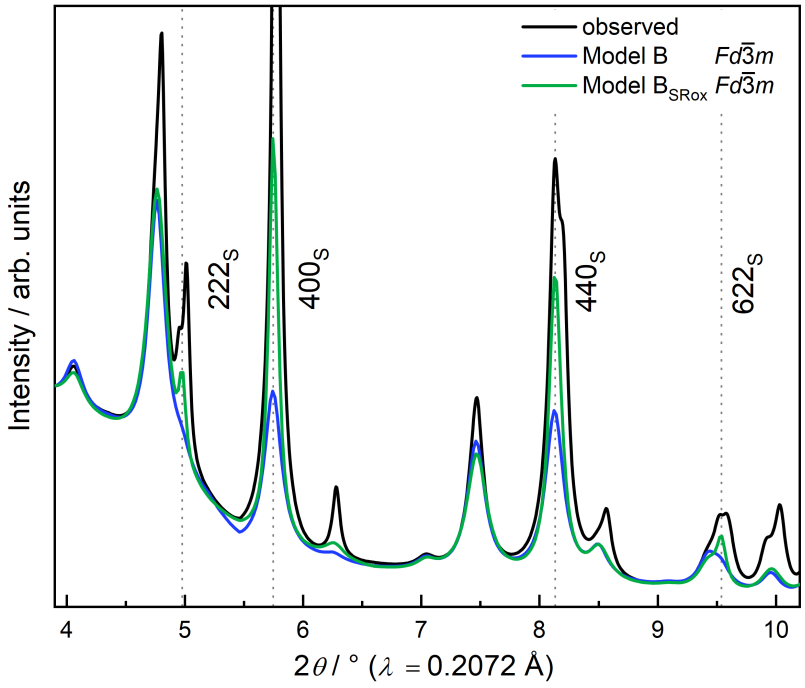

Figure 5.23.: Comparison of simulated patterns regarding the $Fd\bar{3}m$ phase using 'Model B' and 'Model B_{SRox}', obtained from the Rietveld refinement of SRPD patterns belonging to a charged 'HE5050' sample (4.7 V) after heating and relithiation. Reflection-subscripts: s – spinel.

A deconvolution of the calculated pattern using 'Model B_{SRox}' into the single phases and the pure oxygen framework[6] is shown in Figure 5.24. The enhanced structural model ('Model B_{SRox}') was used for the refinement of all 'HE5050' samples in this work. Of course, this enhanced model only affects the refinement of diffraction patterns of highly fatigued samples, which show an additional spinel phase. Regarding the $R\bar{3}m$ phase, this model is identical with 'Model A', which was used for the analysis of the structural changes during the initial formation cycle of the '6-50:50' material (shown in Section 5.1.2).

[6] The simulation (FullProf jobtype 2) of the oxygen framework was carried out by setting the occupancy numbers of Li, Ni, Co and Mn to zero.

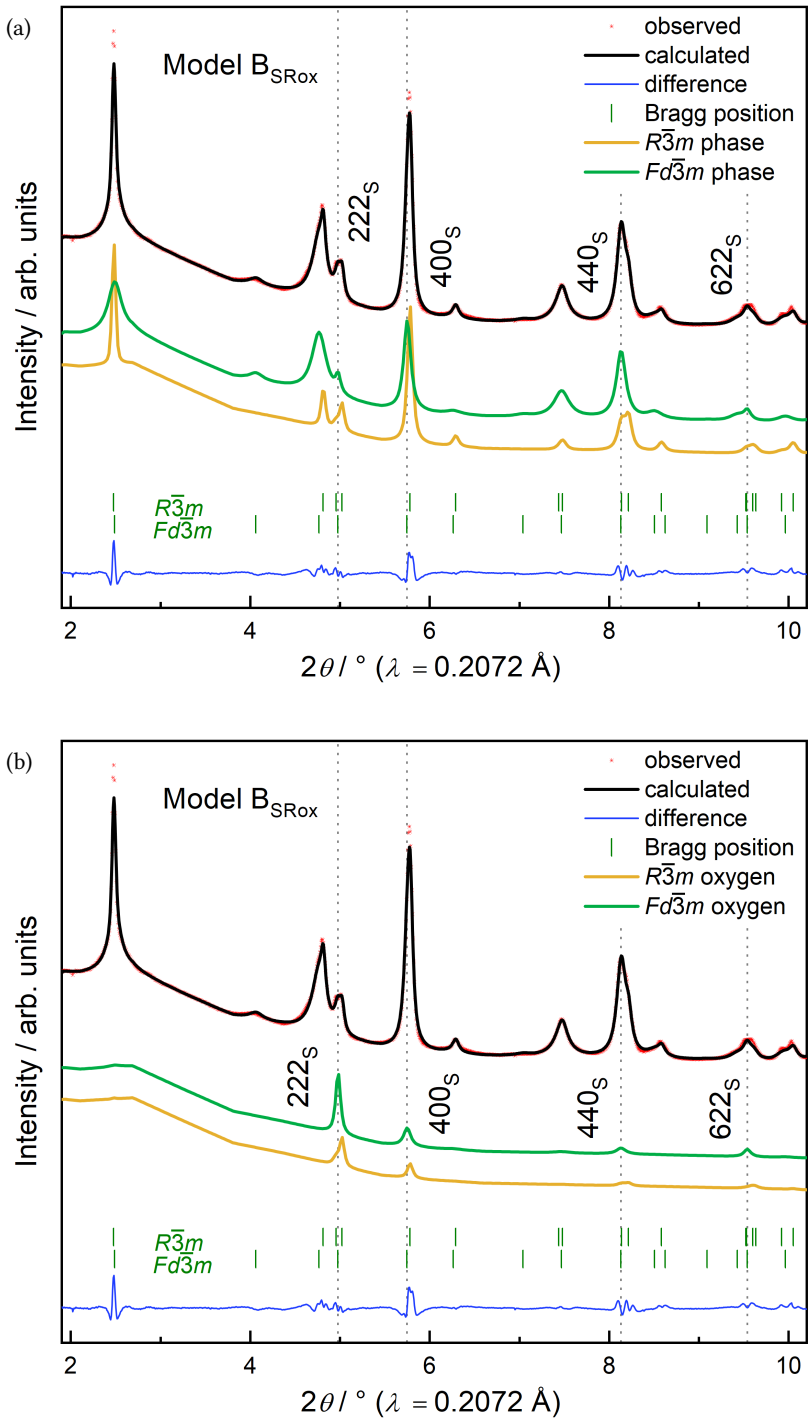

Figure 5.24.: Deconvolution of the calculated diffraction pattern ('Model B_{SRox}') into the single phases (a) as well as a simulation of the pure oxygen framework (b). Reflection-subscripts: s – spinel.

5.3.4. ^{7}Li MAS NMR

As shown in Figure 5.25, the ^{7}Li MAS NMR spectrum of the charged sample after formation is dominated by the broad Li_{Li} resonance indicating an almost complete delithiation of the TM layer. The center of this resonance moved from 615 ppm in the discharged state towards lower NMR shift values of around 555 ppm in the charged state as highlighted by the blue arrow. As already emphasized in Section 5.1.3, three possible explanations for this observation might be: i) the oxidation of Ni, ii) the migration of Li from octahedral to tetrahedral sites, or iii) the preferred delithiation of 'high NMR shift' environments. Additionally, two residual Li_2MnO_3-like peaks at 711 ppm and 1442 ppm are still present in the spectrum of the charged sample. Most probably, the formation (order-disorder transition) has not been fully completed within the first two full cycles. After the heat treatment, the broad Li_{Li} resonance moves back towards higher NMR shifts of approximately 630 ppm. Moreover, the almost symmetric and featureless appearance of the signal

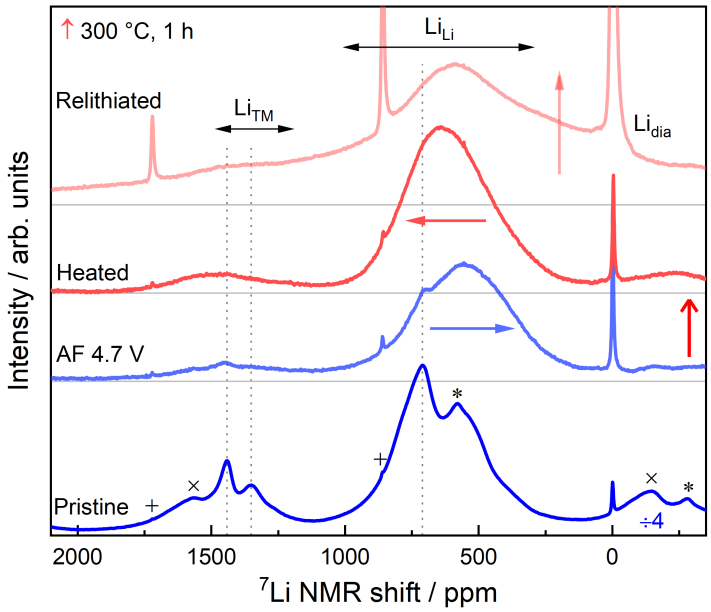

Figure 5.25.: ^{7}Li MAS NMR spectra corresponding to the thermal treatment experiments of charged 'HE5050' samples (4.7 V). Labels: Li_{Li} – Li in Li layers, Li_{TM} – Li in TM layers, Li_{dia} – diamagnetic embedded lithium. The spinning sidebands (±861 ppm) are shown exemplarily in the spectrum of the pristine sample: + (Li_{dia}), × (Li_{Li}) and ∗ (Li_{TM}). For presentation purposes the intensity of the spectrum belonging to the pristine sample is damped by factor 4.

might be an indicator for a more random distribution of the surrounding transition metals [92]. However, whether the remaining lithium is still occupying octahedral sites in a layered-type environment or whether it moved to tetrahedral sites in a spinel-type environment during the thermal treatment cannot be deduced from the data. At least a distinct composition, e.g. of an ordered and well crystallized $LiNi_{0.5}Mn_{1.5}O_4$ or $LiMn_2O_4$ spinel can be excluded at this point, since these would appear as rather sharp resonances at 925 ppm or 520 ppm [59]. Furthermore, the signals at 711 ppm and 1442 ppm are absent in the sample after heating pointing to the dissolution of the aforementioned Li_2MnO_3-like residues.

Interestingly, the spectrum of the relithiated sample (after five post thermal cycles, discharged) features a broad 'bump' at around 250 ppm as highlighted by the red vertical arrow. Due to the broad character, a distinct allocation of the newly formed Li environment(s) is difficult. Two possible explanations might be: i) the occupancy of octahedral 16*c* sites in a $Fd\bar{3}m$ spinel, which was already observed for overlithiated LNMO [93] and LMO [59, 94] as well as for activated Li_2MnO_3 [41], and/or ii) the occupancy of under-coordinated tetrahedral sites (CN<4) due to oxygen vacancies in a still maintained layered framework [15]. Moreover, the spectrum shows a significant increase and broadening of the signal around 0 ppm, which is associated with lithium embedded in a diamagnetic environment. This can be attributed to DMC-insoluble reaction products from the electrolyte salt and/or the post mortem reaction products with air, since the NMR rotors were filled outside the glovebox.

5.3.5. Electrochemical and structural changes below 300 °C

Up to this point, the presented results clearly demonstrate the electrochemical and structural degradation of a charged sample after heating at 300 °C for 1 hour. The electrochemical characteristics are dominated by a LMNO-like spinel along with a profound structural rearrangement towards a cubic symmetry. In order to get a more detailed insight into the transformation process, the experiments were repeated at 150 °C, 200 °C and 250 °C, respectively. Figure 5.26 shows the electrochemical data regarding the initial discharge after heating as well as the fifth post thermal cycle. From the results it is apparent, that the electrochemical degradation intensifies with increasing temperature and can be divided in three different characteristic features: i) The area of the 'O_{def}' region increases gradually at the expense of the higher-voltage regions 'NC' and 'O_{2p}' in the charge and discharge (voltage fade). ii) The difference between the mean charge and discharge voltage increases (hysteresis), which is most clearly demonstrated by the gradual shift of reduction peak 'NC' towards lower voltages as highlighted by the red arrow, whereas the position of the corresponding oxidation peak is rather unaffected. iii) The LNMO-like spinel redox peaks ('S_{Mn2}', 'S_{Mn}', 'S_{Ni}') appear for heating temperatures of 250 °C and 300 °C.

Generally, these observations in the electrochemical data are strongly correlated with determined structural changes, for instance, the appearance of additional spinel-associated reflections in the diffraction patterns, the increase of the refined Ni occupancy in the Li layers as well as the determined mass loss of the electrode after heating (oxygen release). As shown in Figure 5.27, the nano-sized spinel phase is clearly apparent in the in the diffraction patterns of the 250 °C and the 300 °C sample as highlighted by the red arrows. In the following a detailed analysis of selected refined parameters is conducted, which are presented in Figure 5.28. The focus is thereby put on the relithiated samples (five post thermal cycles, discharged) which are represented by the triangular-shaped data points. For the 250 °C and the 300 °C sample spinel contents of 23(5)% and 64(4)% (w/w) were refined with average apparent sizes of 2 nm and 5 nm, respectively. A small amount of spinel was also determined for the 150 °C and the 200 °C sample after heating. However, after the post thermal cycles the refined spinel content decreased to zero again. Interestingly, the emergence of the spinel phase in the diffraction pattern goes along with noteworthy structural changes in the layered $R\bar{3}m$ phase starting at 250 °C as indicated by the red arrows. These alterations are strong indicators for a gradual transformation towards a more spinel-type cation arrangement and a densification of the lattice, i.e. the initially layered phase can now be rather described as kind

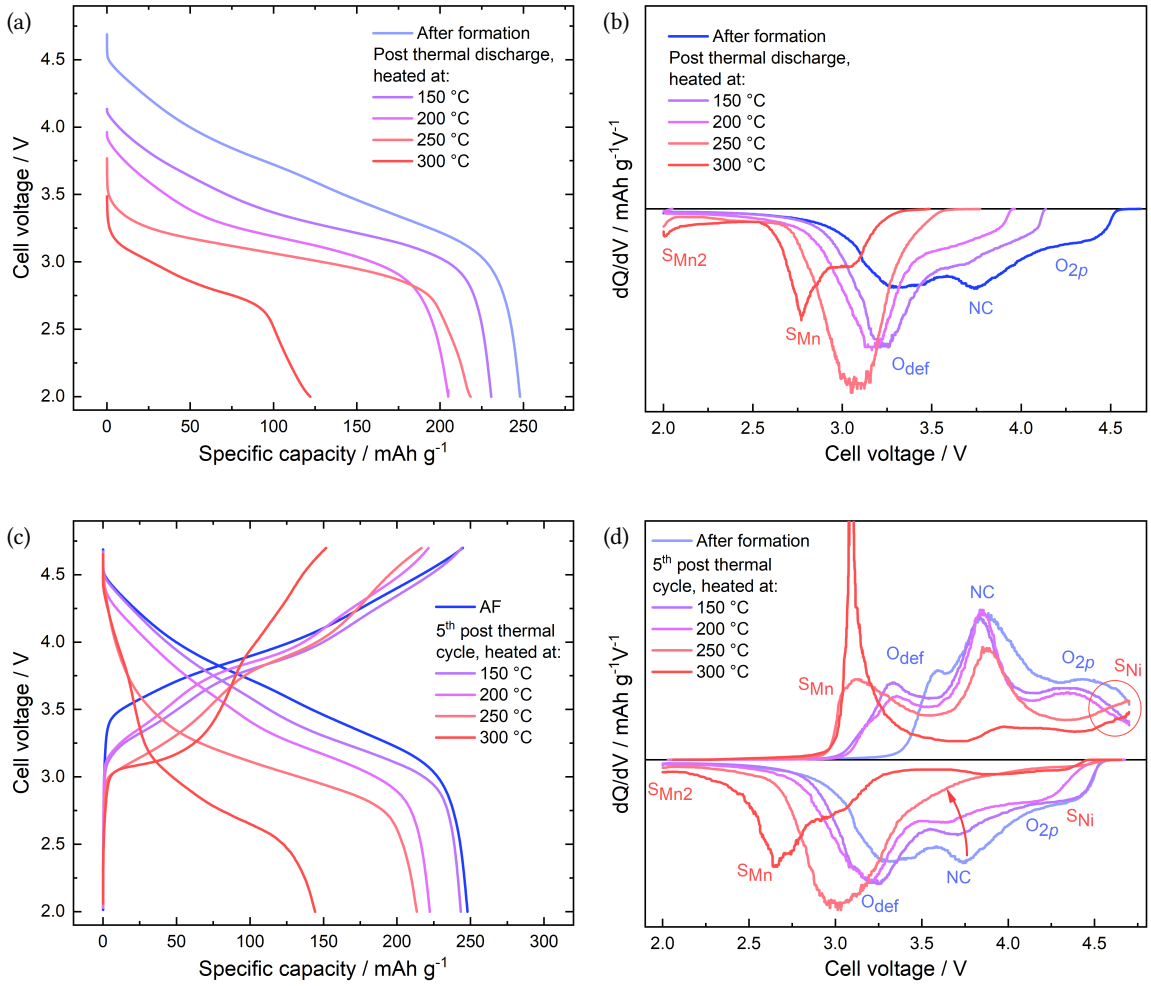

Figure 5.26.: Thermal treatment of charged 'HE5050' samples (4.7 V) at various temperatures ranging from 150 °C to 300 °C: Cell voltage vs. specific capacity plots of the first (a) and fifth (c) post thermal cycles and the thereof derived dQ/dV plots (b,d). Labels: 'NC' – Ni/Co redox activity, 'O_{2p}' – oxygen 2*p* band, 'O_{def}' – defect-associated oxygen redox activity, 'S_{Mn2}'/'S_{Mn}'/'S_{Ni}' – Mn/Ni redox activity in a LNMO-like spinel.

of intermediate spinel-layered structure [12, 95]. The significant alteration of the refined structural parameters can be interpreted as follows:

i) The refined a_h parameter of the layered $R\bar{3}m$ phase increases from 2.8666(1) Å after formation (discharged) to 2.8982(3) Å and 2.8921(4) Å after heating at 250 °C and 300 °C followed by relithiation (discharged), respectively. Since the increase of a_h is an indicator for the expansion of the TM ion radii, in sum a lower oxidation state of the transition metal ions is suggested. Most probably, this also includes the partial reduction of Mn from +IV to +III, which is also found in the corresponding dQ/dV plot of the post thermal cycles (redox process 'S_{Mn}') and indicated in the Mn K-edge and the O K-edge spectra (shown later in Section 5.8).

ii) The drop of the c_h/a_h ratio indicates a decrease of the rhombohedral lattice distortion leading to a more cubic symmetry (c_h/a_h ratio of approximately 4.9).

iii) The determined Ni occupancy in the Li layers raises from 4.7(6)% before to 10.3(6)% and 15.4(9)% after heating at 250 °C and 300 °C followed by relithiation, respectively. This finding suggests a profound migration of transition metals from the TM into the Li layers and thus forming a more cubic cation arrangement. The refined TM occupancy within the TM layers increases significantly at 300 °C (orange arrow in Figure 5.28), which might be due to a densification of the lattice including the release of oxygen from the surface (will be shown in Section 5.6.2) and the migration of cations from the surface to the bulk.

iv) A further indicator of the transition from a layered to a cubic symmetry is the z_O coordinate of the oxygen 6*c* site, which is 0.25 for an ideal ccp oxygen lattice. Here, the initially rhombohedral distortion along c_h direction resulting in two different oxygen layer distances along c_h vanishes, due to a similar Li/TM ratio in the former Li and TM layers. From 250 °C on, a decrease of z_O coordinate in direction of a more cubic cation arrangement (0.25) is apparent.

v) The determined lattice strain increases from 250 °C on, which might be due to the formation of nano-sized spinel domains within the layered matrix (compare Section 5.3.3). A simultaneous increase of the c_h-anisotropy of the lattice strain is not observable.

vi) Importantly, these structural changes are well correlated with the mass loss of the electrode coating (active material, binder, carbon) after heating. Whereas up to 200 °C almost no mass loss (<1% w/w) could be determined, the value increases remarkably for the 250 °C sample to 3.3(6)% and to 9.9(7)% (w/w) for the 300 °C sample, respectively.

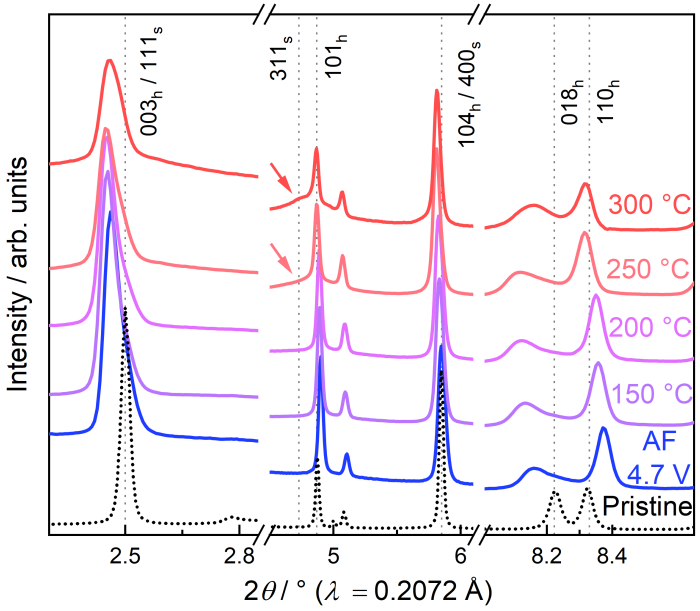

Figure 5.27.: *ex situ* SRPD patterns belonging to the thermal treatment experiments of charged 'HE5050' samples (4.7 V) at various temperatures ranging from 150 °C to 300 °C. Reflection-subscripts: h – hexagonal setting, s – spinel.

In conclusion, these findings clearly indicate a more spinel-type cation arrangement with increasing temperature: by the increase of the refined spinel content and the more 'cubic character' of the layered phase, respectively. This goes along with release of oxygen (mass loss), which is mandatory for the formation of a fully developed spinel phase. These structural changes lead to a profound voltage and capacity fade as it is apparent from the electrochemical data.

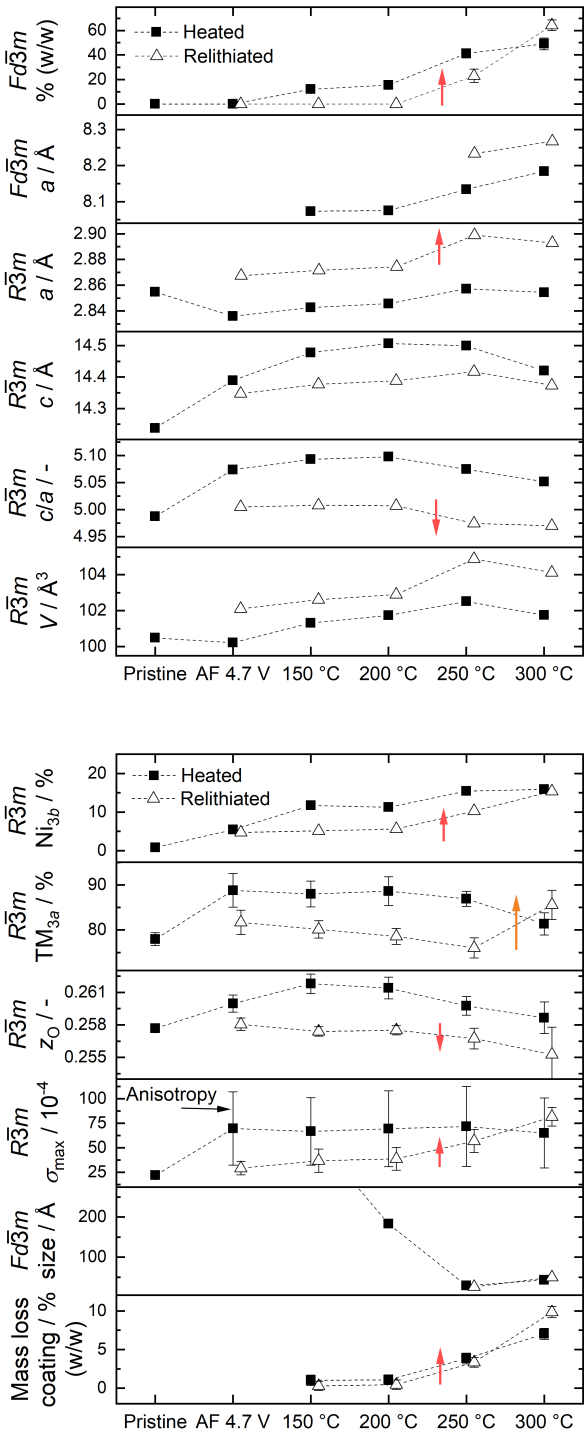

Figure 5.28.: Selected parameters from the Rietveld refinement corresponding to the thermal treatment experiments of charged samples (4.7 V) at various temperatures ranging from 150 °C to 300 °C. The underlying structural model (Model SR_{ox}) of the refinement is described in Section 5.3.3. The dashed lines are inserted as a guide for the eye. $3a$ – TM layer, $3b$ – Li Layer, z_O – z coordinate of the oxygen $6c$ site, σ_{max} – average maximum strain and c_h anisotropy (vertical bars).

5.4. Thermal treatment of samples charged to 4.2 V

In this section the results of heating experiments that were conducted on samples that were charged to 4.2 V after formation are presented. Since the main electrochemical and structural features originating from the thermal treatment procedure were already described in detail in the preceding sections, only the most important outcomes are presented and discussed in the following.

5.4.1. Electrochemical and structural changes at 300 °C

Electrochemical characterization: Figure 5.29a shows the cell voltage vs. specific capacity of the cycle after formation and the charge step to 4.2 V as well as the first and fifth cycle after heating (300 °C, 1 h). In order to emphasize the single redox processes, the corresponding dQ/dV vs. cell voltage curves are plotted in Figure 5.29b. The first post thermal charge starts with the oxidation peak 'NC' at a cell voltage of about 3.7 V belonging to the oxidation of Ni and Co. The oxidation peak 'S_{Ni}' beyond 4.5 V can be assigned to the oxidation of Ni along with the delithiation of LNMO-like spinel environments. In the subsequent discharge step, the dQ/dV plot reveals only a rather weak redox activity until 3.2 V, where the reduction peaks 'O_{def}' and followed by 'S_{Mn}' start to appear. In the second post thermal cycle, the dQ/dV plot clearly demonstrates the reversible de-/lithiation of LMNO-like spinel environments as indicated by the redox peaks 'S_{Mn}' and 'S_{Ni}'. In contrast to the sample which was heated after charging to 4.7 V (see Figure 5.18), the oxidation peaks belonging to the processes 'NC' and 'O_{2p}' are stronger. However, these processes reveal a profound hysteresis and a shift of the corresponding reduction peaks of about 1 V towards lower potentials (highlighted by the red arrow). Furthermore, the capacity fade and the gradual increase of the overvoltage, for instance, indicated by the divergence of the oxidation/reduction peaks of process 'S_{Mn}', are much weaker in comparison to the post thermal cycles of the samples heated at a charging state of 4.7 V (see Figure 5.18). In sum, these observations suggest the presence of a LNMO-like spinel after heating in coexistence with a still layered phase, which is more pronounced than in the sample heated at a fully charged state (4.7 V). Most probably, this leads to a higher stability of the capacity and just a slight increase of the overvoltage during cycling, respectively.
Structural characterization: The analysis of the structure before and after the thermal treatment was carried out by SRPD and ^{7}Li MAS NMR measurements as shown in Figure 5.29c+d. From the diffraction pattern of the sample after heating (red line) the emergence of a second phase can be

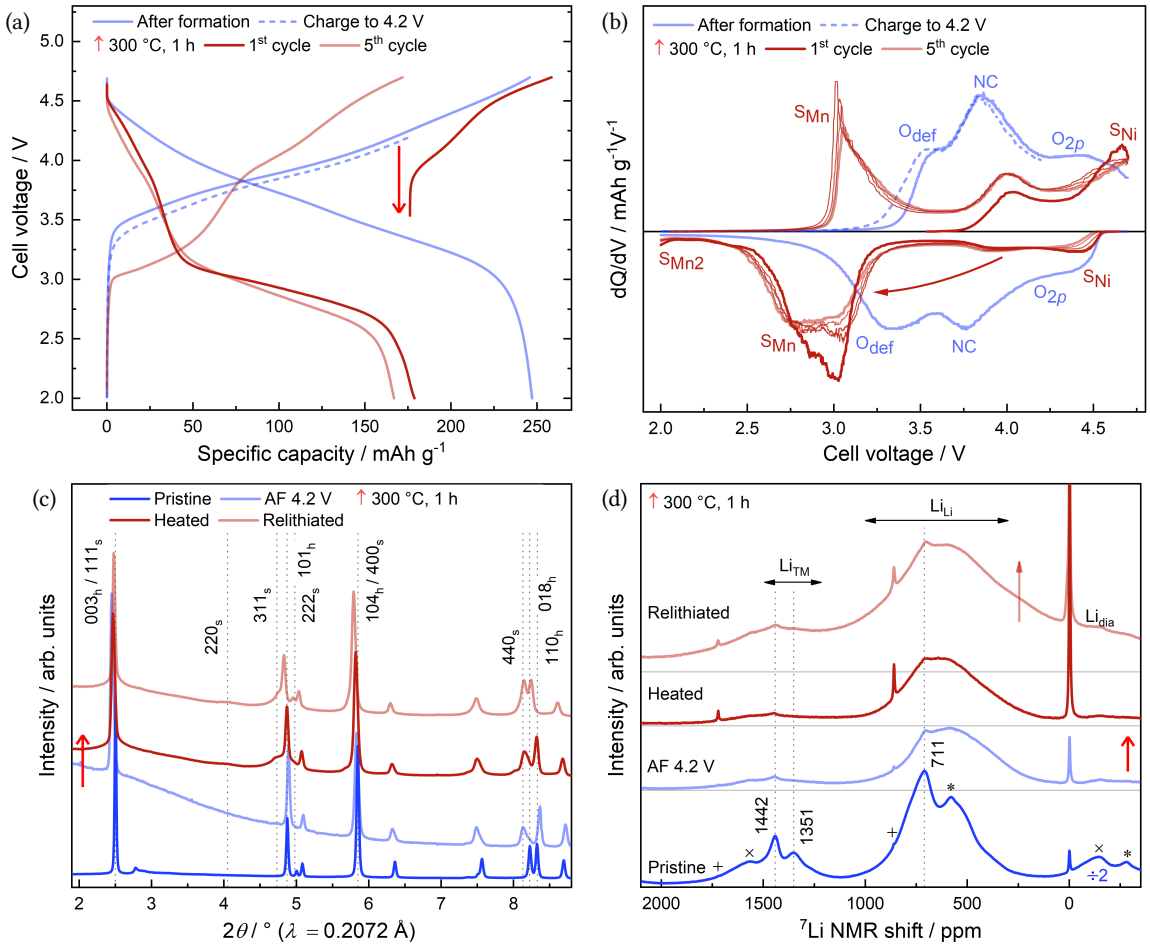

Figure 5.29.: Cell voltage vs. specific capacity (a) and the thereof derived differential capacity (dQ/dV) plot (b) corresponding to the thermal treatment experiments of 'HE5050' cathode samples charged to 4.2 V, which completed the initial formation cycle. Cycling parameters: C/10, 4.7 V - 2 V. The corresponding SRPD patterns and the ^{7}Li MAS NMR spectra are shown in (c) and (d). Labels EC: 'NC' – Ni/Co redox activity, 'O_{2p}' – oxygen 2*p* band, 'O_{def}' – defect-associated oxygen redox activity, 'S_{Mn2}'/'S_{Mn}'/'S_{Ni}' – Mn/Ni redox activity in a LNMO-like spinel. Reflection-subscripts: h – hexagonal setting, s – spinel. Labels NMR : Li_{Li} – Li in Li layers, Li_{TM} – Li in TM layers, Li_{dia} – diamagnetic embedded lithium. The spinning sidebands (±861 ppm) are highlighted exemplarily in the spectrum of the pristine sample: + (Li_{dia}), × (Li_{Li}) and ∗ (Li_{TM}). For presentation purposes the intensity of the spectrum belonging to the pristine sample is damped by factor 2.

identified. Most clearly indicated, for instance, by the appearance of the 311_s reflection. The second phase could be assigned, here as well, to a nano-sized spinel with a refined phase content of 47(7)% (w/w) and a domain size of about 3 nm (refined as $LiMn_2O_4$ with 'Model B_{SRox}', see Section 5.3.3). After the five relithiation cycles, the refined phase content of the spinel reduces to 39(3)% (w/w) and a domain size increases to approximately 5 nm. For comparison, the spinel content of fully charged sample (4.7 V) after the thermal treatment was refined to 49(5)% and to 64(4)% (w/w) after relithiation, respectively. A more detailed presentation of selected refined parameters will be given below.

The ^{7}Li MAS NMR spectrum (see Figure 5.29d), which correspons to the sample after the thermal treatment (red line) only shows minor changes in comparison to the spectrum of the sample before heating (light blue line). The position of the broad signal associated with the Li_{Li} environments only moved slightly towards higher NMR shifts and a small residue of the distinct Li_2MnO_3-like resonances is still identifiable (711 ppm and 1442 ppm). After the subsequent relithiation cycles (light red line), these distinct peaks remain and the entire spectrum becomes significantly broadened. Furthermore, a broad 'bump' is emerging at around 250 ppm as highlighted by the red arrow. This feature was already identified and discussed for the spectrum of the relithiated sample, which was heated at the fully charged state (4.7 V, see Figure 5.25). The occupancy of octahedral 16*c* sites in a $Fd\bar{3}m$ spinel Li environment and/or the occupancy of under-coordinated tetrahedral sites (CN<4) due to oxygen vacancies, were listed as possible explanations.

5.4.2. Electrochemical and structural changes below 300 °C

Figure 5.30 shows the electrochemical characterization of thermally treated 'HE5050' cathode samples charged to 4.2 V, which completed the initial formation cycle. The temperature was varied in 50 °C steps ranging from 150 °C to 300 °C. From the cell voltage vs. specific capacity plot of the first and fifth post thermal cycle (a+c) it is apparent that the voltage and capacity fade intensifies with increasing temperature. Furthermore, the hysteresis is more and more present as indicated by the red arrow. The most significant alteration of the electrochemical properties occurs at the step from 250 °C to 300 °C: whereas until 250 °C no spinel redox activity is identifiable in the dQ/dV plot, the curve of the fifth cycle belonging to the sample heated at 300 °C clearly shows the peaks associated with a LNMO-like spinel ('S_{Mn}' and 'S_{Ni}'). This observation can be directly linked to a profound structural modification including the formation of a nano-sized spinel and the release of oxygen as will be shown in the following.

The diffraction patterns and a selection of refined parameters corresponding to the thermal treatment of samples charged to 4.2 V are plotted in Figure 5.31 and Figure 5.32, respectively. Only for the samples heated at 300 °C, a clear signature of the spinel phase is apparent in the diffraction patterns as highlighted by the red arrow. This observation is well in agreement with a refined spinel content of 39(3)% (w/w) in the relithiated sample and is again correlated with a significant mass loss of the electrode coating (oxygen release).

To sum up, in this section it was demonstrated, that the thermal treatment of Li-rich 'HE5050' samples charged to 4.2 V leads to an obvious degradation of the structure and the electrochemical properties towards a more spinel-type appearance. Similarly to the findings in the previous Section 5.3 (Thermal treatment of samples charged to 4.7 V) the degradation process can be divided into two steps: i) the increase of the voltage fade and the hysteresis along with an increased disorder in the material (migration of TMs from TM into Li layers and increased lattice strain) up to 250 °C, and ii) the formation of nano-sized spinel domains along with the release of oxygen at 300 °C. As a complementary remark, the formation of spinel domains was already obvious at 250 °C in the diffraction patterns as well as in the corresponding dQ/dV plot of the fully charged sample (4.7 V) after heating and relithiation suggesting a higher phase stability of the partially delithiated (4.2 V) electrodes.

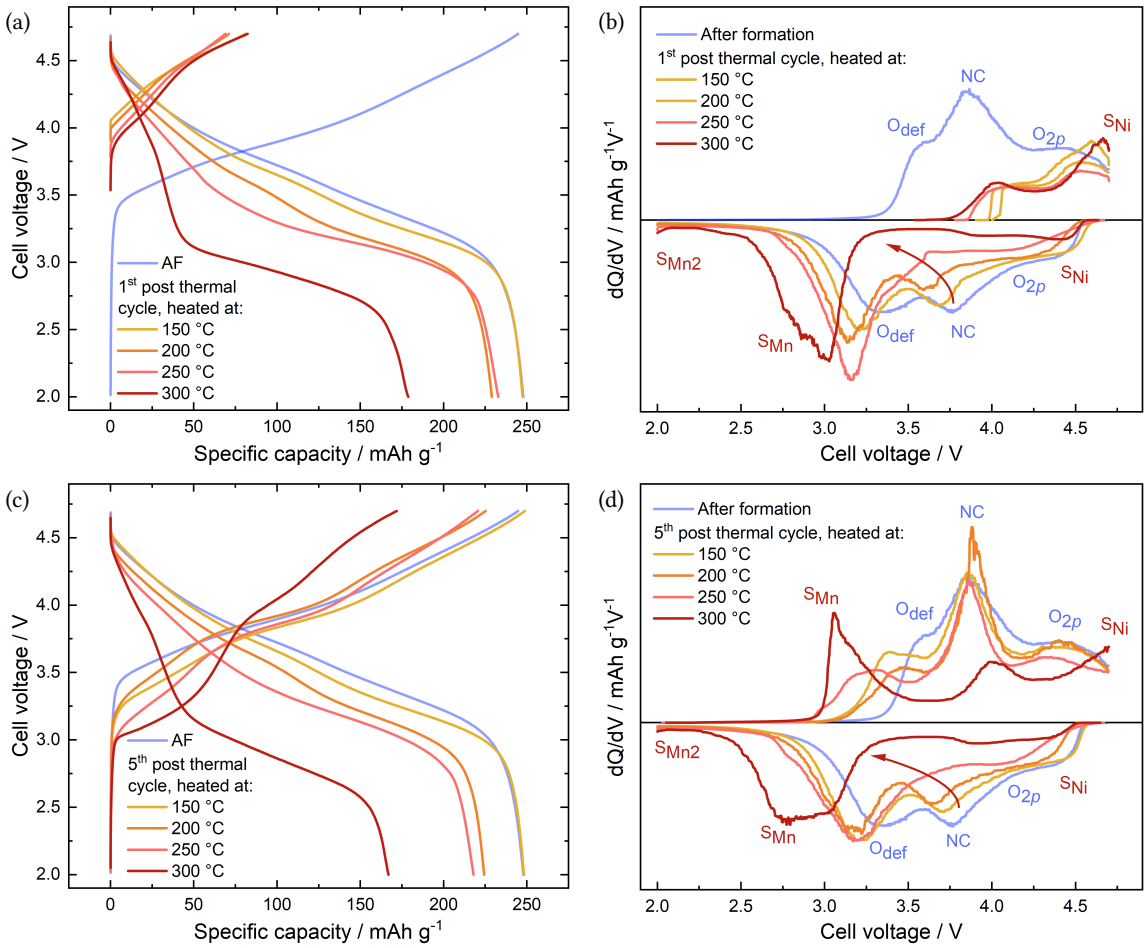

Figure 5.30.: Thermal treatment at various temperatures from 150 °C to 300 °C of 'HE5050' cathode samples charged to 4.2 V, which completed the initial formation cycle: Cell voltage vs. specific capacity plots of the first (a) and fifth (c) post thermal cycles and the thereof derived dQ/dV plots (b,d). Labels: 'NC' – Ni/Co redox activity, 'O_{2p}' – oxygen 2*p* band, 'O_{def}' – defect-associated oxygen redox activity, 'S_{Mn2}'/'S_{Mn}'/'S_{Ni}' – Mn/Ni redox activity in a LNMO-like spinel.

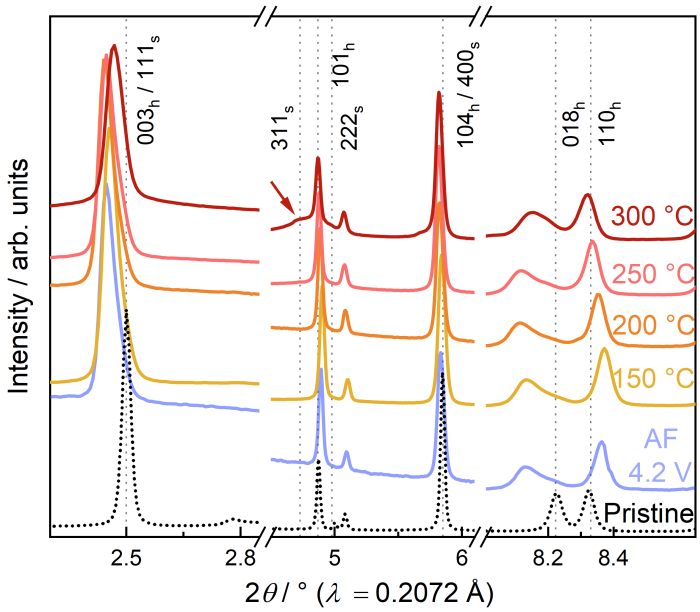

Figure 5.31.: *ex situ* SRPD patterns belonging to the thermal treatment experiments of 'HE5050' samples charged to 4.2 V at various temperatures ranging from 150 °C to 300 °C. Reflection-subscripts: h – hexagonal setting, s – spinel.

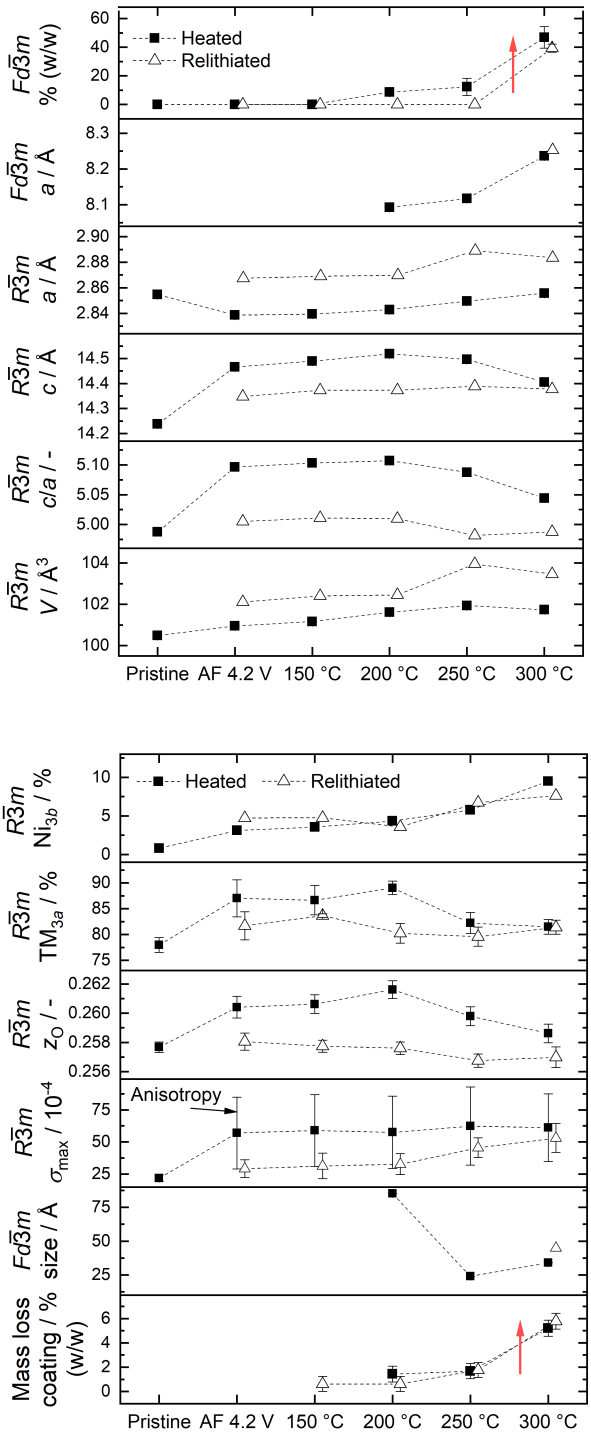

Figure 5.32.: Selected parameters from the Rietveld refinement corresponding to the thermal treatment experiments of 'HE5050' samples charged to 4.2 V at various temperatures ranging from 150 °C to 300 °C. The underlying structural model (Model SR_{ox}) of the refinement is described in Section 5.3.3. The dashed lines are inserted as a guide for the eye. $3a$ – TM layer, $3b$ – Li Layer, z_O – z coordinate of the oxygen $6c$ site, σ_{max} – average maximum strain and c_h anisotropy (vertical bars).

5.5. Thermal treatment of fatigued samples (300 cycles)

In this section, the influence of a thermal treatment on electrochemically fatigued 'HE5050' cathode samples after 300 cycles (discharged to 2.0 V) is studied. The structure and the electrochemical properties before and after heating are investigated in detail using electrochemical characterization, SRPD and ^{7}Li MAS NMR.

5.5.1. Electrochemical characterization

Based on the findings from the thermal treatment of discharged and charged electrodes after formation, the heating experiments were repeated with electrochemically fatigued samples (300 cycles). As can be clearly seen from Figure 5.33a, the extensive cycling resulted in a pronounced voltage and capacity fade. The discharge capacity dropped from 251 mAh/g after formation to 202 mAh/g after 300 cycles, the mean discharge voltage from 3.6 V to 3.2 V, respectively. Overall, this leads to a loss of energy density concerning the discharge step of about 28%.
In the corresponding dQ/dV vs. cell voltage plot in Figure 5.33b, the voltage fade (dashed arrows) and the hysteresis (dotted arrow) are emphasized. The contribution of the low-voltage redox

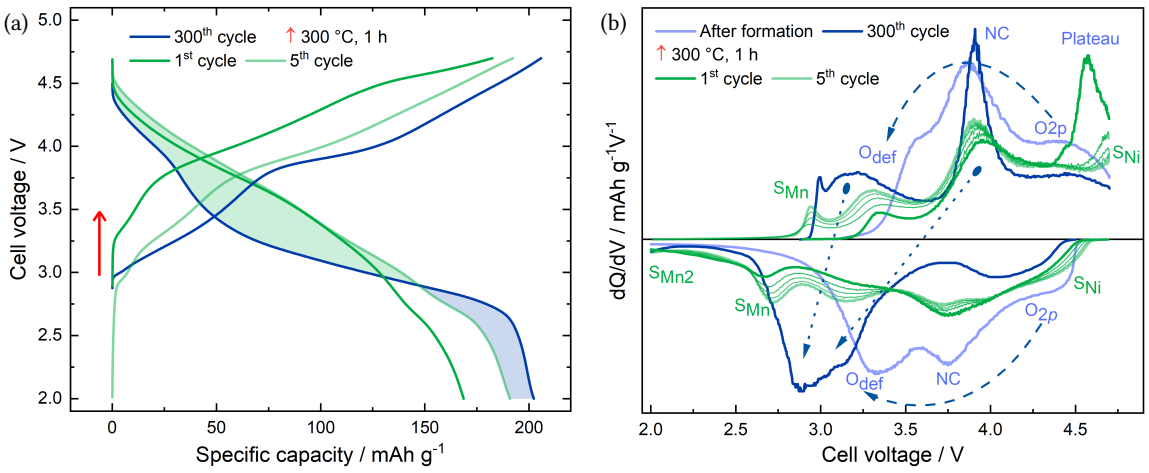

Figure 5.33.: Cell voltage vs. specific capacity (a) and the thereof derived differential capacity (dQ/dV) plot (b) corresponding to the thermal treatment experiments of electrochemically fatigued 'HE5050' cathode samples. Cycling parameters: 4.7 V - 2 V, C/10 (C/5 for the fatigue-cycles, not shown). Labels: 'NC' – Ni/Co redox activity, 'O_{2p}' – oxygen 2*p* band, 'O_{def}' – defect-associated oxygen redox activity, 'S_{Mn2}'/'S_{Mn}'/'S_{Ni}' – Mn/Ni redox activity in a LNMO-like spinel.

processes 'O_{def}' and 'S_{Mn}' increases at the expense of the high-voltage process 'O_{2p}' leading to a decrease of the mean charge/discharge voltage (voltage fade). Whereas in the charging step the oxidation peaks 'O_{def}' and 'NC' are clearly separated, the reduction peak 'NC' completely shifts inside the area of the reduction peak 'O_{def}' in the discharge step. This leads to a charge/discharge voltage difference of the redox process 'NC' of about 0.8 V and thus to a more pronounced hysteresis than in the cycle after formation. After 300 cycles, the spinel-associated redox peak 'S_{Mn}' emerged, but is rather weak and not well-separated from peak 'O_{def}' in comparison to the dQ/dV curves of thermally fatigued samples. The high-voltage redox peak 'S_{Ni}' associated with the formation of a LNMO-like spinel is not identifiable.

Similar to the experiments presented above, the electrochemically fatigued electrode was thermally treated at 300 °C for 1 hour. Most surprisingly, also the cycled Li- and Mn-rich material partially regenerated towards the pristine state as evident from the first post thermal charge (dark green line). The oxidation peaks 'S_{Mn}' and 'O_{def}' are significantly damped in comparison to the cycle before heating and the 'plateau' reoccurs. This observation already indicates the partial recovery of the highly ordered state, however the 'plateau' is less pronounced than in the first post thermal charge of the sample, which was heated directly after formation (compare with Figure 5.11, Section 5.2.1). Another very remarkable finding is the significant intensification of reduction peaks 'O_{2p}' and 'NC' in the subsequent discharge step in comparison to the dQ/dV curve of the fatigued sample. This is directly correlated with the damping of the low-voltage regions 'O_{def}' and 'S_{Mn}'. In other words: The voltage fade and the profound hysteresis have been partially reversed by the thermal treatment.

Again, the partial recovery of the pristine properties is directly connected with the formation of a LMNO-spinel like phase, as apparent from the rise of the spinel-related redox processes 'S_{Mn}' and 'S_{Ni}'. As a reminder, the spinel formation is mandatory for the restoration of the pristine-like phase in order to compensate the lithium deficiency in the material. This deficiency is induced by the initial formation cycle (irreversible capacity loss) and by long-term cycling, respectively. Finally, the first post thermal cycle reached a charge capacity of 182 mAh/g and a discharge capacity of 169 mAh/g. After the five post thermal cycles, two modifications are apparent in the dQ/dV plot: i) the redox activity in the 'NC' area is decreasing again and is intensified in the 'O_{def}' region (voltage fade), and ii) the redox activity of the spinel phase increases within the five cycles, as clearly indicated by the expansion of the area 'S_{Mn}'. Overall, this leads to an increase of the discharge capacity from 169 mAh/g in the first to 191 mAh/g in the fifth post thermal cycle. Furthermore,

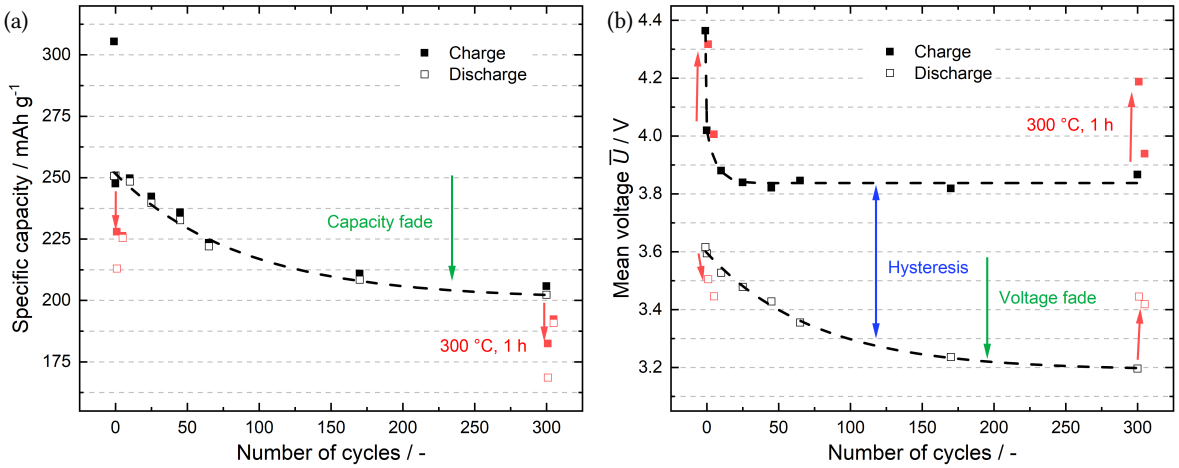

Figure 5.34.: Specific capacity (a) and mean voltage decay (b) with increasing number of cycles. Each set of data points (charge/discharge) represents a different electrode, which was cycled with a rate of C/5 after the formation (C/10) to the desired number of cycles. The last two cycles were again recorded with a rate of C/10 in a new cell in order to exclude a contribution to the detected degradation features, for instance, from the electrolyte and the Li-anode. The electrochemical data regarding the thermal treatment of samples after formation and after 300 cycles is added in red.

the mean discharge voltage increased to 3.4 V in comparison to 3.2 V for the fatigued sample as highlighted by the dyed areas in Figure 5.33a. Figure 5.34 emphasizes the decay of the capacity and mean voltage of the charge/discharge step with increasing number of cycles. Additionally, the impact of the thermal treatment on samples after formation and after 300 cycles is shown (red data points). It is clearly apparent, that the initial mean charge/discharge voltage can be partially recovered by a thermal treatment of an electrochemically fatigued sample. However, the recovery of the high initial capacity is obviously not achievable.

5.5.2. Synchrotron radiation powder diffraction

The data obtained from the diffraction measurement of the electrochemically fatigued electrode powder is presented in Figure 5.35. Selected refined parameters are plotted in Figure 5.36. The diffraction pattern corresponding to the highly cycled sample (dark blue line) reveals a general broadening of the reflections in comparison to the pattern of the sample after formation (light blue line). Especially the emergence of the 311_s reflection already indicates the partial transformation of the sample to spinel. The Rietveld refinement provided a spinel phase content of 34(16)% (w/w) with an average apparent domain size of about 2 nm. This indicates a very fine dispersion of these spinel domains in the layered matrix. Furthermore, the refinement returned a high lattice strain and a strong c_h-anisotropy of the lattice strain in the $R\bar{3}m$ matrix, which is also indicated by the broadened 018_h reflection in the diffraction pattern. This suggests a large variety of locally different degrees of lithiation and probably cation arrangements and/or the loss of electrochemically active lithium sites due to the high degree of disorder in the material.

After the heating procedure, the $C2/m$ superstructure reflections reappear in the diffraction pattern

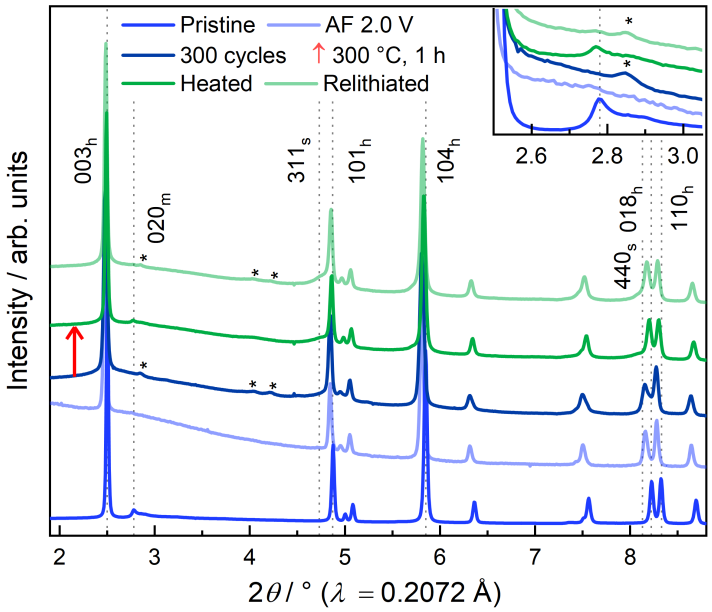

Figure 5.35.: SRPD patterns corresponding to the thermal treatment experiments of electrochemically fatigued (300 cyc) 'HE5050' cathode samples. The $C2/m$ superstructure reflections are magnified in the inset. *Li_2CO_3 associated reflections with space group $C2/c$. Reflection-subscripts: m – monoclinic setting, h – hexagonal setting, s – spinel.

(dark green line) and the 018_h reflection narrows, which clearly demonstrates the partial restoration of the initially well-ordered atomic structure on a long-range scale. The Rietveld refinement provides a spinel content of 21(7)% (w/w) with an apparent domain size of 2 nm, suggesting that within the range of estimated standard deviations no additional material was converted to spinel or the spinel content even decreased during heating. This finding is surprising, since a mass loss of about 4.7(10)% was determined for the electrode coating and therefore suggests the loss of oxygen and the formation of an oxygen-poor phase during the thermal treatment. One explanation could be the very local arrangement of cations in a spinel-type manner without a profound loss of oxygen due to kinetic reasons. Accordingly, this 'excess oxygen' is released during heating. Probably, these results are directly correlated with the findings from the electrochemical characterization (see Figure 5.33). Therefore, no clear evidence was found for a spinel redox activity (represented by 'S_{Mn}' and 'S_{Ni}') after cycling, but clearly appeared after the thermal treatment. A second contribution to mass loss after thermal treatment might be the thermal decomposition of cathode electrolyte interphase (CEI) species.

The overall lattice strain and its c_h-anisotropy decreased to values close to those determined for the sample after formation (emphasized by red arrows), which indicates a pronounced reorganization of the cations in order to reduce high lattice strain, which was clearly apparent before heating. This reorganization process probably also includes a more pronounced segregation of the material into a lithium- and oxygen-rich pristine-like and a lithium- and oxygen-poor spinel phase, respectively. After five post thermal cycles (light green line), the 020_m superstructure reflection vanishes again indicating the loss of the long-range Li/TM-TM_6 honeycomb ordering. The spinel phase content was refined to 27(5)% (w/w) with an average apparent domain size of 4 nm.

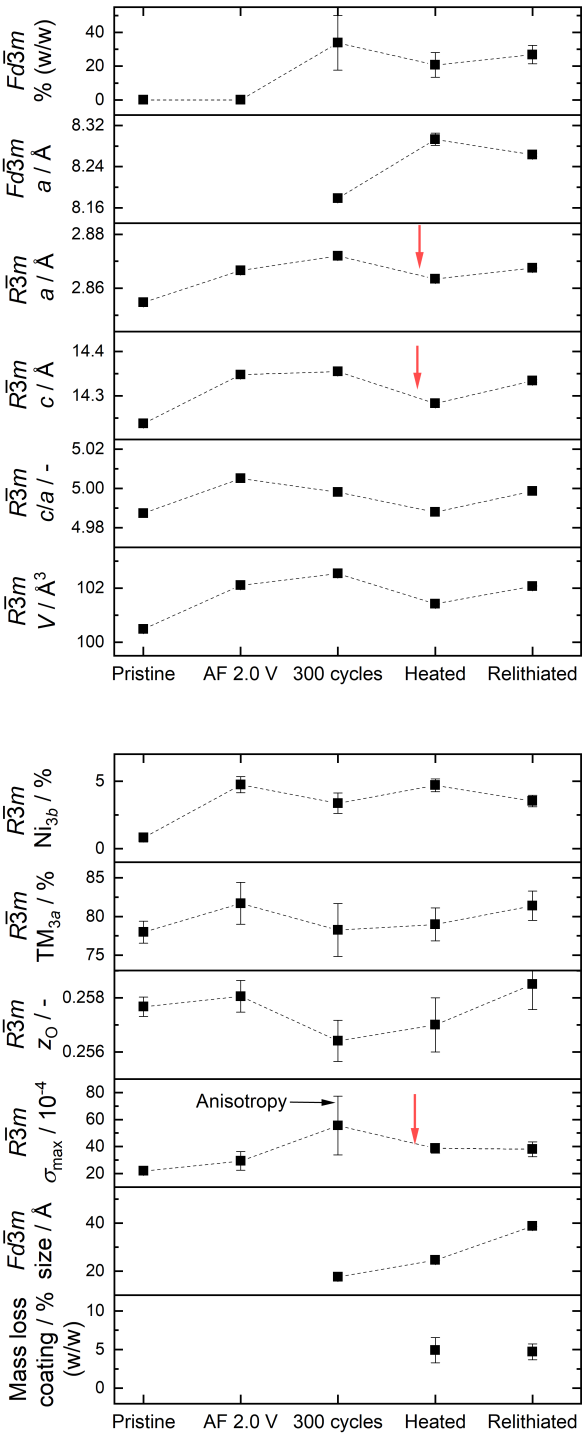

Figure 5.36.: Selected parameters from the Rietveld refinement corresponding to the thermal treatment experiments (300 °C, 1 h) of electrochemically fatigued samples (300 cyc). The underlying structural model (Model SR_{ox}) of the refinement is described in Section 5.3.3. The dashed lines are inserted as a guide for the eye. 3*a* – TM layer, 3*b* – Li Layer, z_O – *z* coordinate of the oxygen 6*c* site, σ_{max} – average maximum strain and c_h anisotropy (vertical bars).

5.5.3. ^{7}Li MAS NMR

The ^{7}Li NMR spectrum belonging to the electrochemically fatigued sample (300 cycles) shown in Figure 5.37 reveals three prominent spectral changes in comparison to the spectrum of the sample after formation (AF 2.0 V): i) all resonances associated with the Li_2MnO_3-like Li-environments (711 ppm, 1351 ppm, 1442 ppm) disappeared, which indicates a completed formation of the entire material and the loss of the Li-TM_6 honeycomb short-range ordering, ii) a newly formed broad resonance aroused at around 250 ppm as highlighted by the blue arrow, and iii) the signal at 0 ppm, which represents the diamagnetic embedded lithium L_{dia} increased significantly. Most interestingly, the 'bump' at around 250 ppm and an increase of the 0 ppm peak area were also observed in the spectrum of a charged electrode after heating and relithiation (compare with Figure 5.25). In order to emphasize the similarities of these spectra, they are superimposed in Figure 5.38a (compare spectrum 'After 300 cycles' with 'Heated at 4.7 V, relithiated'). The overlap of the Li_{Li} and Li_{TM} resonances as well as the emergence of the 'bump' at around 250 ppm (blue and red arrows) suggest

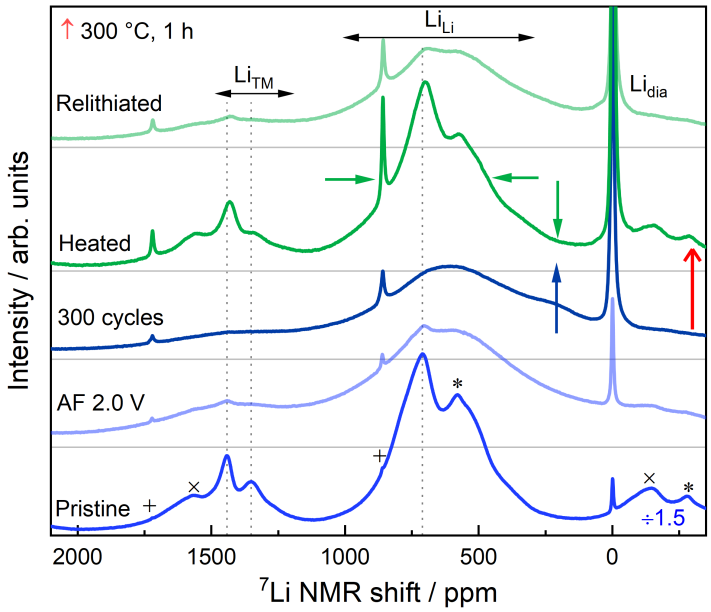

Figure 5.37.: ^{7}Li MAS NMR spectra corresponding to the heating experiments of cycled 'HE5050' samples (300 cycles). Labels: Li_{Li} – Li in Li layers, Li_{TM} – Li in TM layers, Li_{dia} – diamagnetic embedded lithium. The spinning sidebands (±861 ppm) are shown exemplarily in the spectrum of the pristine sample: + (Li_{dia}), × (Li_{Li}) and ∗ (Li_{TM}). The intensity of the spectrum belonging to the pristine sample is damped by factor 1.5.

a rather similar local Li environment in both samples. These findings are very interesting, since both samples share similar features, e.g. a pronounced voltage fade and a trend towards a more spinel-type cation arrangement in the (slightly distorted) ccp oxygen sublattice as revealed by the SRPD measurements. However, the electrochemically fatigued sample still reveals the ability to restore the pristine-like ordering. Most probably, this restoration is possible due to the still intact oxygen sublattice, which suggests no profound oxygen loss during cycling.

Despite the profound structural and electrochemical degradation, the heat treatment of the fatigued sample led to an almost entire recovery of the pristine local ordering in the whole bulk material. As can be clearly seen from the dark green spectrum in Figure 5.37, the resonances associated with the local Li-TM_6 honeycomb ordering in the transition metal layers reappear (1351 ppm and 1442 ppm), which is well in agreement with the return of the $C2/m$ superstructure reflections as shown before. In addition, the 711 ppm resonance, which represents the Li_2MnO_3-like environments in the Li layers is present again. Interestingly, the 'bump' at 250 ppm vanished (dark green arrow) and does not reappear after the relithiation cycles. Obviously, the Li environments observable at low-ppm values around 250 ppm ('bump') are directly linked with a decrease of the mean charge and discharge voltages (voltage fade). This hypothesis is also valid after the subsequent five post thermal cycles. The spectrum is broadened again and distinct Li_2MnO_3-like signals vanished. The 'bump' does not reappear, which is well in agreement with the corresponding electrochemical properties, where the defect-associated low-voltage process 'O_{def}' is significantly damped.

Figure 5.38a+b show a comparison of the ^{7}Li NMR spectra of pristine-like and relithiated samples. The local Li environment still appears rather similar in each set (b,c) of spectra unregarded of the sample's history, which is surprising due to the high refined spinel content in the electrochemically fatigued sample. Overall, this comparison suggests a rather intricate nano-/microstructure in the thermally and electrochemically fatigued samples, which needs to be further investigated by transmission electron microscopy imaging methods. As a general remark, changes in the local Li environment, due to heating or electrochemical cycling, affect the ^{7}Li NMR spectrum as a whole, i.e. (almost) the entire bulk material is modified. Thus it can be concluded that the thermal treatment does not lead to a significant amount of electrochemically inactive cathode particles, for instance, due to the loss of the electrical connection between active material and conductive carbon. Therefore, the observed capacity fade for electrochemically and thermally fatigues samples can be mainly ascribed to structural changes within the cathode material itself.

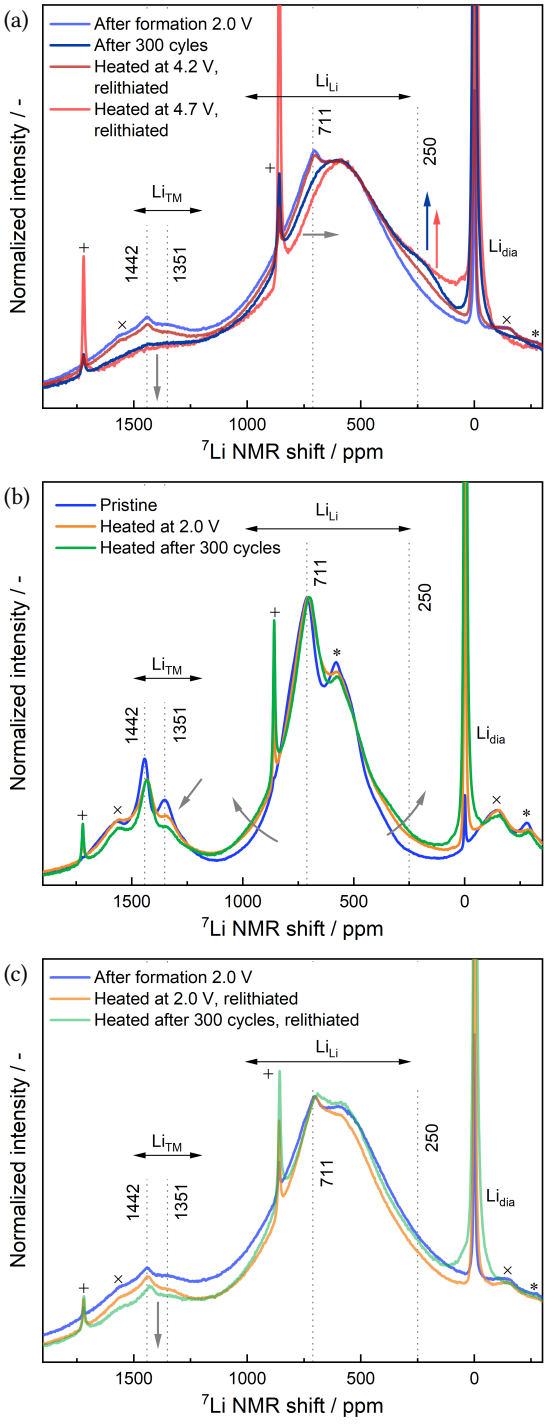

Figure 5.38.: Normalized ^{7}Li MAS NMR spectra corresponding to the thermal treatment experiments of electrochemically fatigued 'HE5050' samples (300 cycles) in comparison with samples, which were heated directly after formation. Labels: Li_{Li} – Li in Li layers, Li_{TM} – Li in TM layers, Li_{dia} – diamagnetic embedded lithium. The spinning sidebands (±861 ppm) are shown exemplarily in the spectrum of the pristine sample: + (Li_{dia}), × (Li_{Li}) and ∗ (Li_{TM}). The spectra were normalized with respect to the 600 ppm (a), 711 ppm (b) and 703 ppm (c) peak height.

5.6. Mass loss during heating

5.6.1. Thermogravimetric analysis

Thermogravimetric analysis (TGA) was performed for the pristine 'HE5050' electrode as well as for electrodes charged to 2.0 V, 4.2 V and 4.7 V, which experienced the formation cycle. The results are shown in Figure 5.39. From the data it is apparent, that the curve corresponding to the fully charged electrode (4.7 V) shows a stronger mass loss and an earlier onset of the gas release in comparison to the curve of discharged electrode (2.0 V). These findings clearly demonstrate a higher thermal instability of the Li- and Mn-rich materials at high degrees of delithiation. Especially the curve of the fully charged electrode (4.7 V) suggests a highly thermally unstable structure with two significant drops of the sample mass at around 300 °C and 400 °C, respectively. As highlighted in the graph, the polymer binder (PVDF) starts to decompose above 375 °C according to the data sheet of the material manufacturer. Therefore, it is considered that a thermal treatment of electrodes up to 300 °C does not significantly affect the integrity of the electrode compound (active material, binder, carbon) regarding electronic conductivity as well as mechanical stability.

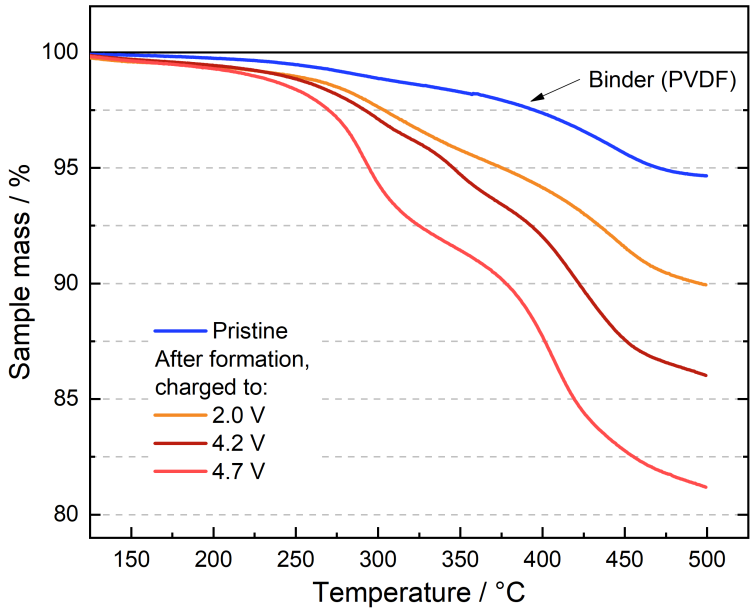

Figure 5.39.: TGA curves obtained for a pristine electrode and electrodes after formation charged to 2.0 V, 4.2 V and 4.7 V (sample mass = active material, carbon, binder, 87:7:6 mass ratio) until 500 °C in argon atmosphere.

Commonly the observed mass loss in layered oxide cathode materials is ascribed to an extensive oxygen release with a simultaneously occurring structural phase transition. This was demonstrated, for instance, by Bak et al. in a combined *in situ* diffraction and mass spectroscopy heating study for a overcharged $Li_{0.1}Ni_{0.8}Co_{0.15}Al_{0.02}O_2$ cathode [88]. With increasing temperature, the material undergoes a phase transition from the layered $R\bar{3}m$ to the cubic $Fd\bar{3}m$ spinel and finally to cubic $Fm\bar{3}m$[7] rock salt symmetry along with the release of oxygen (detected as O_2 and CO_2). The quantitative analysis of the released oxygen is a rather difficult task, since the measured mass loss or quantity of released gas may also partially origin from electrolyte residues, electrode additives (carbon and binder) and/or their reaction products. Nevertheless, a rough estimation of the released oxygen is carried out in the next Section 5.6.2.

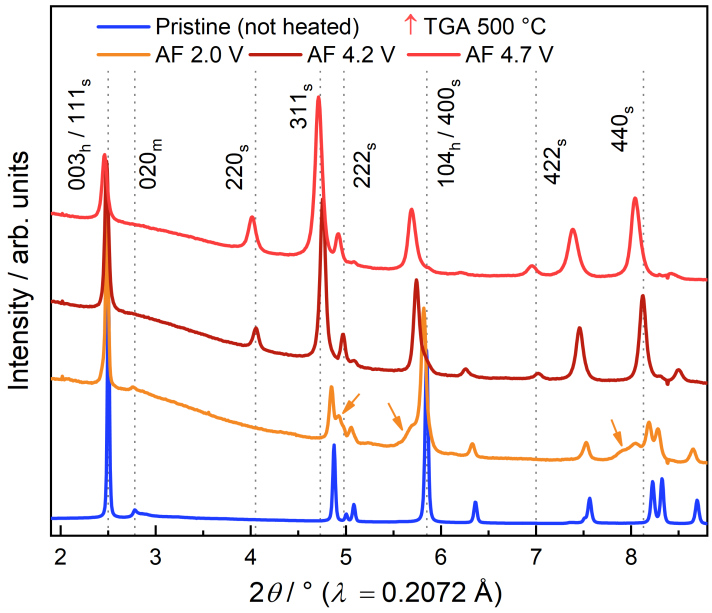

Figure 5.40.: *ex situ* SRPD patterns belonging to electrode powders used for the thermogravimetric analysis, which reached a maximum temperature of 500 °C. Reflection-subscripts: m – monoclinic setting, h – hexagonal setting, s – spinel.

After the TGA measurements, the thereof derived electrode powder was further analyzed by SRPD. The results are presented in Figure 5.40. In the diffraction pattern of the sample heated after discharge (2.0 V), two main phases can be identified: the initial layered phase as well as a newly occurring nano-sized cubic rock salt phase with space group $Fm\bar{3}m$, which is highlighted by the orange arrows. The refinement determined a weight fraction of the cubic phase of 35(9)% with

[7] International Tables for Crystallography number 225

an average apparent domain size of 4 nm. The corresponding plot of the experimental and the simulated pattern is appended in Figure E.8. Additionally, the presence of the $C2/m$ superstructure reflection 020_m indicates the partial recovery of the long-range Li/TM-TM_6 honeycomb ordering. As a reminder, the $C2/m$ superstructure reflections are absent in respective pattern of the material before heating, due to the loss of long-range ordering after the formation cycle (see Section 5.2.2). The diffraction patterns, belonging to the samples heated at higher charging states (4.2 V and 4.7 V), clearly present the layered to spinel transformation. The emergence of the 220_s and the 422_s reflection suggests the occupancy of the spinel tetrahedral 8*a* sites ($Fd\bar{3}m$) with transition metal ions. As a remark, these reflections are exclusively associated with the occupancy of the 8*a* site with ions high in electron density, i.e. the occupancy with lithium does not lead to a noticeably increase of the reflection intensity. This observation suggests a strong ion exchange between the 8*a* site (predominantly Li) and the 16*d* site (predominantly Mn) and/or the partial densification of the lattice towards a TM_3O_4-type spinel.

5.6.2. Cathode mass loss after heating

Table 5.4 shows the determined mass loss after thermal treatment (300 °C, 1 h) of a pristine 'HE5050' electrode, of electrodes after formation charged to 2.0 V, 4.2 V and 4.7 V as well as of an electrochemically fatigued sample (300 cycles). These values directly belong to the samples which were used for the post thermal electrochemical characterization and the structural characterizations (SRPD and NMR), respectively. In the following, a rough estimation of the oxygen loss during the thermal treatment and the resulting oxygen to transition metal ratio (O/TM) in dependence of the selected lithium content x is derived. For the estimation two different approaches were utilized. First, the oxygen loss was directly determined from the mass loss of the respective electrode, while neglecting further gas-releasing decomposition reactions. Since the exact species of the released gas(es) is unknown, the calculation was carried out with CO_2 (lower limit) and O_2 (upper limit) as released molecules, respectively. In a second approach, the oxygen loss during heating was determined based on the restoration of the initial oxidation states present in the pristine state (Ni+II, Co+III, Mn+IV, O-II). The overall increase of the oxidation state (concerning TM and O) in dependence of the degree of delithiation is $-x$ per formula unit, where x is representing the selected lithium content per formula unit. It is assumed, that $1.2 - x$ electrons per formula unit are provided by the release of oxygen during heating in order to reduce the transition metals and the oxygen, as demonstrated by Equation 5.1:

$$\overset{+1}{\mathrm{Li}}_x[\mathrm{Ni}_{0.15}\overset{-x}{\mathrm{Co}}_{0.1}\mathrm{Mn}_{0.55}\mathrm{O}_2] \xrightarrow{300\,^\circ\mathrm{C}} \overset{+1}{\mathrm{Li}}_x\overset{+2}{\mathrm{Ni}}_{0.15}\overset{+3}{\mathrm{Co}}_{0.1}\overset{+4}{\mathrm{Mn}}_{0.55}\overset{-2}{\mathrm{O}}_{2-\delta} + (1.2 - x)/4\overset{0}{\mathrm{O}}_2 \uparrow, \qquad (5.1)$$

where x is the lithium content and δ the oxygen loss per formula unit, which is equal to $(1.2 - x)/2$. The lithium contents x are derived from the electrochemical data neglecting side reactions (the reached charge/discharge capacities are fully dedicated to Li extraction/insertion). The thereof derived oxygen loss δ and the resulting O/TM ratio are presented in Table 5.4.
By comparison of the values is is apparent, that both approaches deliver a rather similar result, which supports the hypothesis regarding the restoration of the initial oxidation states present in the pristine material. This will be further investigated in detail by X-ray absorption spectroscopy studies presented in Section 5.8. As already suggested by the TGA measurements, the mass loss during heating is more pronounced for higher states of charge and leads to a significant release of oxygen, for example, about one quarter of the initial oxygen content for the sample heated after charging to 4.7 V.

Table 5.4.: Estimation of the oxygen loss δ and the O/TM ratio after the heating step (300 °C, 1 h) in $Li_xMn_{0.55}Ni_{0.15}Co_{0.1}O_{2-\delta}$ in dependence of the selected lithium content x. The error of the mass loss was calculated according to the specifications of the used balance.

			Derived from mass loss as CO_2 / O_2		Expected from charge compensation	
Sample	Mass loss / %	x	δ	O/TM ratio	δ	O/TM ratio
Pristine electrode	0.9(6)	1.2	0.04 / 0.05	2.5 / 2.4	0	2.5
AF charged to 2.0 V	2.2(6)	1.05	0.10 / 0.13	2.4 / 2.3	0.07	2.4
AF charged to 4.2 V	5.8(6)	0.525	0.24 / 0.33	2.2 / 2.1	0.34	2.1
AF charged to 4.7 V	9.9(7)	0.25	0.44 / 0.60	2.0 / 1.8	0.47	1.9
Fatigued, 300 cycles	4.7(10)	0.9	0.20 / 0.28	2.3 / 2.2	0.15	2.3

In order to obtain a more detailed picture regarding the structural transformations during heating, the above described calculations (first approach) were repeated for the whole set of data ranging from 150 °C to 300 °C. Figure 5.41 shows the measured mass loss of the electrodes in dependence of the heating temperature and Figure 5.42 illustrates the thereof derived oxygen content as well as the O/TM ratio. A profound change of the O/TM ratio can be an indicator for the transition of the Li- and Mn-rich material towards a 'densified' layered $LiTMO_2$ and/or a spinel $LiTM_2O_4$ stoichiometry with O/TM = 2. Except for the last data points (300 °C) belonging to the sample charged to 4.7 V after formation, all other data points can be still assigned to an oxygen-rich stoichiometry with O/TM ratio larger than 2. Interestingly, these samples demonstrate the typical Li- and Mn-rich electrochemical features, e.g. a profound hysteresis and an oxygen redox activity ('O_{def}' and 'O_{2p}' redox peaks). After reaching the O/TM ratio of 2 or even lower, the material loses the Li- and Mn-rich characteristics and is similar to a LNMO-like spinel, i.e. the redox processes 'S_{Mn}' and 'S_{Ni}' are dominating the charge compensation during de-/lithiation.

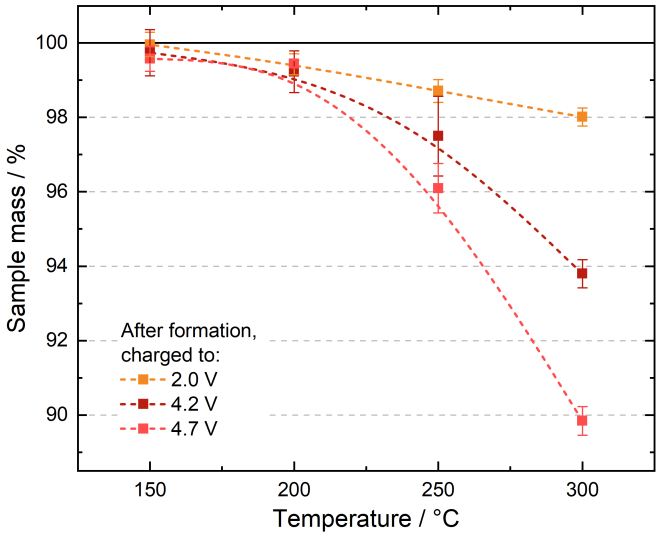

Figure 5.41.: Measured mass loss of electrode samples charged to 2.0 V, 4.2 V and 4.7 V in dependence of the selected heating temperature. Sample mass = active material, carbon, binder, 87:7:6 mass ratio. The data points represent the mean value and the corresponding standard deviation calculated from three identically treated samples. The dashed lines are inserted as a guide for the eye.

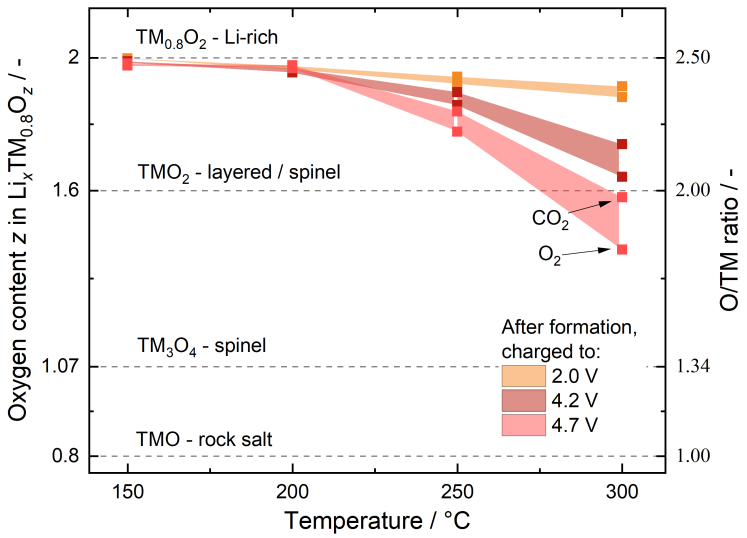

Figure 5.42.: Estimation of the O/TM ratio in dependence of the selected heating temperature for electrode samples charged to 2.0 V, 4.2 V and 4.7 V. The two data points of each configuration represent the assumed released gas species (CO_2 and O_2). The lines are inserted as a guide for the eye.

5.7. Scanning electron microscopy

In this section, thermally treated cathodes are analyzed regarding alterations of their particle surface or morphology. Therefore, scanning electron microscopy (SEM) images of a pristine 'HE5050' electrode as well as of electrodes after heating and post thermal cycling were taken. Since a significant dissolution of TMs from the surface of the heated electrodes was expected during the post thermal cycles, SEM and energy-dispersive X-ray spectroscopy (EDX) were conducted on the respective lithium metal anodes used for these cycles.

5.7.1. SEM imaging of cathodes

Figure 5.43 shows an overview SEM image of a 'HE5050' cathode after heating at a charging state of 2.0 V and post thermal cycling. The particles are arranged in a hierarchical structure with micrometer-sized secondary particles composed of nano-sized primary particles. The manufacturer (TODA) provided a D10 and D90[8] (secondary) particle diameter of 2.9 µm and 4.6 µm as well as a surface area of 3.9 m^2/g, respectively.

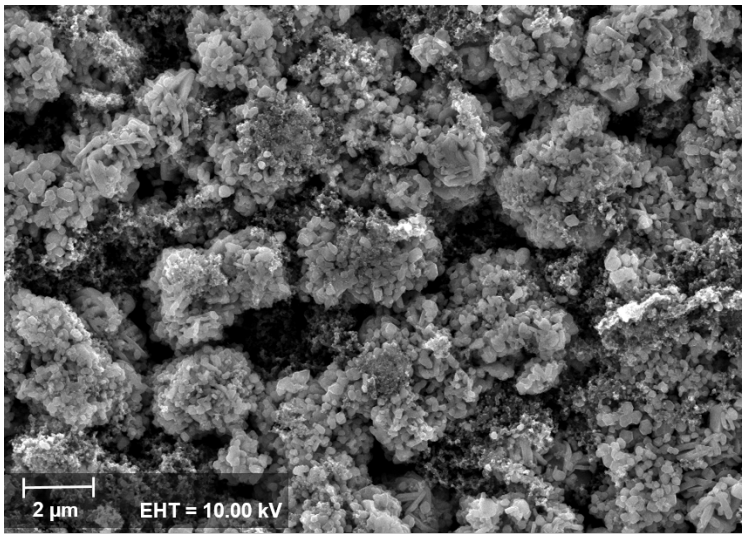

Figure 5.43.: Overview SEM image of a 'HE5050' electrode (electrode compound with binder and carbon) after heating at a charging state of 2.0 V and post thermal cycling. The electrode was rinsed in DMC and dried in advance of the measurement.

[8] D10/D90 is the (secondary) particle diameter at which 10%/90% of the sample's mass is comprised of particles with a diameter less than this value.

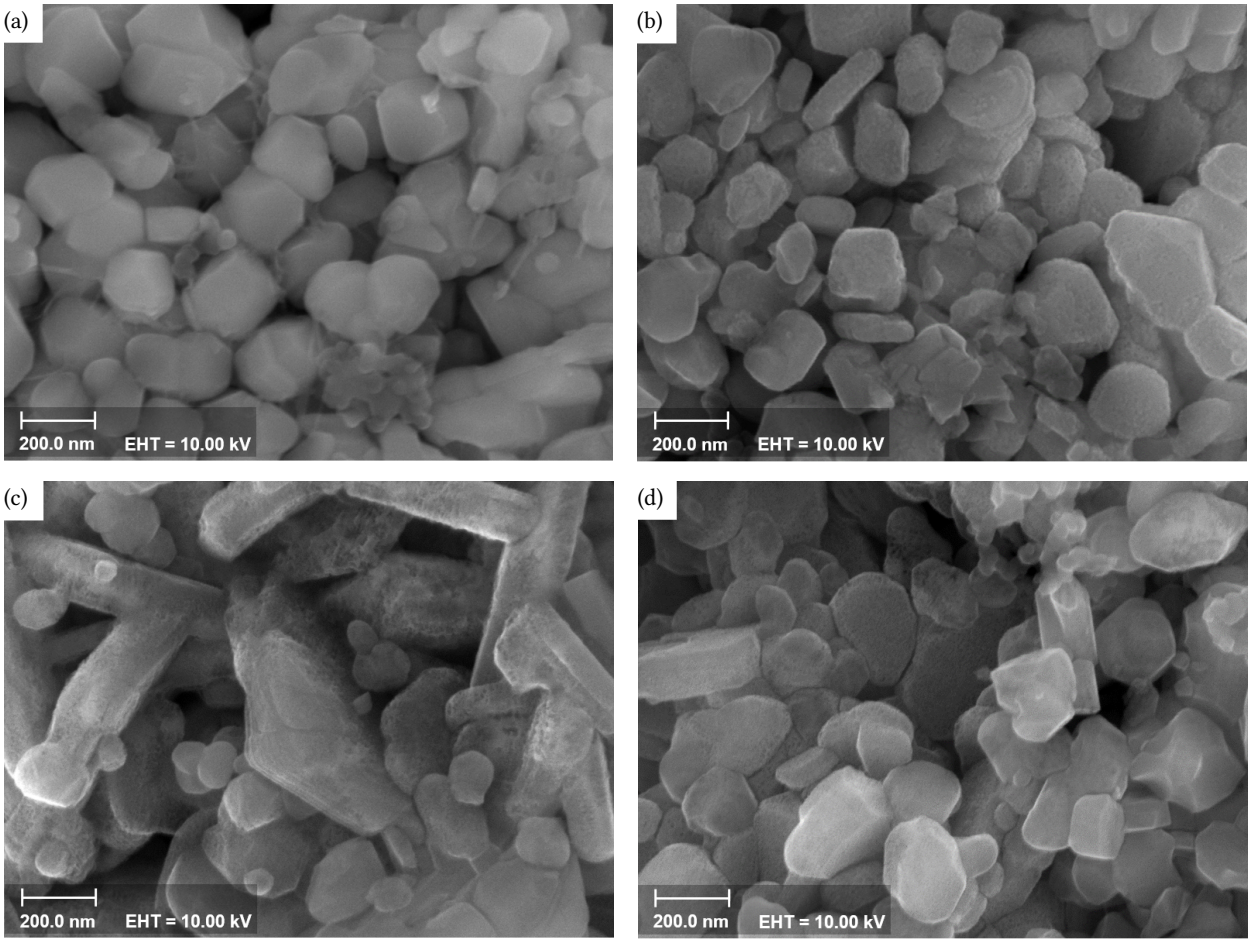

Figure 5.44.: SEM images of a pristine (a) 'HE5050' sample (electrode compound with binder and carbon) as well as cathodes after heating at charging states of 2.0 V (b), 4.2 V (c) and 4.7 V (d) followed by post thermal cycling (relithiation). The electrodes were rinsed in DMC and dried in advance of the measurements.

Figure 5.44 shows the SEM images of 'HE5050' electrodes after heating and relithiation as well as a pristine sample for comparison. From the primary particles in (b)-(d) it is apparent, that the initial formation, thermal treatment and/or the relithiation process caused a roughening of the particle surface. This is most clearly identifiable for particles which are more deeply embedded in the compound. Probably, the still smoothly appearing particles on the top of the electrodes are electrochemically inactive due to a lack of electronic connection to the conductive carbon particles.

5.7.2. SEM imaging of Li anodes

The lithium counter electrodes corresponding to the above investigated cathodes revealed a thick and black 'coating' on the lithium surface after the five post thermal cycles, in particular the samples heated at a charging state of 4.2 V and 4.7 V as shown in Figure 5.45. This finding was unexpected, since the growth of a thick SEI layer and lithium dendrites on the anode surface was only observed for highly cycled lithium anodes before (e.g. for the electrochemically fatigued cell after reaching 300 cycles). The anode samples were extracted from the cell stack inside an argon-filled glovebox and transferred to the SEM within an argon-filled transfer-container. The samples were analyzed as received, without rinsing in DMC.

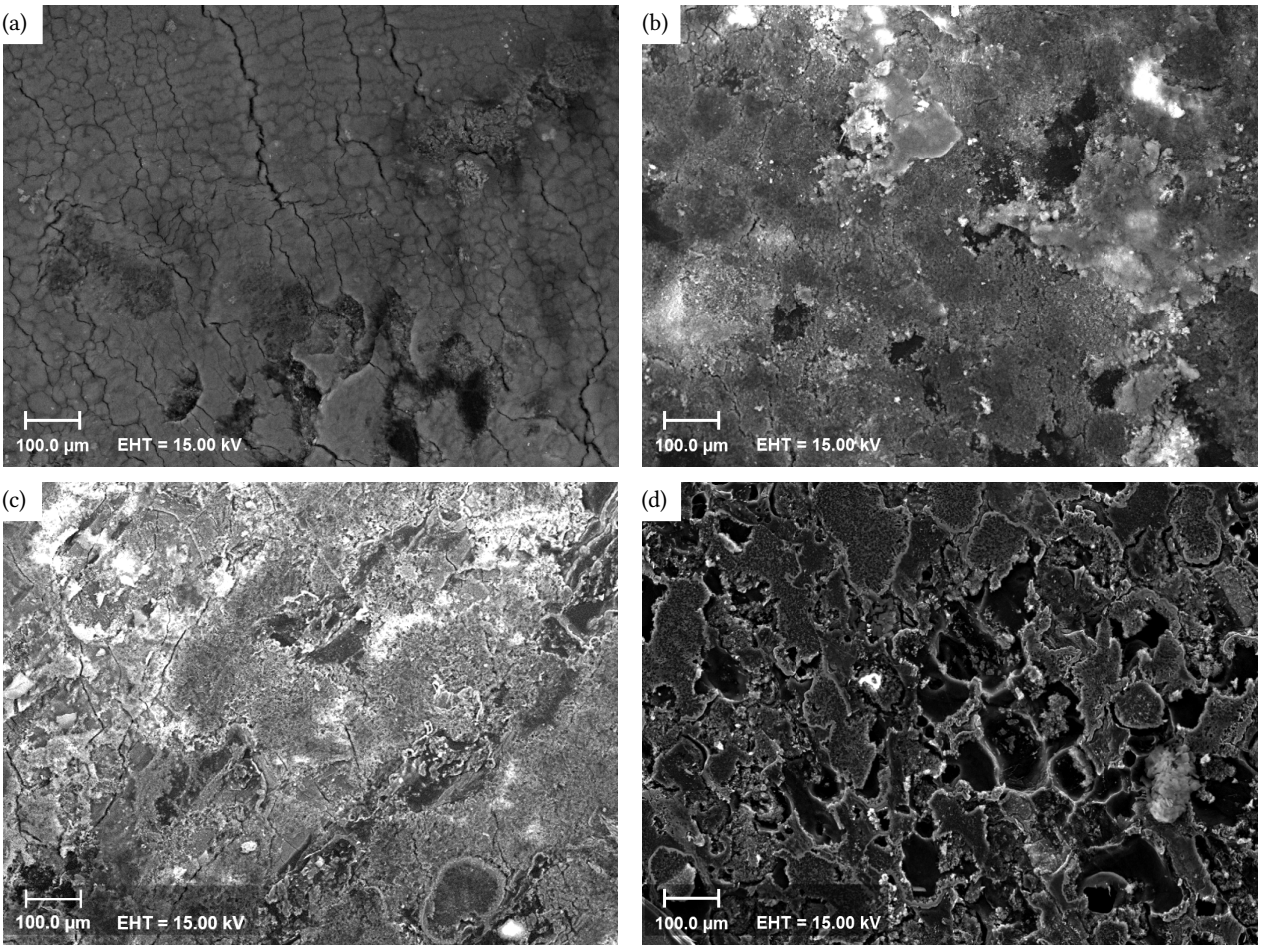

Figure 5.45.: SEM images of lithium anodes after five post thermal cycles against 'HE5050' cathodes, which were thermally treated at a charging state of 2.0 V (a+b), 4.2 V (c) and 4.7 V (d).

The Li anode cycled against a cathode heated in the discharged state (2.0 V) was rather inhomogeneously covered by the SEI as presented by the two spots: blank (a) and covered (b). The SEM images of Li anodes cycled against cathodes heated in a charge state (4.2 V and 4.7 V) show a coverage of the entire lithium anode. Additionally, the SEM image labeled (d) reveals several notches, which were probably induced by the pull off of the well-sticking separator (ingrown lithium dendrites).

5.7.3. SEM-EDX analysis of Li anodes

In order to derive the elemental distribution of the deposits on the lithium anodes, energy-dispersive X-ray spectroscopy (EDX) measurements were carried out. The excited surface directly corresponds to the area shown in the respective SEM image (Figure 5.45). The results of the EDX analysis are summarized in Table 5.5.

Table 5.5.: Mass-related elemental distributions (% w/w) obtained from EDX measurements of lithium anodes after five post thermal cycles against 'HE5050' cathodes, which were thermally treated at a charging state of 2.0 V, 4.2 V and 4.7 V.

Sample	C	O	F	P	Mn	Co	Ni
2.0 V, spot a	8(1)	10(1)	78(8)	4(1)	0.2(1)	-	-
2.0 V, spot b	8(1)	17(2)	71(7)	4(1)	0.3(1)	-	-
4.2 V	16(2)	31(3)	45(5)	2(1)	4.8(2)	0.3(1)	0.4(1)
4.7 V	18(2)	36(4)	36(4)	1(1)	7.2(2)	0.6(1)	0.6(1)

The blank surface (spot a) and the deposit (spot b) of the '2.0 V' lithium anode sample are mainly composed of residues (F, P) from the PF_6^- electrolyte anion as well as residues and/or decomposition products (C, O) from the electrolyte solvent (EC/DMC). Furthermore, a small amount (<1% w/w) of manganese was detected on both spots. The elemental distribution of the '4.2 V' and the '4.7 V' sample clearly shows a trend towards a higher content of residues and/or decomposition products (C, O) originating from the electrolyte solvent at the expense of the PF_6^- electrolyte content (F, P) and most interestingly a profound rise of the transition metal content. The '4.2 V' sample shows a manganese content of about 5% (w/w), the '4.7 V' sample even 7% (w/w). Additionally, both samples reveal traces of nickel and cobalt (<1% w/w). This observation clearly points out the dissolution of transition metals from the cathode surface in the electrolyte and the redeposition

within the SEI of the lithium anode. Since the disproportionation reaction of Mn^{3+} into Mn^{2+}/Mn^{4+} and the subsequent dissolution of Mn^{2+} in the electrolyte is a known degradation mechanism for LNMO and LMO spinels [96], these findings further support the redox activity of manganese in the samples after heating. Apparently, the amount of manganese on the anode surface directly correlates with the refined spinel content and the redox activity of the spinel phase, respectively. Moreover, the existence of Mn^{2+} in the electrolyte may also explain the rather thick coverage of the lithium anode with a SEI. Recent evidence suggests that the growth of the SEI is significantly catalyzed by a manganese contaminated SEI [97, 98], which is well in agreement with aforementioned observations.

5.8. X-ray absorption spectroscopy

In order to study the element-specific changes of oxidation states and the local structural environments of the transition metal ions after the formation cycle as well as after the thermal treatment experiments, hard X-ray absorption spectroscopy (XAS) was performed at the Mn, Co, and Ni K-edges. Here, the oxidation states of the transition metal ions were examined by the evaluation of the normalized near-edge structure (XANES) and the local structure was investigated by the analysis of the extended X-ray absorption fine structure (EXAFS), respectively. This was complemented by soft XAS measurements at the oxygen K-edge.

5.8.1. Transition metal K-edge XANES

Introduction: Figure 5.46 shows the normalized near-edge structure (XANES) spectra of the Mn, Co and Ni K-edge belonging to the 'HE5050' material in pristine state and charged to 2.0 V, 4.2 V and 4.7 V after having completed the initial formation cycle. The transition metal K-edge can be divided into three different edge features: the pre-edge, region 'A' and the white line 'B'. The weak pre-edge is associated with electric quadrupole and formally forbidden electric dipole transitions from TM 1*s* to TM 3*d* orbitals for transition metal ions located in an ideal octahedral environment. With increasing distortion of the octahedral framework or the occupation of tetrahedral sites (both

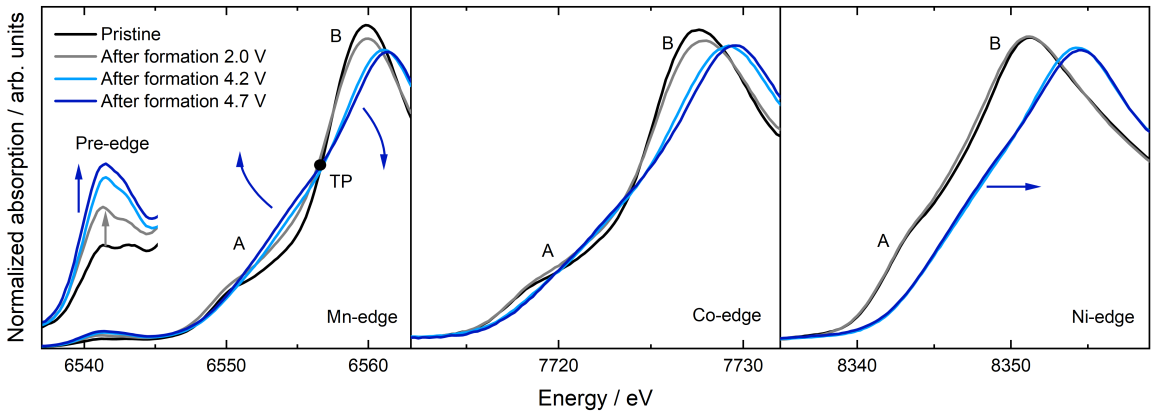

Figure 5.46.: XANES spectra at Mn, Co and Ni K-edges of the pristine 'HE5050' as well as of samples after formation charged to 2.0 V, 4.2 V and 4.7 V. The pre-edge of the manganese K-edge is magnified in the inset. Labels: pre-edge – TM 1*s*-3*d* electron transition, 'A' – TM 1*s*-4*p* electron transition combined with a ligand-to-metal charge transfer (shake-down), 'B' – TM 1*s*-4*p* electron transition, 'TP' – turning point.

leading to a 3d-4p orbital mixing), the electric dipole transition gets more and more allowed and the pre-edge gains in intensity [99, 100]. Due to the rhombohedral distortion of the ccp oxygen sublattice ($R\bar{3}m$) the intensity of the pre-edges are already elevated in the initial state in contrast, for example, to an undistorted cubic unit cell. Since the transition probability strongly depends on the amount of unoccupied 3d orbitals the pre-edge peak intensity changes as a function of the number of 3d electrons with min/max values at d^{10} and d^0, respectively [100]. Region 'A' represents the TM 1s to 4p electron transition combined with a ligand-to-metal charge transfer (shake-down) process and the white line 'B' the direct TM 1s to 4p transition [99, 101].

An oxidation of a TM ion accompanied by a loss of 3d electrons is generally observable by a shift of the edge towards higher energies. This is because the 1s core electrons feel a stronger attraction of the now higher effective nuclear charge relative to the weakly bound and screened valence levels, which leads to an increase of the transition energies. At this point it should be mentioned, that the K-edge (1s-4p transitions) delivers an indirect feedback about the oxidation state of the investigated TM, whereas the L-edge (soft XAS) directly monitors the number of TM 3d electrons by probing the 2p to 3d transitions. Nevertheless, the metal K-edge spectroscopy delivers additional in-depth information about modifications of the local structure and thus was preferred in this study.

Electrochemical formation: By comparing the spectra of 'HE5050' in pristine state (black line) and discharged after formation (grey line) shown in Figure 5.46, it can be concluded that formation induces no considerable shifts of the edge energies. This observation suggests similar oxidation states for all transition metal ions in both states. However, the increase of the Mn pre-edge intensity (highlighted by the grey arrow) indicates an increased distortion of the octahedral symmetry and/or a potential migration of Mn ions into tetrahedral sites. A gain in pre-edge intensity by further oxidation of Mn beyond +IV and thus a decrease of the amount of 3d electrons can be excluded at this point, which was verified by Mn L-edge XAS measurements [63, 77]. These findings support the clear trend towards a decreased order on a local atomic scale in the samples after formation as already exemplified before by the detailed analysis of the ^{7}Li NMR data.

The charging of an electrode after formation to 4.2 V and 4.7 V leads to an obvious shift of the Ni K-edge towards higher energies and thus to an oxidation from +II to +IV [63, 99]. In contrast, no clear shift of the manganese edge as a whole is observed for higher charging states, but instead an alteration of the edge's shape. In fact, this modification can be described as a kind of torsion around the turning point 'TP' as emphasized in the plot. Oishi et al. demonstrated [63], that the torsion of the Mn edge is not linked to the increase of the oxidation state by comparing the results

from Mn K- and L-edge ($2p$–$3d$ transition). Instead, these observations in the Mn K-edge are mainly attributed to variations of the local environment of Mn during de-/lithiation. The significant rise of the pre-edge intensity with increasing charging state suggests a highly distorted Mn-O_6 octahedron and/or the partial migration of Mn ions into tetrahedral sites. The spectra belonging to the Co K-edge do not show a shift of the entire edge after charging to 4.2 V and 4.7 V. This observation suggests a modification of the local environment in combination with or even without a change of the oxidation state [99]. An increase of the oxidation state cannot be verified at this point.

Heating of a discharged sample: As can be seen from Figure 5.47, the thermal treatment (300 °C, 1 h) of a discharged 'HE5050' sample (2.0 V), which completed the initial formation cycle, leads to no considerable changes in the TM K-edge energies and edge shapes (compare blue dashed with orange solid line). However, the decline of the Mn pre-edge intensity (highlighted by the orange arrow) suggests the partial recovery of the initial pristine octahedral symmetry and probably the restoration of the Li/TM-TM_6 honeycomb ordering within the TM layers. After the five post thermal cycles (relithiation) the pre-edge intensity is increased again.

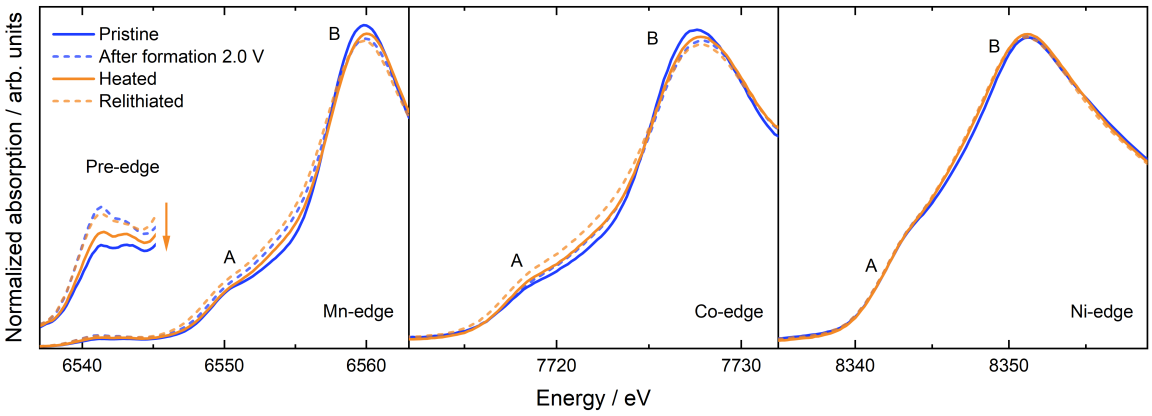

Figure 5.47.: XANES spectra at Mn, Co and Ni K-edges corresponding to the thermal treatment experiments (300 °C, 1 h) of discharged (2.0 V) 'HE5050' cathode samples. The pre-edge of the manganese K-edge is magnified in the inset. Labels: pre-edge – TM $1s$-$3d$ electron transition, 'A' – TM $1s$-$4p$ electron transition combined with a ligand-to-metal charge transfer (shake-down), 'B' – TM $1s$-$4p$ electron transition.

Heating of a charged sample: The experiment was repeated with a charged sample (4.7 V), which completed the initial formation cycle, as presented in Figure 5.48. After the heating step (compare blue dashed with red solid line), the Ni K-edge shifts back to the position it had for the pristine state indicating a reduction of the Ni ions from +IV to +II. Furthermore, the low-energy

region 'A' of the Co K-edge shows a slight shift to lower energies, whereas the position of the white line 'B' is unaffected. This observation provides no direct evidence for a change of the oxidation state. Nevertheless, a comparison with the spectrum of a Co_3O_4 spinel reference (see Figure 5.49a) suggests the reduction of cobalt to a mixed Co^{2+}/Co^{3+} valence state. The tetrahedral 8*a* sites of the cobalt spinel with space group $Fd\bar{3}m$ are occupied with Co^{2+} ions, the octahedral 16*d* sites with Co^{3+} ions, respectively [102]. The formation of a spinel, where Co is (partially) occupying the tetrahedral sites, was also observed within *in situ* thermal studies of overcharged NCM and NCA cathodes by Nam et al. [103]. As a complementary remark, the occupation of these 8*a* sites with transition metal ions can also be observed in the diffraction pattern, for instance, by the emergence of the 220_s reflection (compare Figure 5.20).

Aside from the decline of the pre-edge intensity, the Mn K-edge shows no changes at all. Overall, these findings correlate well with the determined mass loss of the sample after heating (see Section 5.6.2) and the structural transition from the initial layered to spinel structure (see Section 5.3). The immense release of oxygen during heating ($2O^{2-} \rightarrow O_2 + 4e^-$) leads to the reduction of Ni and Co, whereas the oxidation state and the structural framework of manganese shows a high thermal stability.

The subsequent five post thermal cycles ending with a discharge to 2.0 V (relithiation, compare red and red dashed line) lead to a shift of the manganese K-edge towards lower energies beyond

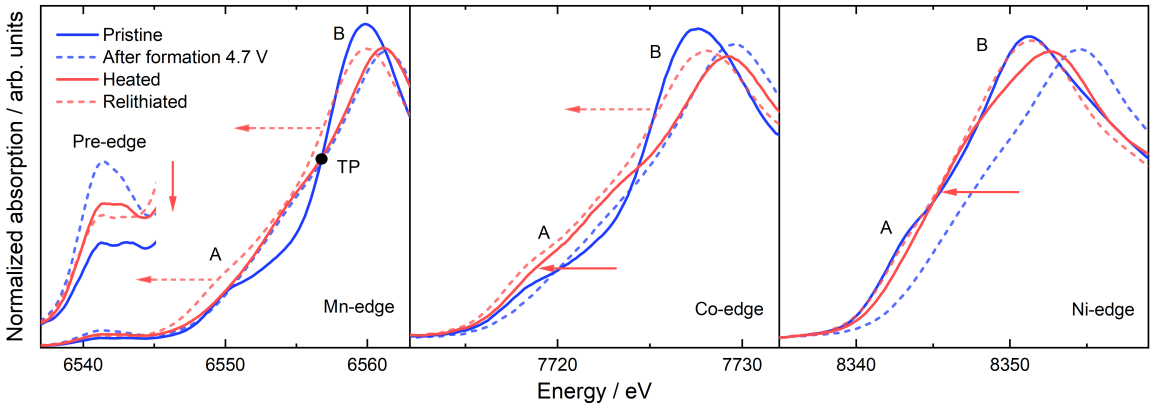

Figure 5.48.: XANES spectra at Mn, Co and Ni K-edges corresponding to the thermal treatment experiments (300 °C, 1 h) of charged (4.7 V) 'HE5050' cathode samples. The pre-edge of the manganese K-edge is magnified in the inset. Labels: pre-edge – TM 1*s*-3*d* electron transition, 'A' – TM 1*s*-4*p* electron transition combined with a ligand-to-metal charge transfer (shake-down), 'B' – TM 1*s*-4*p* electron transition, 'TP' – turning point.

the turning point 'TP', which suggests a reduction of the Mn ions. This outcome accords well with the observed $Mn^{3+/4+}$ redox activity around 3 V in the corresponding dQ/dV plot (see Figure 5.18) of the five post thermal cycles. As already mentioned in the introduction part of this section, the slight decrease of the pre-edge intensity can be explained either by the reduction of lattice distortions as well as a lower transition probability due to a reduction of Mn (less empty 3*d* orbitals). Furthermore, the Co K-edge as a whole moved towards lower absorption energies, whereas for the Ni K-edge only a shift of the white line 'B' can be observed. To sum up, the charge compensation for the lithiation (discharge) of a sample thermally treated in the charged state (4.7 V) is conducted by the reduction of manganese and cobalt, since nickel has already been reduced during heating. This hypothesis will be further supported later on by soft XAS oxygen K-edge measurements (see Section 5.8.3)

Heating of a cycled sample: The extended electrochemical cycling (300 cycles) of a 'HE5050' cathode led to a twist of the Mn K-edge (Figure 5.49b) around 'TP' similar as in the spectrum of the charged sample. Furthermore, the intensity of the pre-edge is significantly increased. These findings indicate a highly distorted Mn environment and/or the occupancy of tetrahedral sites. However the there is no clear indication for the reduction of manganese identifiable in the spectrum. After heating (300 °C, 1 h), the pre-edge intensity decreases as highlighted by the green arrow, which emphasizes a relaxation of lattice distortions. These findings are well in accordance with the corresponding diffraction data. Here, weak $C2/m$ superstructure reflections reappeared as well as the refined lattice strain and the c_h anisotropy decreased noteworthy after heating (see Figure 5.36). Furthermore, the edge twists slightly towards the initial pristine position. However, the edge features are still far away from the pristine state suggesting a less pronounced recovery towards the pristine state in comparison to the discharged sample (2.0 V), which was directly heated after formation.

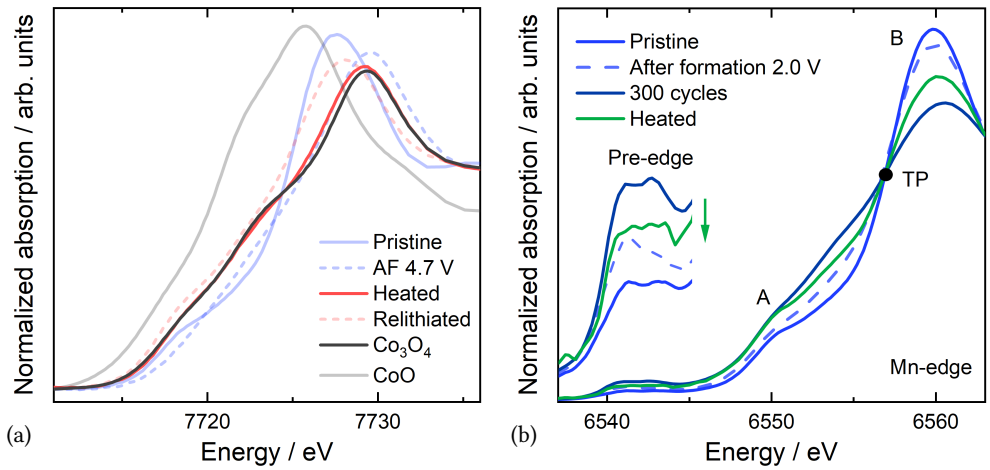

Figure 5.49.: XANES spectrum of the Co K-edge (a) showing a comparison of the heated Li- and Mn-rich sample with a CoO and a Co_3O_4 reference. XANES spectrum at the Mn K-edge (b) corresponding to the thermal treatment experiments (300 °C, 1 h) of electromagnetically fatigued (300 cycles) 'HE5050' cathode samples. The pre-edge of the manganese K-edge is magnified in the inset. Labels: pre-edge – TM 1*s*-3*d* electron transition, 'A' – TM 1*s*-4*p* electron transition combined with a ligand-to-metal charge transfer (shake-down), 'B' – TM 1*s*-4*p* electron transition, 'TP' – turning point.

5.8.2. Transition metal K-edge EXAFS

Introduction: For local structure investigations around the transition metal ions, the element-specific radial distribution functions (RDF) were extracted[9] from the extended X-ray absorption fine structure (EXAFS) oscillations and plotted in Figure 5.50. The strong first and second amplitudes correlate to the single scattering paths of the observed metal with the closest oxygen atoms (M-O) as well as with the second shell (M-M), respectively occupied with metal atoms. In the first instance, the amplitudes are proportional to the coordination number (CN) of the observed atom in the corresponding shell. However, an increased disorder within the material can reduce the amplitude due to a variation in bond distances (destructive interference) within the scattering shell. This variation is commonly described by the Debye-Waller factor σ^2. Higher distances including further single and multiple scattering processes are generally less pronounced, because the EXAFS amplitude decreases with $1/R^2$. However, the intensity of these weak amplitudes provides information regarding the coherent ordering on a mid-range scale. A correlation of the RDF amplitudes with the type and number of bonds is illustrated in Figure F.9 using the Mn RDF as an example.

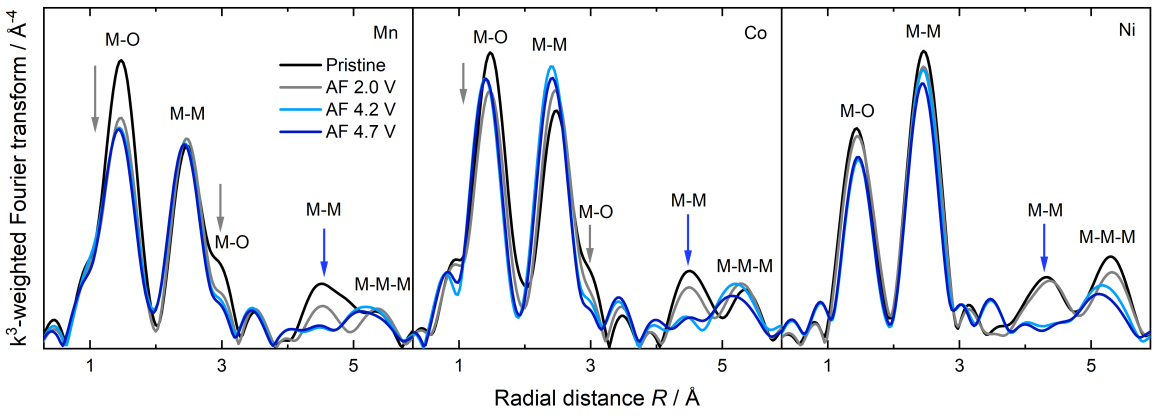

Figure 5.50.: Radial distribution functions (RDF) obtained from the Mn, Co and Ni K-edge EXAFS data of the pristine 'HE5050' as well as of samples after formation charged to 2.0 V, 4.2 V and 4.7 V. Labels: M-O – metal-oxygen single scattering, M-M – metal-metal single scattering, M-M-M – collinear multiple scattering.

[9]It should be noted that the given radial distances are not phase corrected and therefore do not represent the correct crystallographic atomic distances.

Electrochemical formation: As shown in the Mn RDF of the discharged sample (2.0 V), the most apparent change induced by the formation of the Li-rich 'HE5050' is a significant decline of the first and second Mn-O amplitude (compare black and grey line). In contrast, the Ni-O amplitudes do not show a noteworthy change, whereas the Co-O amplitudes show a slight decline. Some possible explanations might be the distortion of the M-O_6 octahedron (higher σ^2), the formation of oxygen vacancies (lower CN) and/or the migration of Mn/Co to a tetrahedral environment (lower CN). The charge process to 4.2 V and 4.7 V leads to the decrease of the M-M amplitudes around 4.5 Å in the RDFs of all three transition metals. This observation suggests a modification of the coherent ordering and was already observed in previous studies [61, 62, 104]. Interestingly, the collinear M-M-M configurations (5.5 Å) are almost unaffected from the delithiation process (slight change for Ni). However, a direct assignment of the changes at 4.5 Å and 5.5 Å to a distinct structural alteration has not been obtained so far.

Heating of a discharge sample: Figure 5.51 shows the RDFs derived from the Mn , Co and Ni EXAFS oscillations corresponding to the thermal treatment experiments of samples discharged to 2.0 V after formation. The most significant change after heating is the increase of the Mn-O amplitudes towards the value it had in the pristine state. Apparently, the Co-O bonds are unaffected by the thermal treatment. These observations suggest a strong contribution of the relaxation of the distorted Mn-O_6 octahedrons to the restoration of the initially well-ordered pristine material and the reoccurrence of the 'plateau' in the first post thermal charge. Additionally, the elimination

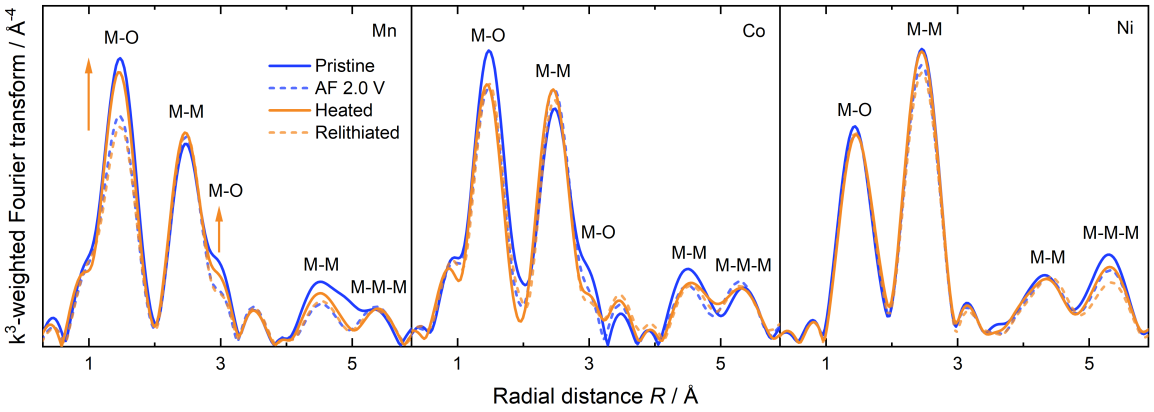

Figure 5.51.: Radial distribution functions (RDF) obtained from the Mn, Co and Ni K-edges EXAFS data corresponding to the thermal treatment experiments (300 °C, 1 h) of discharged samples (2.0 V). Labels: M-O – metal-oxygen single scattering, M-M – metal-metal single scattering, M-M-M – collinear multiple scattering.

of Mn undercoordinations with a CN<6 (oxygen vacancies or migration into tetrahedral sites) can be considered here as well. The subsequent relithiation of the heated electrode leads again to a decrease of the Mn-O amplitudes (compare orange and orange dashed line), which is in accordance with the preceding results, e.g. the disappearance of the $C/2m$ superstructure reflections in the corresponding diffraction pattern (see Figure 5.12).

Heating of a charged sample: It is obvious, that the thermal treatment of a charged sample (Figure 5.52) does not lead to a restoration of the initial state. The M-O amplitudes are declining in the Co and Ni RDFs suggesting a profound distortion of the M-O bonds, oxygen vacancies and/or the migration of TMs in tetrahedral sites. The latter mechanism is indicated in the Co RDF at a radial distance of about 3.3 Å (orange arrow). In order to verify this observation, a Co_3O_4 spinel reference was added to the RDFs as can be seen in Figure 5.53a. Furthermore, a histogram of the bond distances (the type and number of bonds versus the bond distance) is plotted in Figure 5.53b. As can be seen from the histogram, the signal around 3.3 Å fits well with scattering paths originating from the occupation of tetrahedral sites. As a complementary remark, the occupation of tetrahedral sites with Co^{2+} ions was already suggested by the analysis of the corresponding XANES spectrum of the Co K-edge (see Figure 5.49a). A more detailed interpretation of the post thermal RDFs is not straight forward and thus should be further supported by simulations based on corresponding structural models and reference materials. However, this is challenging due to the complex structural features that are not fully identified yet.

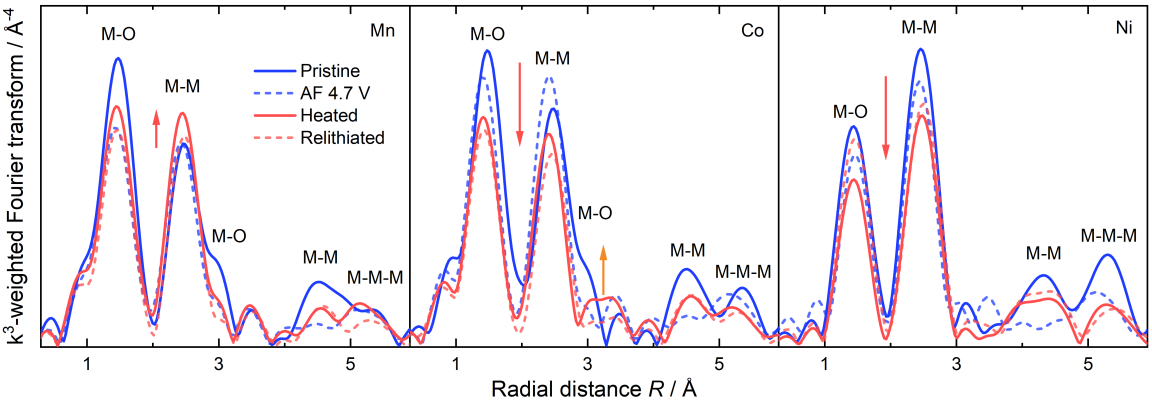

Figure 5.52.: Radial distribution functions (RDF) obtained from the Mn, Co and Ni K-edges EXAFS data corresponding to the thermal treatment experiments (300 °C, 1 h) of charged samples (4.7 V). Labels: M-O – metal-oxygen single scattering, M-M – metal-metal single scattering, M-M-M – collinear multiple scattering.

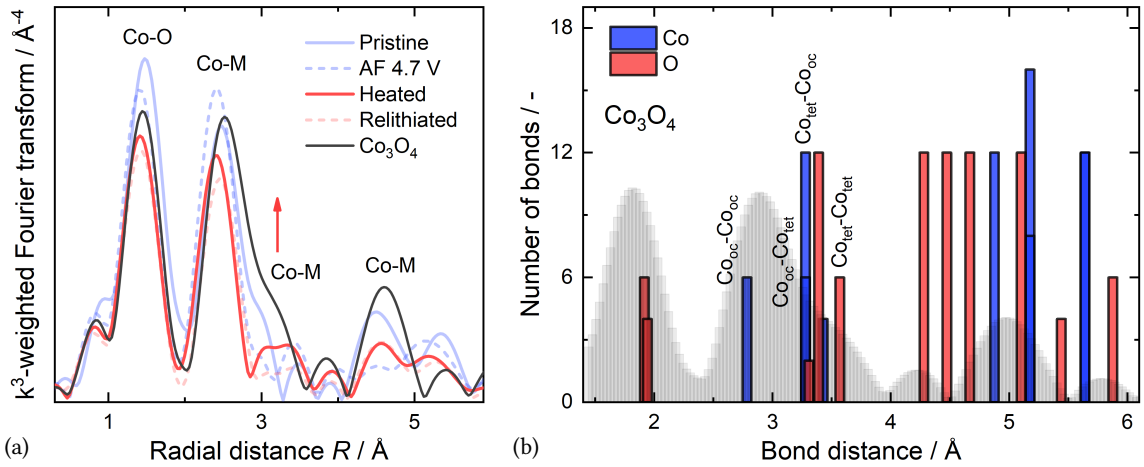

Figure 5.53.: Comparison of the Co RDFs (a) of a charged sample after heating with the Co_3O_4 spinel reference as well as a histogram (b) of the bond distances in the Co_3O_4 spinel, which were extracted from a Crystallographic Information File [105]. The Co RDF of the Co_3O_4 spinel is inserted in the background of (b) and its radial distances were slightly shifted in order to match the histogram. Labels: Co-O – cobalt-oxygen single scattering, Co-M – cobalt-metal single scattering.

5.8.3. Oxygen K-edge

Introduction: Figure 5.54 shows the oxygen K-edge XAS spectra of the 'HE5050' material in pristine state and charged to 2.0 V, 4.2 V and 4.7 V after having completed the formation. The spectra were obtained in the fluorescence yield (FY) mode, which provides information about changes in the bulk (probing depth > 1000 Å) as well as the total electron yield (TEY) mode, which is more surface sensitive (probing depth ≈ 40 Å) [106]. The pre-edge peaks (A*, A, B*, B) below 534 eV belong to the electron transitions from O 1*s* into unoccupied hybridized states of TM 3*d* and O 2*p* orbitals (TM_{3d}–O_{2p}) [107, 108, 109]. A rise of their intensities can be attributed to a higher oxidation state of the transition metals leading to an increase of the number of *d* hole states in the TM 3*d* orbitals that are hybridized with the O 2*p* orbitals as well as to a higher bond covalency of the TM-O bond. The broad peak 'C' beyond 534 eV has been associated with electron transitions from O 1*s* into hybridized TM 4*sp* and O 2*p* orbitals [107, 110]. These transitions are sensitive to changes in the metal-oxygen bond lengths and show an upward energy shift for smaller bond lengths. Since Mn^{4+} ($3d^3$) is the dominant TM ion in the 'HE5050' material and offers seven unoccupied 3*d* electron states (Ni^{2+}: 2, Co^{3+}: 4), the obtained spectra are determined to a large extend by transitions from O 1*s* into Mn_{3d}–O_{2p} orbitals. Consequently, profound alterations in the oxygen K pre-edge can be attributed preferably to the reduction/oxidation of Mn ions and/or significant alteration of the TM-O bond covalency [5].

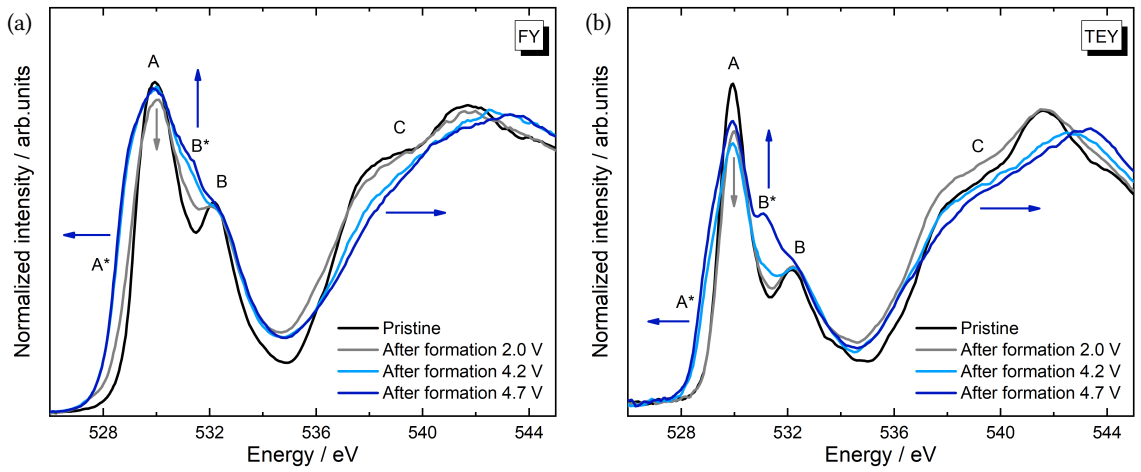

Figure 5.54.: Oxygen K-edge absorption spectra of the pristine 'HE5050' as well as of samples after formation charged to 2.0 V, 4.2 V and 4.7 V, measured in FY (a) and TEY (b) mode. Labels: 'A*', 'A', 'B*', 'B' – electron transitions from O 1*s* to TM 3*d*–O2*p*, 'C' – electron transitions from O 1*s* to TM 4*sp*–O2*p*.

Electrochemical formation: Beginning with the half and fully charged states at 4.2 V and 4.7 V, the spectra measured in FY mode (Figure 5.54a) clearly point to the oxidation of the transition metals during charging. As highlighted by the blue arrows, newly formed electron transitions rise at the position 'A*' as well as at 'B*' and position 'C' shifts to higher values due to a decline of the TM-O bond lengths. Qiao et. al [111] demonstrated for the $LiNi_{0.5}Mn_{1.5}O_4$ spinel, that the evolution of peak 'A*' can be attributed to the oxidation of Ni from +II to +IV generating two additional low-energy transitions. However, soft XAS studies on (partially) delithiated $LiCoO_2$ [112, 113, 114], $LiCo_{0.5}Ni_{0.5}O_2$ [115], $LiCo_{1/3}Ni_{1/3}Mn_{1/3}O_2$ [99] and Li_2MnO_3 [83] cathode materials suggest a more complicated picture consisting of a superposition of many new transitions at 'A*' and 'B*', respectively.

Interestingly, the FY spectra of the 4.2 V as well as the 4.7 V state are rather similar indicating no further modifications in the hybridized TM_{3d}–O_{2p} orbitals beyond 4.2 V. The corresponding spectra obtained in the surface sensitive TEY mode (Figure 5.54b) show additional electron hole states at position 'A' and 'B*' after increasing the charge voltage from 4.2 V to 4.7 V. This indicates a slightly different charge compensation mechanism in the surface and bulk of the electrode material during the charge process. In the discharged state (gray lines), the intensity at position 'A*' and 'B*' drops close to the value of the pristine state. The intensity of peak 'A' is generally decreased after formation (highlighted by the gray arrows), predominantly in the TEY spectra . An explanation for it could be the reduction of manganese, e.g. due to the development of a spinel-like surface layer during formation [6, 116].

Heating of a discharge sample: After the thermal treatment of a discharged sample (Figure 5.55), the pre-edge of the FY spectrum shows slight modifications towards the pristine state (see positions A*, A, dip). The corresponding spectrum of the relithiated sample shows again similar features as the spectrum of the sample after formation. Interestingly, the TEY spectrum reveals a significant drop of the intensity at position 'A' after the relithiation (highlighted by the dashed arrow). As already mentioned before, this drop suggests a reduction of manganese during discharge predominantly at the surface, most probably in a spinel-like surface layer. In reviewing the literature, a considerable similarity with the spectrum of Mn_2O_3 was found [117], which further supports the existence of Mn^{3+}. In summary, these findings are well in agreement with the so far presented results. The bulk properties of initial Li- and Mn-rich material are restored after the thermal treatment of a discharged sample. Nevertheless, as already presented in detail in Section 5.2.5, the irreversible loss of lithium in the first formation cycle leads to a lithium deficiency inhibiting a full restoration

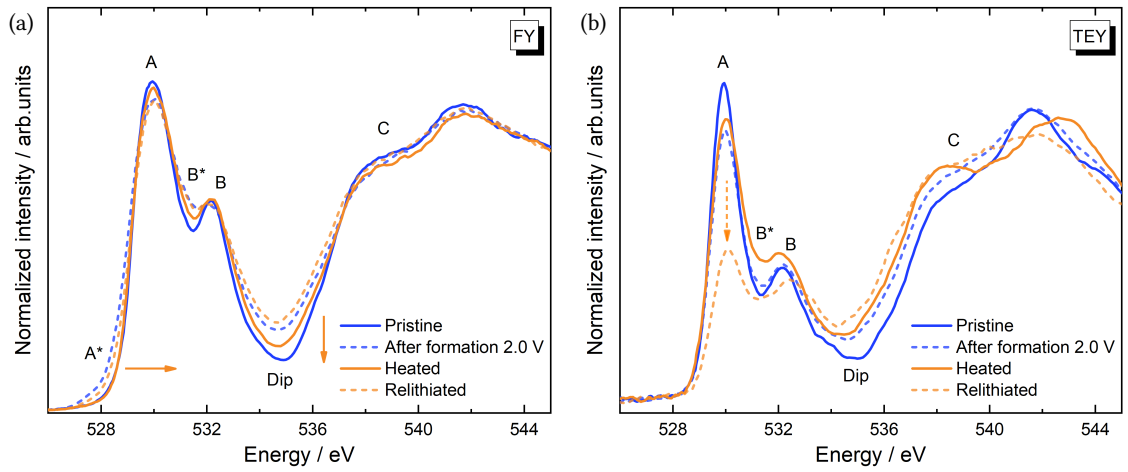

Figure 5.55.: Oxygen K-edge absorption spectra belonging to the thermal treatment experiments of discharged samples (2.0 V), measured in FY (a) and TEY (b) mode. Labels: 'A*', 'A', 'B*', 'B' – electron transitions from O 1*s* to TM 3*d*–O2*p*, 'C' – O 1*s* to TM 4*sp*–O2*p*.

of the pristine state. This deficiency is compensated by the formation of a lithium-poor spinel phase, which has been verified for instance by the emergence of spinel-associated reflections in the corresponding diffraction patterns (see Figure 5.12). Obviously, this process is occurring dominantly at the surface as suggested by the intensity drop in the surface sensitive TEY spectrum of the relithiated sample.

Heating of a charged sample: After the heat treatment of a charged sample (4.7 V), three major changes can be observed in the FY spectrum as shown in Figure 5.56: i) the pre-edge peak 'A*' vanishes, the intensity at position 'A' and 'B*' declines slightly, ii) the TM-O bond lengths increase as indicated by the shift of 'C', and iii) the intensity at the 'dip' significantly increased. These observations can be explained by the reduction of the bulk TM-ions during the heat treatment leading to a decline of free states in the hybridized TM_{3d}–O_{2p} orbitals. Most probably, nickel is reduced predominantly as demonstrated by the shift of the Ni K-edge towards lower energies close the position of the pristine state (see Figure 5.48). The corresponding TEY spectrum reveals similar changes, however the drop of the intensity at 'A' and 'B*' is more pronounced suggesting a reduction of Mn ions within the surface layer. Again, these findings can be well correlated with the preceding results. The reduction of TM ions is induced by the loss of oxygen from the bulk during heating, which is accompanied by the structural rearrangement towards a more spinel-like cation ordering. One unanticipated feature in the spectra is the arise of new electron transitions within the 'dip'. However, the origin of these newly formed transitions remains unclear so far, but

indicates a profound structural alteration during the thermal treatment of a charged sample. The subsequent relithiation (red dashed line) leads to a further decline of the pre-edge intensity, especially at position 'A'. The decline is apparent in both the TEY as well as in the FY spectrum, which points to a reduction of Mn ions located in the surface and in the bulk during discharge. This is in coincidence with the $Mn^{3+/4+}$ redox peaks in the corresponding dQ/dV plots as well as the shift of the Mn K-edge towards lower energies, respectively (see Figures 5.11 and 5.48).

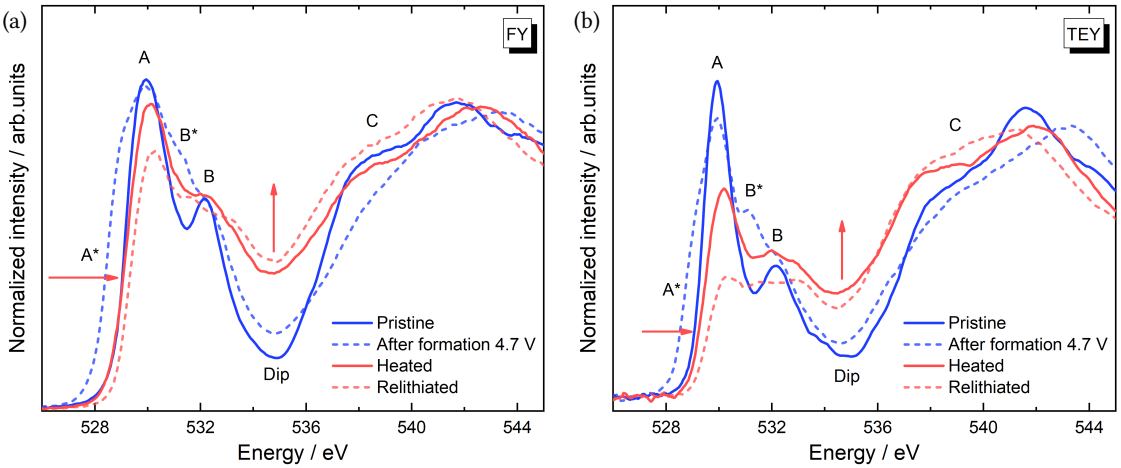

Figure 5.56.: Oxygen K-edge absorption spectra belonging to the thermal treatment experiments of charged samples (4.7 V), measured in FY (a) and TEY (b) mode. Labels: 'A*', 'A', 'B*', 'B' – electron transitions from O 1*s* to TM 3*d*–O2*p*, 'C' – O 1*s* to TM 4*sp*–O2*p*.

6. Discussion

In this chapter, the most important findings of the presented experiments are summarized and merged into a coherent picture regarding the correlation of structure and electrochemical properties of the investigated $Li_{1.2}Ni_{0.15}Co_{0.1}Mn_{0.55}O_2$ layered oxide as a typical representative for Li- and Mn-rich high energy cathode materials. Special focus is put on the modifications of the ordering phenomena either induced electrochemically or thermally as well as on electrochemical features such as the 'plateau' and the voltage fade.

6.1. Formation – order-disorder transition

The first part of the discussion focuses on the processes involved in the initial formation cycle of Li- and Mn-rich NCMs and in particular those with a composition of about $0.5Li_2MnO_3 \cdot 0.5LiTMO_2$ (50:50). Common hypotheses found in literature will be identified and compared with the key findings of this work. Based on this evaluation a more detailed picture will be derived regarding the structure – electrochemical property relationship during the initial charge. First publications that studied the mechanism of the formation, also referred to as 'activation' of Li- and Mn-rich NCMs, suggested an irreversible extraction of lithium and oxygen when the material is charged above 4.4 V on the 'plateau' [72, 73, 74, 75]. This is demonstrated in Equation 6.1 taking pure Li_2MnO_3 for simplification:

$$Li_2MnO_3 \xrightarrow{\text{Charge } >4.4V} 2Li^+ + 2e^- + MnO_2 + 0.5O_2 \uparrow . \tag{6.1}$$

This is followed by a lithiation of the newly formed material during the subsequent discharge step as exemplified by Equation 6.2:

$$MnO_2 + Li^+ + e^- + \xrightarrow{\text{Discharge}} LiMnO_2. \tag{6.2}$$

The proposed mechanism would lead to the following consequences:

i) The migration of transition metal ions to former lithium sites within the TM layer and a release of oxygen from the surface, i.e. a densification of the lattice. This 'densified' lattice is supposed to be isostructural to a non Li/O-rich layered oxide, e.g. $LiCoO_2$, which includes a strict separation of Li and TM ions into pure Li and TM layers. This process is considered to be irreversible and a reconstruction of the pristine ordering can be excluded, in particular the reoccupation of TM sites with Li and the Li/TM-TM_6 honeycomb order within the TM layers.

ii) The formation of $LiMnO_2$ in the subsequent lithiation step after the initial charge and thus to the activation of a $Mn^{3+/4+}$ redox couple for charge compensation, which includes a Jahn-Teller distortion of the Mn-O_6 octahedra and probably the dissolution Mn^{2+} in the electrolyte leading overall to a fast degradation of the cell capacity.

These hypotheses are in strong contrast to the key observations made in this work, in particular to the findings obtained by thermal treatment experiments of discharged samples after formation (2.0 V) as well as electrochemically fatigued samples also in the discharged state (300 cycles):

i) By heating a lithiated sample at 300 °C for 1 h, a (partial) reconstruction of the initial pristine well-ordered structural arrangement was induced. This included a pronounced recovery of the long-range Li/TM-TM_6 honeycomb ordering in the TM layers, as clearly demonstrated by the reappearance of the $C2/m$ superstructure reflections in the corresponding diffraction patterns, and the recovery of the highly ordered local Li environments as suggested by the reappearance of the distinct Li_2MnO_3-like resonances in the $^{6/7}$Li NMR spectra.

ii) The presence of bulk Mn^{3+} after the formation cycle could not be confirmed by the conducted XAS measurements at the Mn K-edge nor at the O K-edge. Similar results were obtained by other groups [63, 76, 77]. Furthermore, a rapid decay of the capacity, due to a manganese +III/+IV redox activity, was not observed during cycling.

In strong contrast to Equations 6.1 and 6.2, the results of this work strongly imply the integrity of the oxygen sublattice to a large extend and the absence of a profound migration of TM ions into former lithium sites within the TM layer (densification) after the formation cycle or even after a high number of cycles. This accords well with recently published studies, which demonstrated that only a small proportion of the formerly proposed amount of oxygen is actually released from the material [5, 6, 69].

The question that now arises is, which processes can be linked with the formation above 4.4 V during first charge instead?

The obtained results of this work suggest the following mechanism: The 4.5 V 'plateau' can be directly associated with a order-disorder transition of the initially well-ordered material. The *ex situ* XRPD and ^{6}Li NMR measurements (see Section 5.1), at defined charging states along the voltage profile of the first cycle, clearly underpins the loss of the Li/TM-TM_6 honeycomb ordering on a long-range as well as on a very-local atomic scale. Until a charging state of 4.4 V the $C2/m$ superstructure reflections (diffraction) and the distinct Li_2MnO_3-like resonances (^{6}Li NMR) are still well-identifiable indicating the integrity of the honeycomb ordering up to this point. After the 'plateau' these features completely vanish and thereupon a highly defective metastable structure is formed which gradually transforms towards a more spinel-type cation arrangement with increasing number of cycles or by moderate heating in a charged state, respectively. As it has clearly been shown, the honeycomb ordering and the therewith-associated spectral features do not reappear after the subsequent discharge nor in the following charge/discharge steps.

Interestingly, in pure Li_2MnO_3 this transformation is almost completed after the first cycle as it was emphasized in Section 5.1.1. The voltage profile of the second cycle belonging to pure Li_2MnO_3 can be directly correlated to a $Mn^{3+/4+}$ redox activity (redox peaks around 3.0 V, 'S_{Mn}') as already suggested by Equations 6.1 and 6.2 shown above. In literature this was confirmed, for instance, by soft XAS measurements at the Mn L-edge and at the O K-edge [83, 118]. It can therefore be concluded that the cation rearrangement processes during cycling of Li- and Mn-rich NCMs can be described as a kind of postponed transformation towards a densified lattice over many charge and discharge cycles. This gradual transformation is manifested in a continuous decrease of the mean charge and discharge voltage, respectively.

The initial 'de'-ordering process during the first charge of $Li_{1.2}Ni_{0.15}Co_{0.1}Mn_{0.55}O_2$ material leads to the emergence of a reversible anionic contribution to the charge compensation at low redox potentials, in this study termed defect-related oxygen contribution 'O_{def}'. Apparently, this redox process replaced the initially occurring 'plateau' and was considered to be irreversible so far. The presented results clearly demonstrate the gradual suppression of this redox process 'O_{def}' after the thermal treatment of lithiated samples (discharged to 2.0 V) with increasing temperature (150 °C - 300 °C). These observations can be linked to the recovery of the initial binding conditions and therefore the restoration of the initial electronic structure and is observable, for instance, by the reappearance of the 'plateau' around 4.5 V in the electrochemical data (see dQ/dV Figure 5.2.5).

The evolution of the observed structural features revealed that the gradual suppression of the redox process 'O_{def}' can be attributed to the transition of the highly defective state towards the well-ordered pristine state. This disordered-ordered transition takes place as a function of temperature in a two-step mechanism (see Section 5.2.5): First, lattice defects are compensated on a very-local scale at temperatures from 150 °C to 250 °C. This is most clearly indicated by the decrease of the refined lattice strain as well as a narrowing of the resonances in the ^{7}Li NMR spectra. The first recovery-step could involve, for instance, the depletion of tetrahedral sites, which are presumably occupied by Li and TM ions after formation [11, 12, 13, 14]. However, due to the loss of Li in the formation cycle a full recovery of the entire material cannot be achieved. For this reason, the second recovery-step is characterized by a phase separation that occurs at a heating temperature of 300 °C. This includes the formation of a pristine-like lithium- and oxygen-rich phase and a lithium- and oxygen-poor spinel phase, respectively. This assumption was confirmed by the post thermal electrochemical and structural characterization, where two newly occurring spinel-related redox peaks ('S_{Mn}' and 'S_{Ni}') were identified in the dQ/dV plot of the post thermal cycles and spinel-related additional reflections emerged in the corresponding diffraction pattern. These reflections are significantly broadened, which originates from a rather fine dispersion of the newly formed spinel domains (refined to about 5 nm) within the layered matrix.

6.2. Spinel formation and oxygen loss

The investigations regarding the thermal treatment of partially delithiated electrodes (charged to 4.2 V and 4.7 V) demonstrated a profound degradation towards a spinel-type cation arrangement associated with the release of oxygen (see Sections 5.3 and 5.4). In the following, the main findings are summarized and, based on that, a suitable mechanism is proposed. Especially from the TM K-edge XAS measurements (see Section 5.8), it is apparent, that the oxidation state of the transition metals reduces during heating towards the pristine configuration (Ni+II, Co+III, Mn+IV). Most probably, the reduction process is also valid for the compensation of the electron holes on the oxygen, which were introduced during charging. The proposed reaction mechanism during heating is demonstrated by Equation 6.3 using the fully charged electrode (4.7 V) as an example:

$$\overset{+1}{\mathrm{Li}}_{0.25}\overset{+4}{\mathrm{Ni}}_{0.15}\overset{+4}{\mathrm{Co}}_{0.1}\overset{+4}{\mathrm{Mn}}_{0.55}\overset{-2}{\mathrm{O}}_{2} \xrightarrow{300\,^{\circ}\mathrm{C}} \overset{+1}{\mathrm{Li}}_{0.25}\overset{+2}{\mathrm{Ni}}_{0.15}\overset{+3}{\mathrm{Co}}_{0.1}\overset{+4}{\mathrm{Mn}}_{0.55}\overset{-2}{\mathrm{O}}_{1.53} + 0.24\overset{0}{\mathrm{O}}_{2}\uparrow, \tag{6.3}$$

where the Li content was derived from the electrochemical data neglecting side reactions, for this and the subsequent equations, respectively. The thereof derived amount of released oxygen fits well to the estimated values being based on the electrode mass loss after heating (see Section 5.6.2). There an oxygen loss of 0.22 or 0.3 O_2 per formula unit were determined by assuming a degassing as CO_2 or O_2, respectively. The thus obtained oxygen loss leads to an O/TM ratio smaller than 2 indicating a full densification towards a LiTMO$_2$-type layered and/or LiTM_2O$_4$-type spinel cation arrangement. This includes a more uniform occupancy of the Li and TM layers with Li and TM ions and therefore a disappearance of the layered character. The thereof derived hypotheses is clearly confirmed by the analysis of the corresponding SRPD patterns. After heating, a spinel phase content of 50(5)% (w/w) was derived from the Rietveld refinement of a sample charged to 4.7 V before. Since Ni and Co are probably already in their +II and +III ground state the first post thermal discharge includes the reduction of manganese, as emphasized by Equation 6.4:

$$\overset{+1}{\mathrm{Li}}_{0.25}\overset{+2}{\mathrm{Ni}}_{0.15}\overset{+3}{\mathrm{Co}}_{0.1}\overset{+4}{\mathrm{Mn}}_{0.55}\overset{-2}{\mathrm{O}}_{1.53} \xrightarrow{\text{Discharge +0.4 Li}} \overset{+1}{\mathrm{Li}}_{0.65}\overset{+2}{\mathrm{Ni}}_{0.15}\overset{+3}{\mathrm{Co}}_{0.1}\overset{+3.3}{\mathrm{Mn}}_{0.55}\overset{-2}{\mathrm{O}}_{1.53}. \tag{6.4}$$

This reduction of manganese leads to an active $Mn^{3+/4+}$ redox couple identifiable at around 3.0 V/2.7 V (ox/red) in the corresponding dQ/dV plot and is rather similar to the low-voltage plateau in LMO- or LNNO-type spinels (compare Figure 5.19). The related dissolution of Mn^{2+} in the electrolyte, the consequent deposition on the anode (proved by SEM-EDX, Section 5.7.2) and the strong capacity fade provided further evidence for the $Mn^{3+/4+}$ redox activity. In the subsequent

delithiation step (charge), first Mn^{3+} is oxidized to Mn^{+4} followed by the high-voltage redox activity of Ni as presented by Equation 6.5:

$$\overset{+1}{Li}_{0.65}\overset{+2}{Ni}_{0.15}\overset{+3}{Co}_{0.1}\overset{+3.3}{Mn}_{0.55}\overset{-2}{O}_{1.53} \xrightarrow{\text{Charge -0.55(0.65)Li}} \overset{+1}{Li}_{0.1(0)}\ \overset{+3(3.7)}{Ni}_{0.15}\overset{+3}{Co}_{0.1}\overset{+4}{Mn}_{0.55}\overset{-2}{O}_{1.53}. \tag{6.5}$$

Since there is still lithium available and not all transition metal ions are fully oxidized, the material can be further reversibly delithiated beyond 4.7 V as illustrated by the values in the round brackets in Equation 6.5. Most probably, this high-voltage activity is originating from the delithiation of tetrahedral sites and the oxidation of Ni rather similar to the LNMO-type spinel. A redox activity of cobalt probably takes place at higher voltages beyond 5.0 V in a spinel-type environment and is therefore presumably not contributing to the charge compensation during de-/lithiation [92].

The variation of the heating temperature (150 °C, 200 °C, 250 °C, 300 °C) clearly underpins the importance of oxygen release for the spinel formation (see Section 5.3.5). Up to 200 °C no significant mass loss was observed for the charged electrode (4.7 V) after heating and the corresponding dQ/dV curves revealed no spinel-type redox contribution to the charge and discharge capacity. However, the mean charge/discharge voltage decreased (voltage fade), which can be ascribed to the very-local rearrangement of cations towards a more cubic configuration. Probably, the migration of a small percentage of TM ions to tetrahedral sites and/or to the Li layers is sufficient in order to induce the voltage fade [14]. From 250 °C on, the spinel-associated redox peaks emerge in the electrochemical data (dQ/dV), and a nano-sized spinel phase appears in the related diffraction patterns, respectively. In addition, a considerable amount of oxygen was released from the electrode (determined by mass loss), which clearly emphasizes the direct link between spinel formation and oxygen loss in Li- and Mn-rich NCM cathode materials.

6.3. Degradation processes in highly cycled cathode samples

Continuous cycling results in unwanted voltage fade and increase of the hysteresis attributed to cation rearrangement, which is evident from the structural investigations of the electrochemically fatigued sample (300 cycles). For example, this is demonstrated by the emergence of a spinel phase and the increase of the refined lattice strain as well as the appearance of new Li-environments in the ^{7}Li NMR spectra. The analysis of the corresponding diffraction data revealed a refined spinel phase content of about 30% (w/w). However, the electrochemical data differs from thermally fatigued samples, which also showed the appearance of a spinel phase in the diffraction patterns, especially after heating in a charged state. Interestingly, spinel-associated redox peaks are not clearly identifiable in the dQ/dV curve of the 300$^{\text{th}}$ cycle (see Figure 5.33), but rather an intensification of the low-voltage redox process 'O_{def}'. The Mn K-edge of the fatigued sample shows no shift of the entire edge and therefore does not support a significant $Mn^{3+/4+}$ redox activity in the material. Overall, this seems to be rather contradictory to the findings in the diffraction data and needs to be further investigated. One possible explanation will be given below.

After heating an electrochemically fatigued sample (300 °C, 1 h), the pristine well-ordered state is partially recovered as exemplified by the reappearance of the $C2/m$ superstructure reflections, the narrowing of the ^{7}Li NMR resonances in combination with the return of the distinct Li_2MnO_3-like resonances as well as the reappearance of the 4.5 V 'plateau' in the first post thermal charge. Furthermore, the defect-associated redox process 'O_{def}' decreases significantly in the post thermal cycles and the high-voltage peaks are reactivated, i.e. the formation of a pronounced voltage fade and hysteresis has been partially reversed. Furthermore, the refined spinel content did not change in range of error after the heat treatment. Interestingly, the spinel-associated redox peaks 'S_{Mn}' and 'S_{Ni}' are now clearly identifiable in the electrochemical data (dQ/dV) of the post thermal cycles. These observations suggest a partial formation of a spinel-type transition metal cation ordering within the 300 charge/discharge cycles. Probably, due to the excess of oxygen in the material as well as the high lattice strain, the formation of a LNMO-like spinel is obviously not fully developed, i.e. a clear structure – electrochemical property correlation is not apparent.

One explanation for this phenomenon might be the formation of nano-twins [17, 18, 47] within the first cycle as well as in the following cycles in order to compensate the resulting lattice strain in highly delithiated states. It has recently been shown that nano-twin boundaries exhibit a cation arrangement that is close to the spinel-type ordering, but are still embedded in the initial oxygen

framework [17]. Perhaps, these nano-twins might lead to a rather similar X-ray diffraction pattern and are misinterpreted. The emergence of spinel-type reflections in the diffraction patterns after a high number of cycles might be due to an increased twin density. After heating, the structure probably separates in a Li/O-rich pristine-like phase and a spinel phase along with the release of oxygen (partial densification) and the reduction of the lattice strain. This 'post thermal' spinel phase is full-featured including the clear appearance of the high-voltage redox peak 'S_{Ni}' and the low-voltage peak 'S_{Mn}', respectively. In order to complement the observed structural changes and to monitor a possible contribution of manganese to the charge compensation during de-/lithiation, for instance, transmission electron microscopy imaging and soft XAS at the Mn L-edge would be appropriate methods.

7. Conclusion and Outlook

The findings of this work clearly emphasize the structural processes involved in the formation cycle as well as the subsequent electrochemical degradation in the investigated Li- and Mn-rich NCM cathode material ($Li_{1.2}Ni_{0.15}Co_{0.1}Mn_{0.55}O_2$) with increasing number of cycles including the disappearance of the 4.5 V 'plateau' and a pronounced voltage fade. It could be shown that the initially well-ordered layered structure and in particular the Li/TM-TM_6 honeycomb ordering within the transition metal layers disappears during first charge and is replaced by a highly defective metastable state. This order-disorder transition was monitored on a long-range as well as on a very-local atomic scale by the combination of complementary characterization methods: synchrotron radiation powder diffraction (evolution of the $C2/m$ honeycomb superstructure, lattice parameters and size/strain), $^{6/7}$Li MAS NMR spectroscopy (local Li-TM_6 honeycomb ordering and detection of newly formed Li environments) and X-ray absorption spectroscopy (evolution of the TM oxidation states and local TM environments). The newly formed highly defective material exhibits a modified electronic structure and in particular an additional low-voltage redox process 'O_{def}' in comparison to non Li-rich NCM cathodes. It could be shown that this redox process can be ascribed to the disappearance of the honeycomb ordering within the TM layers.

The mild thermal treatment at temperatures ranging from 150 °C - 300 °C of these highly defective materials (after formation) induced either the partial recovery of the pristine well-ordered state in discharged samples (lithiated), or a strong degradation towards a spinel-type cation arrangement in charged electrodes (delithiated). In the first case, the electrochemical property – structure relationship was clearly exemplified by the reappearance of the first charge 4.5 V 'plateau', the disappearance of the redox process 'O_{def}' and the partial reversion of the voltage fade. In the second case, the highly defective metastable material was converted to a more thermodynamically stable cubic spinel phase, which included the loss of the layered cation ordering and a densification of the lattice along with the release of oxygen. It could be shown that this structural transformation led to the emergence of LNMO-like spinel redox processes in the corresponding electrochemical data.

These findings contribute to a more coherent picture regarding the decisive processes involved in the initial order-disorder transition as well as the subsequent far-reaching structural changes during cycling. Complementary investigations by using, for instance, transmission electron microscopy and *in situ* methods in combination with a thermally induced modification of the material might be useful for completing this picture regarding the the very-local and the long-range atomic ordering and the thereof related electrochemical properties. Furthermore, a rapid benchmarking procedure via the here demonstrated thermal treatment route might be useful for identifying electrochemically stable material compositions, coatings, dopings or synthesis routes in order to arrest the energy fade during cycling and to pave the way towards the commercialization of high energy Li- and Mn-rich NCM cathode materials.

Bibliography

[1] Michael M. Thackeray, Sun-Ho Kang, Christopher S. Johnson, John T. Vaughey, Roy Benedek, and Stephen A. Hackney. Li_2MnO_3-stabilized $LiMO_2$ (M= Mn, Ni, Co) electrodes for lithium-ion batteries. *Journal of Materials chemistry*, 17(30):3112–3125, 2007.

[2] Gaurav Assat and Jean-Marie Tarascon. Fundamental understanding and practical challenges of anionic redox activity in Li-ion batteries. *Nature Energy*, page 1, 2018.

[3] Jason R. Croy, Mahalingam Balasubramanian, Kevin G. Gallagher, and Anthony K. Burrell. Review of the US department of energy's "deep dive" effort to understand voltage fade in Li-and Mn-rich cathodes. *Accounts of chemical research*, 48(11):2813–2821, 2015.

[4] Fulya Dogan, Jason R. Croy, Mahalingam Balasubramanian, Michael D. Slater, Hakim Iddir, Christopher S. Johnson, John T. Vaughey, and Baris Key. Solid State NMR Studies of Li_2MnO_3 and Li-Rich Cathode Materials: Proton Insertion, Local Structure, and Voltage Fade. *Journal of The Electrochemical Society*, 162(1):A235–A243, 2015.

[5] Kun Luo, Matthew R. Roberts, Rong Hao, Niccoló Guerrini, David M. Pickup, Yi-Sheng Liu, Kristina Edström, Jinghua Guo, Alan V. Chadwick, Laurent C Duda, and Peter G. Bruce. Charge-compensation in 3d-transition-metal-oxide intercalation cathodes through the generation of localized electron holes on oxygen. *Nature chemistry*, 8(7):684, 2016.

[6] Benjamin Strehle, Karin Kleiner, Roland Jung, Frederick Chesneau, Manuel Mendez, Hubert A. Gasteiger, and Michele Piana. The role of oxygen release from Li- and Mn-rich layered oxides during the first cycles investigated by on-line electrochemical mass spectrometry. *Journal of The Electrochemical Society*, 164(2):A400–A406, 2017.

[7] Meng Gu, Ilias Belharouak, Jianming Zheng, Huiming Wu, Jie Xiao, Arda Genc, Khalil Amine, Suntharampillai Thevuthasan, Donald R. Baer, Ji-Guang Zhang, Nigel D. Browning, Jun Liu,

and Chongmin Wang. Formation of the spinel phase in the layered composite cathode used in Li-ion batteries. *ACS nano*, 7(1):760–767, 2012.

[8] Gaurav Assat, Dominique Foix, Charles Delacourt, Antonella Iadecola, Rémi Dedryvère, and Jean-Marie Tarascon. Fundamental interplay between anionic/cationic redox governing the kinetics and thermodynamics of lithium-rich cathodes. *Nature communications*, 8(1):2219, 2017.

[9] Mariyappan Sathiya, Gwenaëlle Rousse, K. Ramesha, CP. Laisa, Hervé Vezin, Moulay Tahar Sougrati, Marie-Liesse Doublet, D. Foix, Danielle Gonbeau, W. Walker, A. S. Prakash, Ben M. Hassine, L. Dupont, , and J-M. Tarascon. Reversible anionic redox chemistry in high-capacity layered-oxide electrodes. *Nature materials*, 12(9):827, 2013.

[10] Hungru Chen and M. Saiful Islam. Lithium extraction mechanism in Li-Rich Li_2MnO_3 involving oxygen hole formation and dimerization. *Chemistry of Materials*, 28(18):6656–6663, 2016.

[11] M. Sathiya, Artem M. Abakumov, D. Foix, G. Rousse, K. Ramesha, M. Saubanère, ML. Doublet, H. Vezin, CP. Laisa, AS. Prakash, d. Gonbeau, G. VanTendeloo, and J-M. Tarascon. Origin of voltage decay in high-capacity layered oxide electrodes. *Nature materials*, 14(2):230, 2015.

[12] Jason R. Croy, Kevin G. Gallagher, Mahalingam Balasubramanian, Zonghai Chen, Yang Ren, Donghan Kim, Sun-Ho Kang, and Michael M. Dees, Dennis W .and Thackeray. Examining hysteresis in composite $x\mathrm{Li_2MnO_3}\cdot(1-x)\mathrm{LiMO_2}$ cathode structures. *The Journal of Physical Chemistry C*, 117(13):6525–6536, 2013.

[13] Debasish Mohanty, Jianlin Li, Daniel P. Abraham, Ashfia Huq, E. Andrew Payzant, David L. Wood III, and Claus Daniel. Unraveling the voltage-fade mechanism in high-energy-density lithium-ion batteries: origin of the tetrahedral cations for spinel conversion. *Chemistry of Materials*, 26(21):6272–6280, 2014.

[14] Fulya Dogan, Brandon R. Long, Jason R. Croy, Kevin G. Gallagher, Hakim Iddir, John T. Russell, Mahalingam Balasubramanian, and Baris Key. Re-entrant lithium local environments and defect driven electrochemistry of Li-and Mn-rich Li-ion battery cathodes. *Journal of the American Chemical Society*, 137(6):2328–2335, 2015.

[15] Baris Key. Solid State NMR Studies of Li-Rich NMC Cathodes: Investigating Structure Change and Its Effect on Voltage Fade Phenomenon. In *Proceedings of the DOE Hydrogen Program and Vehicle Technologies Program Annual Merit Review, Washington, DC*, 2014. URL `https://www.energy.gov/sites/prod/files/2014/07/f17/es187_key_2014_o.pdf`. Last accessed on 18-10-07.

[16] Alastair D. Robertson and Peter G. Bruce. Mechanism of electrochemical activity in Li_2MnO_3. *Chemistry of Materials*, 15(10):1984–1992, 2003.

[17] Lars Riekehr, Jinlong Liu, Björn Schwarz, Florian Sigel, Ingo Kerkamm, Yongyao Xia, and Helmut Ehrenberg. Fatigue in $0.5Li_2MnO_3$:$0.5Li(Ni_{1/3}Co_{1/3}Mn_{1/3})O_2$ positive electrodes for lithium ion batteries. *Journal of Power Sources*, 325:391–403, 2016.

[18] Atsushi Ito, Kaoru Shoda, Yuichi Sato, Masaharu Hatano, Hideaki Horie, and Yasuhiko Ohsawa. Direct observation of the partial formation of a framework structure for Li-rich layered cathode material $Li[Ni_{0.17}Li_{0.2}Co_{0.07}Mn_{0.56}]O_2$ upon the first charge and discharge. *Journal of Power Sources*, 196(10):4785–4790, 2011.

[19] Andrej Singer, M. Zhang, S. Hy, D. Cela, C. Fang, TA. Wynn, B. Qiu, Y. Xia, Z. Liu, A. Ulvestad, N. Hua, J. Wingert, H. Liu, M. Sprung, A. V. Zozulya, E. Maxey, R. Harder, Y. S. Meng, and O. G. Shpyrko. Nucleation of dislocations and their dynamics in layered oxide cathode materials during battery charging. *Nature Energy*, 3:641–647, 2018.

[20] J-M Tarascon and M Armand. Issues and challenges facing rechargeable lithium batteries. *Nature*, 414(6861):359, 2001.

[21] Doron Aurbach, Ella Zinigrad, Yaron Cohen, and Hanan Teller. A short review of failure mechanisms of lithium metal and lithiated graphite anodes in liquid electrolyte solutions. *Solid state ionics*, 148(3-4):405–416, 2002.

[22] John B. Goodenough and Kyu-Sung Park. The Li-ion rechargeable battery: a perspective. *Journal of the American Chemical Society*, 135(4):1167–1176, 2013.

[23] Dominique Guyomard and Jean-Marie Tarascon. Rocking-chair or lithium-ion rechargeable lithium batteries. *Advanced materials*, 6(5):408–412, 1994.

[24] Jürgen Janek and Wolfgang G Zeier. A solid future for battery development. *Nature Energy*, 1:16141, 2016.

[25] Xiuxia Zuo, Jin Zhu, Peter Müller-Buschbaum, and Ya-Jun Cheng. Silicon based lithium-ion battery anodes: A chronicle perspective review. *Nano Energy*, 31:113–143, 2017.

[26] WWU/MEET. Ragone-Plot verschiedener Kathodenmaterialien für Lithium-Ionen Batterien, 2016. URL `http:http://forschung-energiespeicher.info/projektschau/gesamtliste/projekt-einzelansicht/95/Neue_Materialien_fuer_Lithium_Ionen_Batterien/`. Last accessed on 18-10-07.

[27] Arumugam Manthiram and Theivanayagam Muraliganth. Lithium Intercalation Cathode Materials for Lithium-Ion Batteries. *Handbook of Battery Materials*, pages 341–375, 2011.

[28] Stanley M. Whittingham. Lithium batteries and cathode materials. *Chemical reviews*, 104 (10):4271–4302, 2004.

[29] Alpesh Khushalchand Shukla, Quentin M. Ramasse, Colin Ophus, Hugues Duncan, Fredrik Hage, and Guoying Chen. Unravelling structural ambiguities in lithium-and manganese-rich transition metal oxides. *Nature communications*, 6:8711, 2015.

[30] Karalee A. Jarvis, Zengqiang Deng, Lawrence F. Allard, Arumugam Manthiram, and Paulo J. Ferreira. Atomic structure of a lithium-rich layered oxide material for lithium-ion batteries: evidence of a solid solution. *Chemistry of materials*, 23(16):3614–3621, 2011.

[31] Claude Delmas, Claude Fouassier, and Paul Hagenmuller. Structural classification and properties of the layered oxides. *Physica B+ c*, 99(1-4):81–85, 1980.

[32] Tsutomu Ohzuku and Atsushi Ueda. Solid-state redox reactions of $licoo_2$ (r3m) for 4 volt secondary lithium cells. *Journal of The Electrochemical Society*, 141(11):2972–2977, 1994.

[33] Koichi Momma and Fujio Izumi. VESTA 3 for three-dimensional visualization of crystal, volumetric and morphology data. *Journal of applied crystallography*, 44(6):1272–1276, 2011.

[34] Pierre Strobel and Bernadette Lambert-Andron. Crystallographic and magnetic structure of Li_2MnO_3. *Journal of Solid State Chemistry*, 75(1):90–98, 1988.

[35] RD. Shannon and C. Prewitt. Effective ionic radii in oxides and fluorides. *Acta Crystallographica Section B: Structural Crystallography and Crystal Chemistry*, 25(5):925–946, 1969.

[36] Adrien Boulineau, Laurence Croguennec, Claude Delmas, and François Weill. Reinvestigation of Li_2MnO_3 structure: electron diffraction and high resolution TEM. *Chemistry of Materials*, 21(18):4216–4222, 2009.

[37] Julien Bréger, Meng Jiang, Nicolas Dupré, Ying S. Meng, Yang Shao-Horn, Gerbrand Ceder, and Clare P. Grey. High-resolution X-ray diffraction, DIFFaX, NMR and first principles study of disorder in the Li_2MnO_3–$Li[Ni_{1/2}Mn_{1/2}]O_2$ solid solution. *Journal of Solid State Chemistry*, 178(9):2575–2585, 2005.

[38] Adrien Boulineau, Laurence Croguennec, Claude Delmas, and François Weill. Structure of Li_2MnO_3 with different degrees of defects. *Solid State Ionics*, 180(40):1652–1659, 2010.

[39] Toshiyuki Matsunaga, Hideyuki Komatsu, Keiji Shimoda, Taketoshi Minato, Masao Yonemura, Takashi Kamiyama, Shunsuke Kobayashi, Takeharu Kato, Tsukasa Hirayama, Yuichi Ikuhara, et al. Dependence of Structural Defects in Li_2MnO_3 on Synthesis Temperature. *Chemistry of Materials*, 28(12):4143–4150, 2016.

[40] Denis Y.W. Yu, Katsunori Yanagida, Yoshio Kato, and Hiroshi Nakamura. Electrochemical activities in Li_2MnO_3. *Journal of The Electrochemical Society*, 156(6):A417–A424, 2009.

[41] Keiji Shimoda, Masatsugu Oishi, Toshiyuki Matsunaga, Miwa Murakami, Keisuke Yamanaka, Hajime Arai, Yoshio Ukyo, Yoshiharu Uchimoto, Toshiaki Ohta, Eiichiro Matsubara, and Zempachi Ogumi. Direct observation of layered-to-spinel phase transformation in Li_2MnO_3 and the spinel structure stabilised after the activation process. *Journal of Materials Chemistry A*, 5(14):6695–6707, 2017.

[42] CS. Johnson, JS. Kim, C. Lefief, N. Li, JT. Vaughey, and MM. Thackeray. The significance of the Li_2MnO_3 component in 'composite' $x Li_2MnO_3 \cdot (1\text{-}x) LiMn_{0.5}Ni_{0.5}O_2$ electrodes. *Electrochemistry Communications*, 6(10):1085–1091, 2004.

[43] Hakim Iddir and Roy Benedek. First-principles analysis of phase stability in layered–layered composite cathodes for lithium-ion batteries. *Chemistry of Materials*, 26(7):2407–2413, 2014.

[44] Lars Riekehr, Jinlong Liu, Björn Schwarz, Florian Sigel, Ingo Kerkamm, Yongyao Xia, and Helmut Ehrenberg. Effect of pristine nanostructure on first cycle electrochemical characteristics of lithium-rich lithium–nickel–cobalt–manganese-oxide cathode ceramics for lithium ion batteries. *Journal of Power Sources*, 306:135–147, 2016.

[45] Anton Buzlukov, Jean-Marie Mouesca, Lucienne Buannic, Sabine Hediger, Loïc Simonin, Emmanuel Canevet, Jean-Francois Colin, Thibaut Gutel, and Michel Bardet. Li-Rich Mn/Ni Layered Oxide as Electrode Material for Lithium Batteries: A ^{7}Li MAS NMR Study Revealing Segregation into (Nanoscale) Domains with Highly Different Electrochemical Behaviors. *The Journal of Physical Chemistry C*, 120(34):19049–19063, 2016.

[46] MM. Thackeray, S-H. Kang, CS. Johnson, JT. Vaughey, and SA. Hackney. Comments on the structural complexity of lithium-rich $Li_{1+x}M_{1-x}O_2$ electrodes (M= Mn, Ni, Co) for lithium batteries. *Electrochemistry Communications*, 8(9):1531–1538, 2006.

[47] Lars Riekehr. Degradation von Li-reichen $x$$Li_2MnO_3$:(1-$x$)$Li(Ni_{1/3}Co_{1/3}Mn_{1/3})O_2$ Nanokompositen als Aktivmaterial für Lithium-Ionen Batterien. PhD thesis, Technische Universität Darmstadt, 2016.

[48] Kwang Soo Yoo, Nam Woong Cho, and Yong-Joo Oh. Structural and electrical characterization of $Li(Mn_{1-\delta}Ti_{\delta})_2O_4$ electrode materials. *Solid state ionics*, 113:43–49, 1998.

[49] MM. Thackeray, MF. Mansuetto, and JB. Bates. Structural stability of $LiMn_2O_4$ electrodes for lithium batteries. *Journal of power sources*, 68(1):153–158, 1997.

[50] MM. Thackeray, WIF. David, PG. Bruce, and JB. Goodenough. Lithium insertion into manganese spinels. *Materials Research Bulletin*, 18(4):461–472, 1983.

[51] SH. Park, S-W. Oh, SH. Kang, I. Belharouak, K. Amine, and Y-K. Sun. Comparative study of different crystallographic structure of $LiNi_{0.5}Mn_{1.5}O_{4-\delta}$ cathodes with wide operation voltage (2.0–5.0 V). *Electrochimica Acta*, 52(25):7226–7230, 2007.

[52] Qingliu Wu, Yuzi Liu, Christopher S. Johnson, Yangxing Li, Dennis W. Dees, and Wenquan Lu. Insight into the structural evolution of a high-voltage spinel for lithium-ion batteries. *Chemistry of Materials*, 26(16):4750–4756, 2014.

[53] Eun-Sung Lee, Kyung-Wan Nam, Enyuan Hu, and Arumugam Manthiram. Influence of cation ordering and lattice distortion on the charge–discharge behavior of $LiNi_{0.5}Mn_{1.5}O_4$ spinel between 5.0 and 2.0 V. *Chemistry of Materials*, 24(18):3610–3620, 2012.

[54] Ming Xu, Zhaoyong Chen, Lingjun Li, Huali Zhu, Qunfang Zhao, Lian Xu, Nanfa Peng, and Li Gong. Highly crystalline alumina surface coating from hydrolysis of aluminum isopropoxide on lithium-rich layered oxide. *Journal of Power Sources*, 281:444–454, 2015.

[55] Ann-Christin Dippel, Hanns-Peter Liermann, Jan Torben Delitz, Peter Walter, Horst Schulte-Schrepping, Oliver H. Seeck, and Hermann Franz. Beamline P02.1 at PETRA III for high-resolution and high-energy powder diffraction. *Journal of synchrotron radiation*, 22(3): 675–687, 2015.

[56] AP. Hammersley, SO. Svensson, M. Hanfland, AN. Fitch, and D. Hausermann. Two-dimensional detector software: from real detector to idealised image or two-theta scan. *International Journal of High Pressure Research*, 14(4-6):235–248, 1996.

[57] Juan Rodríguez-Carvajal. Recent advances in magnetic structure determination by neutron powder diffraction. *Physica B: Condensed Matter*, 192(1-2):55–69, 1993.

[58] J-F. Bérar and PE. Lelann. ESD's and estimated probable error obtained in Rietveld refinements with local correlations. *Journal of applied crystallography*, 24(1):1–5, 1991.

[59] Clare P. Grey and Young Joo Lee. Lithium MAS NMR studies of cathode materials for lithium-ion batteries. *Solid State Sciences*, 5(6):883–894, 2003.

[60] Bruce Ravel and Mathena Newville. ATHENA, ARTEMIS, HEPHAESTUS: data analysis for X-ray absorption spectroscopy using IFEFFIT. *Journal of synchrotron radiation*, 12(4): 537–541, 2005.

[61] Xiqian Yu, Yingchun Lyu, Lin Gu, Huiming Wu, Seong-Min Bak, Yongning Zhou, Khalil Amine, Steven N. Ehrlich, Hong Li, Kyung-Wan Nam, and Xiao-Qing Yang. Understanding the Rate Capability of High-Energy-Density Li-Rich Layered $Li_{1.2}Ni_{0.15}Co_{0.1}Mn_{0.55}O_2$ Cathode Materials. *Advanced Energy Materials*, 4(5):1300950, 2014.

[62] Atsushi Ito, Yuichi Sato, Takashi Sanada, Masaharu Hatano, Hideaki Horie, and Yasuhiko Ohsawa. In situ X-ray absorption spectroscopic study of Li-rich layered cathode material $Li[Ni_{0.17}Li_{0.2}Co_{0.07}Mn_{0.56}]O_2$. *Journal of Power Sources*, 196(16):6828–6834, 2011.

[63] Masatsugu Oishi, Takahiro Fujimoto, Yu Takanashi, Yuki Orikasa, Atsushi Kawamura, Toshiaki Ina, Hisao Yamashige, Daiko Takamatsu, Kenji Sato, Haruno Murayama, Hajime Tanida, Hajime Arai, Hideshi Ishii, Chihiro Yogi, Iwao Watanabe, Toshiaki Ohta, Atsushi Mineshige, Yoshiharu Uchimoto, and Zempachi Ogumi. Charge compensation mechanisms in $Li_{1.16}Ni_{0.15}Co_{0.19}Mn_{0.50}O_2$ positive electrode material for Li-ion batteries analyzed by a

combination of hard and soft X-ray absorption near edge structure. *Journal of Power Sources*, 222:45–51, 2013.

[64] Xianhui Zhang, Zhenlian Chen, Björn Schwarz, Florian Sigel, Helmut Ehrenberg, Ke An, Zhifeng Zhang, Qinggang Zhang, Yantu Li, and Jun Li. Kinetic characteristics up to 4.8 V of layered $LiNi_{1/3}Co_{1/3}Mn_{1/3}O_2$ cathode materials for high voltage lithium-ion batteries. *Electrochimica Acta*, 227:152–161, 2017.

[65] Vilas G. Pol, Yan Li, Fulya Dogan, Ethan Secor, Michael M. Thackeray, and Daniel P. Abraham. Pulsed sonication for alumina coatings on high-capacity oxides: Performance in lithium-ion cells. *Journal of Power Sources*, 258:46–53, 2014.

[66] Debasish Mohanty, Athena S. Sefat, Jianlin Li, Roberta A. Meisner, Adam J. Rondinone, Andrew E. Payzant, Daniel P. Abraham, David L. Wood III, and Claus Daniel. Correlating cation ordering and voltage fade in a lithium–manganese-rich lithium-ion battery cathode oxide: a joint magnetic susceptibility and TEM study. *Physical Chemistry Chemical Physics*, 15(44):19496–19509, 2013.

[67] R. Hausbrand, G. Cherkashinin, H. Ehrenberg, M. Gröting, K. Albe, C. Hess, and W. Jaegermann. Fundamental degradation mechanisms of layered oxide Li-ion battery cathode materials: Methodology, insights and novel approaches. *Materials Science and Engineering: B*, 192:3–25, 2015.

[68] Robert A. Armstrong, Michael Holzapfel, Petr Novák, Christopher S. Johnson, Sun-Ho Kang, Michael M. Thackeray, and Peter G. Bruce. Demonstrating oxygen loss and associated structural reorganization in the lithium battery cathode $Li[Ni_{0.2}Li_{0.2}Mn_{0.6}]O_2$. *Journal of the American Chemical Society*, 128(26):8694–8698, 2006.

[69] Jing Xu, Meiling Sun, Ruimin Qiao, Sara E. Renfrew, Lu Ma, Tianpin Wu, Sooyeon Hwang, Dennis Nordlund, Dong Su, Khalil Amine, Jun Lu, Bryan D. McCloskey, Wanli Yang, and Wei Tong. Elucidating anionic oxygen activity in lithium-rich layered oxides. *Nature communications*, 9(1):947, 2018.

[70] Enyuan Hu, Xiqian Yu, Ruoqian Lin, Xuanxuan Bi, Jun Lu, Seongmin Bak, Kyung-Wan Nam, Huolin L Xin, Cherno Jaye, Daniel A. Fischer, Kahlil Amine, and Xiao-Qing Yang. Evolution

of redox couples in Li-and Mn-rich cathode materials and mitigation of voltage fade by reducing oxygen release. *Nature Energy*, 3(8):690, 2018.

[71] Seungjun Myeong, Woongrae Cho, Wooyoung Jin, Jaeseong Hwang, Moonsu Yoon, Youngshin Yoo, Gyutae Nam, Haeseong Jang, Jung Gu Han, Nam Soon Choi, Min Gyu Kim, and Jaephil Cho. Understanding voltage decay in lithium-excess layered cathode materials through oxygen-centred structural arrangement. *Nature communications*, 9(1):3285, 2018.

[72] Haijun Yu, Hyunjeong Kim, Yarong Wang, Ping He, Daisuke Asakura, Yumiko Nakamura, and Haoshen Zhou. High-energy 'composite'layered manganese-rich cathode materials via controlling Li_2MnO_3 phase activation for lithium-ion batteries. *Physical Chemistry Chemical Physics*, 14(18):6584–6595, 2012.

[73] Jeom-Soo Kim, Christopher S. Johnson, John T. Vaughey, Michael M. Thackeray, Stephen A. Hackney, Wonsub Yoon, and Clare P. Grey. Electrochemical and Structural Properties of $x$$Li_2M'O_3$(1-$x$)$LiMn_{0.5}Ni_{0.5}O_2$ Electrodes for Lithium Batteries (M' = Ti, Mn, Zr; $0 \leq x \leq 0.3$). *Chemistry of Materials*, 16(10):1996–2006, 2004.

[74] Zhonghua Lu and Jeff R. Dahn. Understanding the anomalous capacity of $Li/Li[Ni_xLi_{(1/3-2x/3)}Mn_{(2/3-x/3)}]O_2$ cells using in situ X-ray diffraction and electrochemical studies. *Journal of The Electrochemical Society*, 149(7):A815–A822, 2002.

[75] Sunny Hy, Felix Felix, John Rick, Wei-Nien Su, and Bing Joe Hwang. Direct In situ observation of Li_2O evolution on Li-Rich high-capacity cathode material, $Li[Ni_xLi_{(1-2x)/3}Mn_{(2-x)/3}]O_2 (0 \leq x \leq 0.5)$. *Journal of the American Chemical Society*, 136(3): 999–1007, 2014.

[76] Shoaib Muhammad, Hyunchul Kim, Yunok Kim, Donghwi Kim, Jay Hyok Song, Jaegu Yoon, Jin-Hwan Park, Sung-Jin Ahn, Sun-Ho Kang, Michael M. Thackeray, et al. Evidence of reversible oxygen participation in anomalously high capacity Li-and Mn-rich cathodes for Li-ion batteries. *Nano Energy*, 21:172–184, 2016.

[77] Masatsugu Oishi, Chihiro Yogi, Iwao Watanabe, Toshiaki Ohta, Yuki Orikasa, Yoshiharu Uchimoto, and Zempachi Ogumi. Direct observation of reversible charge compensation by oxygen ion in Li-rich manganese layered oxide positive electrode material, $Li_{1.16}Ni_{0.15}Co_{0.19}Mn_{0.50}O_2$. *Journal of Power Sources*, 276:89–94, 2015.

[78] Yukinori Koyama, Isao Tanaka, Miki Nagao, and Ryoji Kanno. First-principles study on lithium removal from Li_2MnO_3. *Journal of Power Sources*, 189(1):798–801, 2009.

[79] Kei Kubota, Takayuki Kaneko, Masaaki Hirayama, Masao Yonemura, Yuichiro Imanari, Kenji Nakane, and Ryoji Kanno. Direct synthesis of oxygen-deficient Li_2MnO_{3-x} for high capacity lithium battery electrodes. *Journal of Power Sources*, 216:249–255, 2012.

[80] J. M. Tarascon, E. Wang, F. K. Shokoohi, W. R. McKinnon, and S. Colson. The spinel phase of $LiMn_2O_4$ as a cathode in secondary lithium cells. *Journal of the Electrochemical Society*, 138 (10):2859–2864, 1991.

[81] Pengfei Yan, Liang Xiao, Jianming Zheng, Yungang Zhou, Yang He, Xiaotao Zu, Scott X. Mao, Jie Xiao, Fei Gao, Ji-Guang Zhang, and Chong-Min Wang. Probing the degradation mechanism of Li_2MnO_3 cathode for Li-ion batteries. *Chemistry of Materials*, 27(3):975–982, 2015.

[82] S. Francis Amalraj, Boris Markovsky, Daniel Sharon, Michael Talianker, Ella Zinigrad, Rachel Persky, Ortal Haik, Judith Grinblat, Jordan Lampert, Martin Schulz-Dobrick, Arnd Garsuch, Luba Burlaka, and Doron Aurbach. Study of the electrochemical behavior of the "inactive" Li_2MnO_3. *Electrochimica Acta*, 78:32–39, 2012.

[83] Masatsugu Oishi, Keisuke Yamanaka, Iwao Watanabe, Keiji Shimoda, Toshiyuki Matsunaga, Hajime Arai, Yoshio Ukyo, Yoshiharu Uchimoto, Zempachi Ogumi, and Toshiaki Ohta. Direct observation of reversible oxygen anion redox reaction in Li-rich manganese oxide, Li_2MnO_3, studied by soft X-ray absorption spectroscopy. *Journal of Materials Chemistry A*, 4(23): 9293–9302, 2016.

[84] Naoaki Yabuuchi, Kazuhiro Yoshii, Seung-Taek Myung, Izumi Nakai, and Shinichi Komaba. Detailed studies of a high-capacity electrode material for rechargeable batteries, Li_2MnO_3-$LiCo_{1/3}Ni_{1/3}Mn_{1/3}O_2$. *Journal of the American Chemical Society*, 133(12):4404–4419, 2011.

[85] Clare P. Grey and Nicolas Dupré. NMR studies of cathode materials for lithium-ion rechargeable batteries. *Chemical Reviews*, 104(10):4493–4512, 2004.

[86] Meng Jiang, Baris Key, Ying S. Meng, and Clare P. Grey. Electrochemical and structural study of the layered, "Li-excess" lithium-ion battery electrode material $Li[Li_{1/9}Ni_{1/3}Mn_{5/9}]O_2$. *Chemistry of Materials*, 21(13):2733–2745, 2009.

[87] Young Joo Lee and Clare P. Grey. Determining the lithium local environments in the lithium manganates $LiZn_{0.5}Mn_{1.5}O_4$ and Li_2MnO_3 by analysis of the ^{6}Li MAS NMR spinning sideband manifolds. *The Journal of Physical Chemistry B*, 106(14):3576–3582, 2002.

[88] Seong-Min Bak, Kyung-Wan Nam, Wonyoung Chang, Xiqian Yu, Enyuan Hu, Sooyeon Hwang, Eric A. Stach, Kwang-Bum Kim, Kyung Yoon Chung, and Xiao-Qing Yang. Correlating Structural Changes and Gas Evolution during the Thermal Decomposition of Charged $Li_xNi_{0.8}Co_{0.15}Al_{0.05}O_2$ Cathode Materials. *Chemistry of Materials*, 25(3):337–351, 2013.

[89] Jianming Zheng, Pinghong Xu, Meng Gu, Jie Xiao, Nigel D. Browning, Pengfei Yan, Chongmin Wang, and Ji-Guang Zhang. Structural and chemical evolution of Li-and Mn-rich layered cathode material. *Chemistry of Materials*, 27(4):1381–1390, 2015.

[90] Jordi Cabana, Montserrat Casas-Cabanas, Fredrick O. Omenya, Natasha A. Chernova, Dongli Zeng, M. Stanley Whittingham, and Clare P. Grey. Composition-structure relationships in the Li-ion battery electrode material $LiNi_{0.5}Mn_{1.5}O_4$. *Chemistry of Materials*, 24(15):2952–2964, 2012.

[91] Eun-Sung Lee, Ashfia Huq, Hong-Young Chang, and Arumugam Manthiram. High-voltage, high-energy layered-spinel composite cathodes with superior cycle life for lithium-ion batteries. *Chemistry of Materials*, 24(3):600–612, 2012.

[92] Christoph Dräger, Florian Sigel, Sylvio Indris, Daria Mikhailova, Lukas Pfaffmann, Michael Knapp, and Helmut Ehrenberg. Delithiation/relithiation process of $LiCoMnO_4$ spinel as 5 V electrode material. *Journal of Power Sources*, 371:55–64, 2017.

[93] Keiji Shimoda, Miwa Murakami, Hideyuki Komatsu, Hajime Arai, Yoshiharu Uchimoto, and Zempachi Ogumi. Delithiation/lithiation behavior of $LiNi_{0.5}Mn_{1.5}O_4$ studied by in situ and ex situ ^{6,7}Li NMR spectroscopy. *The Journal of Physical Chemistry C*, 119(24):13472–13480, 2015.

[94] Young Joo Lee and Clare P. Grey. ^{6}Li magic-angle spinning (MAS) NMR study of electron correlations, magnetic ordering, and stability of lithium manganese (III) oxides. *Chemistry of materials*, 12(12):3871–3878, 2000.

[95] Robert A. Armstrong, Nicolas Dupre, Allan J. Paterson, Clare P. Grey, and Peter G. Bruce. Combined neutron diffraction, NMR, and electrochemical investigation of the layered-to-spinel transformation in $LiMnO_2$. *Chemistry of materials*, 16(16):3106–3118, 2004.

[96] RJ. Gummow, A. De Kock, and MM. Thackeray. Improved capacity retention in rechargeable 4 V lithium/lithium-manganese oxide (spinel) cells. *Solid State Ionics*, 69(1):59–67, 1994.

[97] C. Delacourt, A. Kwong, X. Liu, R. Qiao, WL. Yang, P. Lu, SJ. Harris, and V. Srinivasan. Effect of manganese contamination on the solid-electrolyte-interphase properties in Li-ion batteries. *Journal of The Electrochemical Society*, 160(8):A1099–A1107, 2013.

[98] Hosop Shin, Jonghyun Park, Ann Marie Sastry, and Wei Lu. Degradation of the solid electrolyte interphase induced by the deposition of manganese ions. *Journal of Power Sources*, 284:416–427, 2015.

[99] Won-Sub Yoon, Mahalingam Balasubramanian, Kyung Yoon Chung, Xiao-Qing Yang, James McBreen, Clare P. Grey, and Daniel A. Fischer. Investigation of the Charge Compensation Mechanism on the Electrochemically Li-Ion Deintercalated $Li_{1-x}Co_{1/3}Ni_{1/3}Mn_{1/3}O_2$ Electrode System by Combination of Soft and Hard X-ray Absorption Spectroscopy. *Journal of the American Chemical Society*, 127(49):17479–17487, 2005.

[100] Takashi Yamamoto. Assignment of pre-edge peaks in K-edge x-ray absorption spectra of 3d transition metal compounds: electric dipole or quadrupole? *X-Ray Spectrometry: An International Journal*, 37(6):572–584, 2008.

[101] YW. Tsai, BJ. Hwang, G. Ceder, HS. Sheu, DG. Liu, and JF. Lee. In-situ X-ray absorption spectroscopic study on variation of electronic transitions and local structure of $LiNi_{1/3}Co_{1/3}Mn_{1/3}O_2$ cathode material during electrochemical cycling. *Chemistry of materials*, 17(12):3191–3199, 2005.

[102] WL. Roth. The magnetic structure of Co_3O_4. *Journal of Physics and Chemistry of Solids*, 25 (1):1–10, 1964.

[103] Kyung-Wan Nam, Seong-Min Bak, Enyuan Hu, Xiqian Yu, Youngning Zhou, Xiaojian Wang, Lijun Wu, Yimei Zhu, Kyung-Yoon Chung, and Xiao-Qing Yang. Combining in situ synchrotron x-ray diffraction and absorption techniques with transmission electron microscopy

to study the origin of thermal instability in overcharged cathode materials for lithium-ion batteries. *Advanced Functional Materials*, 23(8):1047–1063, 2013.

[104] Jason R. Croy, Hakim Iddir, Kevin Gallagher, Christopher S. Johnson, Roy Benedek, and Mahalingam Balasubramanian. First-charge instabilities of layered-layered lithium-ion-battery materials. *Physical Chemistry Chemical Physics*, 17(37):24382–24391, 2015.

[105] Osvald Knop, KIG Reid, Sutarno, and Yasuaki Nakagawa. Chalkogenides of the transition elements. VI. X-Ray, neutron, and magnetic investigation of the spinels Co_3O_4, $NiCo_2O_4$, Co_3S_4, and $NiCo_2S_4$. *Canadian Journal of Chemistry*, 46(22):3463–3476, 1968.

[106] FMF. De Groot. X-ray absorption and dichroism of transition metals and their compounds. *Journal of Electron Spectroscopy and Related Phenomena*, 67(4):529–622, 1994.

[107] FMF. De Groot, M. Grioni, JC. Fuggle, J. Ghijsen, GA. Sawatzky, and H. Petersen. Oxygen 1s X-ray-absorption edges of transition-metal oxides. *Physical Review B*, 40(8):5715, 1989.

[108] Jin Suntivich, Wesley T. Hong, Yueh-Lin Lee, James M. Rondinelli, Wanli Yang, John B. Goodenough, Bogdan Dabrowski, John W. Freeland, and Yang Shao-Horn. Estimating hybridization of transition metal and oxygen states in perovskites from O k-edge X-ray absorption spectroscopy. *The Journal of Physical Chemistry C*, 118(4):1856–1863, 2014.

[109] Won-Sub Yoon, Mahalingam Balasubramanian, Xiao-Qing Yang, Zugen Fu, Daniel A. Fischer, and James McBreen. Soft X-Ray Absorption Spectroscopic Study of a $LiNi_{0.5}Mn_{0.5}O_2$ Cathode during Charge. *Journal of The Electrochemical Society*, 151(2):A246–A251, 2004.

[110] Jigang Zhou, Da Hong, Jian Wang, Yongfeng Hu, Xiaohua Xie, and Haitao Fang. Electronic structure variation of the surface and bulk of a $LiNi_{0.5}Mn_{1.5}O_4$ cathode as a function of state of charge: X-ray absorption spectroscopic study. *Physical Chemistry Chemical Physics*, 16 (27):13838–13842, 2014.

[111] Ruimin Qiao, L. Andrew Wray, Jung-Hyun Kim, Nicholas PW. Pieczonka, Stephen J. Harris, and Wanli Yang. Direct experimental probe of the Ni(II)/Ni(III)/Ni(IV) redox evolution in $LiNi_{0.5}Mn_{1.5}O_4$ electrodes. *The Journal of Physical Chemistry C*, 119(49):27228–27233, 2015.

[112] Ching-Hsiang Chen, Bing-Joe Hwang, Chun-Yu Chen, Shao-Kang Hu, Jing-Ming Chen, Hwo-Shuenn Sheu, and Jyh-Fu Lee. Soft X-ray absorption spectroscopy studies on the

chemically delithiated commercial $LiCoO_2$ cathode material. *Journal of Power Sources*, 174 (2):938–943, 2007.

[113] D. Ensling, G. Cherkashinin, S. Schmid, S. Bhuvaneswari, A. Thissen, and W. Jaegermann. Nonrigid band behavior of the electronic structure of $LiCoO_2$ thin film during electrochemical Li deintercalation. *Chemistry of Materials*, 26(13):3948–3956, 2014.

[114] Won-Sub Yoon, Kwang-Bum Kim, Min-Gyu Kim, Min-Kyu Lee, Hyun-Joon Shin, Jay-Min Lee, Jae-Sung Lee, and Chul-Hyun Yo. Oxygen contribution on Li-ion intercalation-deintercalation in $LiCoO_2$ investigated by O K-edge and Co L-edge X-ray absorption spectroscopy. *The Journal of Physical Chemistry B*, 106(10):2526–2532, 2002.

[115] LA. Montoro and JM. Rosolen. The role of structural and electronic alterations on the lithium diffusion in $Li_xCo_{0.5}Ni_{0.5}O_2$. *Electrochimica Acta*, 49(19):3243–3249, 2004.

[116] Adrien Boulineau, Loic Simonin, Jean-Francois Colin, Emmanuel Canevet, Lise Daniel, and Sebastien Patoux. Evolutions of $Li_{1.2}Mn_{0.61}Ni_{0.18}Mg_{0.01}O_2$ during the initial charge/discharge cycle studied by advanced electron microscopy. *Chemistry of Materials*, 24(18):3558–3566, 2012.

[117] Ruimin Qiao, Timothy Chin, Stephen J. Harris, Shishen Yan, and Wanli Yang. Spectroscopic fingerprints of valence and spin states in manganese oxides and fluorides. *Current Applied Physics*, 13(3):544–548, 2013.

[118] Jatinkumar Rana, Marian Stan, Richard Kloepsch, Jie Li, Gerhard Schumacher, Edmund Welter, Ivo Zizak, John Banhart, and Martin Winter. Structural changes in Li_2MnO_3 cathode material for Li-Ion batteries. *Advanced Energy Materials*, 4(5):1300998, 2014.

[119] Nadine Dannehl, Sven Ole Steinmüller, Dorothée Vinga Szabó, Mathias Pein, Florian Sigel, Lars Esmezjan, Ulrich Hasenkox, Björn Schwarz, Sylvio Indris, and Helmut Ehrenberg. High-Resolution Surface Analysis on Aluminum Oxide-Coated $Li_{1.2}Mn_{0.55}Ni_{0.15}Co_{0.1}O_2$ with Improved Capacity Retention. *ACS applied materials & interfaces*, 10(49):43131–43143, 2018.

A. Appendix

A.1. Reproducibility of the thermal treatment

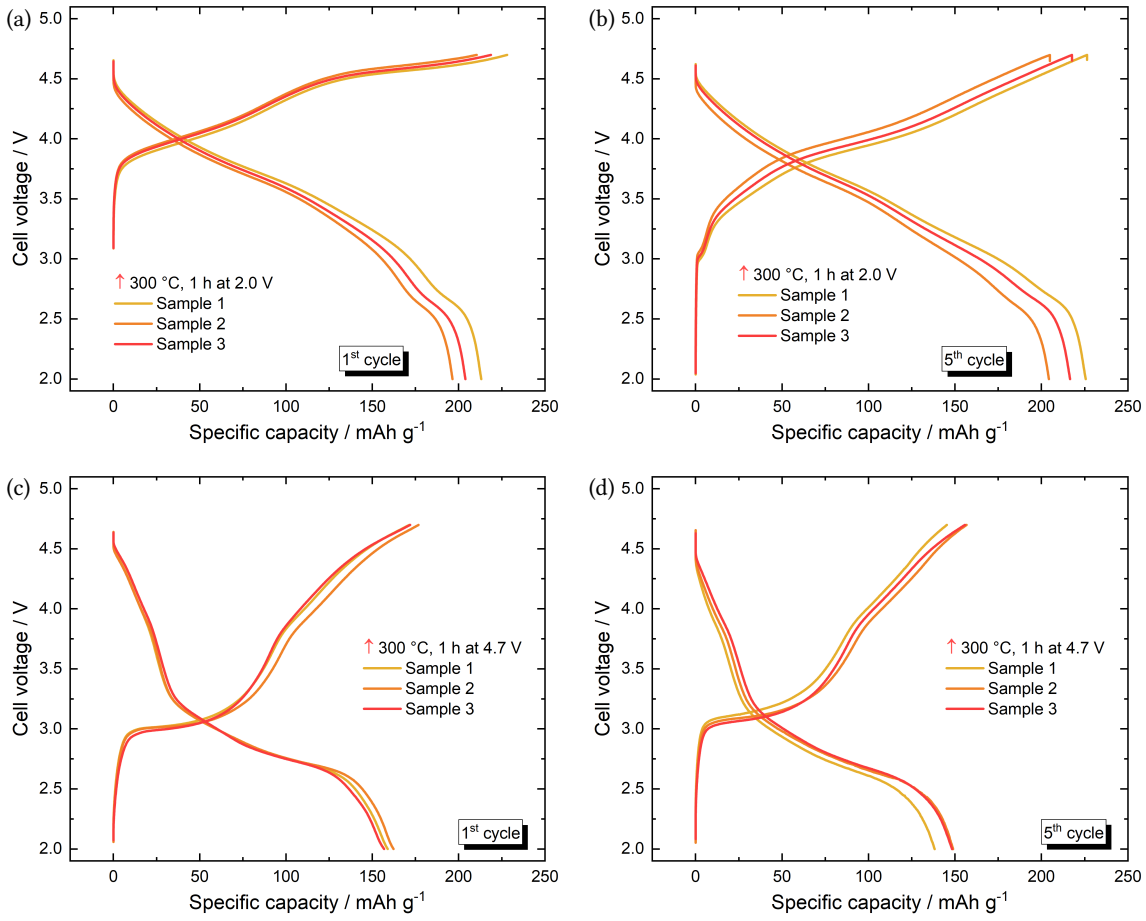

Figure A.1.: Cell voltage vs. specific capacity belonging to the first and fifth post thermal cycles of samples heated in the discharged (a,b) and the charged (c,d) state. In order to illustrate the reproducibility of the procedure, the electrochemical data of three identically treated samples is plotted in each graph. Cycling parameters: 4.7 V-2.0 V, C/10. The first sample of each set is analyzed in detail in the chapter of results.

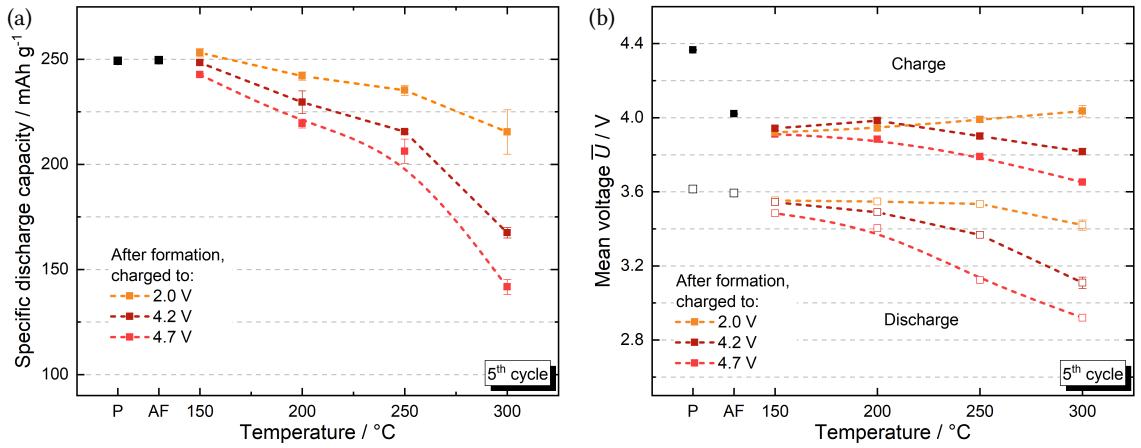

Figure A.2.: Specific discharge capacity (a) and mean charge/discharge voltage (b) vs. heating temperature regarding the fifth post thermal cycle of samples heated in the discharged (2.0 V) and the charged (4.2 V and 4.7 V) state. Each data point represents the mean value and the corresponding standard deviation of three cells. Cycling parameters: 4.7 V-2.0 V, C/10.

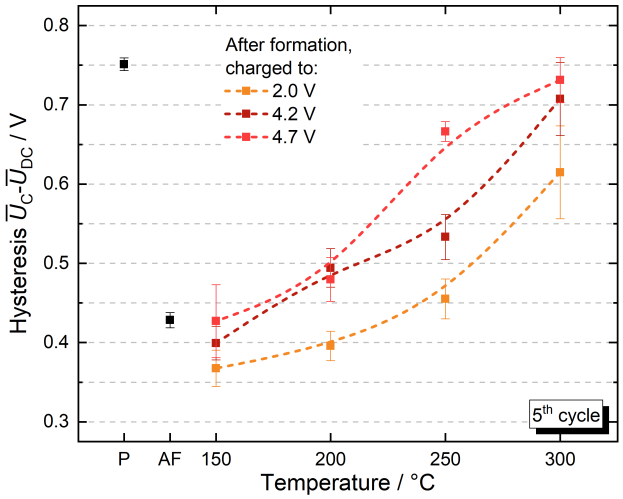

Figure A.3.: Charge/discharge hysteresis vs. heating temperature regarding the fifth post thermal cycle of samples heated in the discharged (2.0 V) and the charged (4.2 V and 4.7 V) state. Each data point represents the mean value and the corresponding standard deviation of three cells. Cycling parameters: 4.7 V-2.0 V, C/10.

A.2. Appendix to Chapter 4

Table B.1.: Actual and nominal composition of the commercial 'HE5050' (TODA) and the self-synthesized ^{6}Li cathode materials determined by elementary analysis using ICP-OES (inductively coupled plasma - optical emission spectrometry). The mean value and the corresponding standard deviation represent the results from a three-fold determination. The ^{6}Li/^{7}Li isotope ratio was determined and considered for the calculations.

	HE5050		6-50:50		6-Li_2MnO_3		6-NCM		6-30:70	
Li	1.207(13)	1.2	1.195(4)	1.2	2.002(10)	2	0.998(5)	1.0	1.126(3)	1.13
Ni	0.154(1)	0.15	0.150(1)	0.15	-	-	0.375(1)	0.375	0.229(1)	0.228
Co	0.101(1)	0.10	0.101(1)	0.10	-	-	0.251(1)	0.25	0.153(1)	0.152
Mn	0.538(5)	0.55	0.554(2)	0.55	0.998(5)	1	0.375(1)	0.375	0.492(1)	0.489

A.3. Appendix to Section 5.1

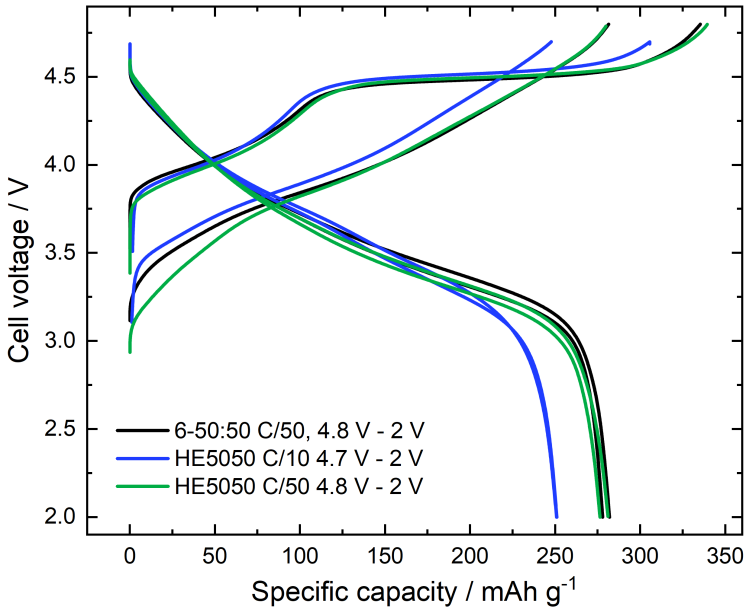

Figure C.4.: A comparison regarding the cell voltage vs. specific capacity of the first and second cycle of the self-synthesized '6-50:50' and the commercial 'HE5050' cathode materials.

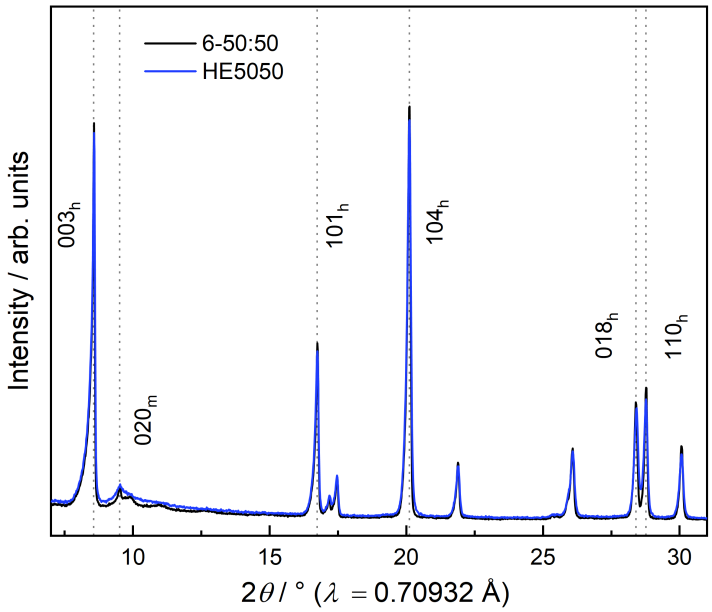

Figure C.5.: Comparison of the X-ray powder diffraction patterns of the self-synthesized '6-50:50' and the respective commercial 'HE5050' cathode material. Reflection-subscripts: h – hexagonal setting, m – monoclinic setting.

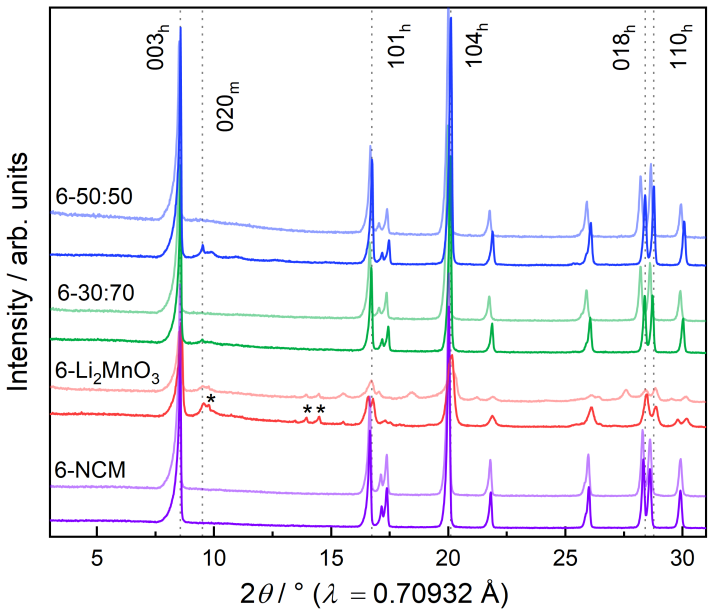

Figure C.6.: X-ray powder diffraction patterns of the self-synthesized ^{6}Li-enriched cathode powders as well as of the respective samples after two cycles (light-colored lines). *Li_2CO_3-associated reflections with space group $C2/c$. Reflection-subscripts: h – hexagonal setting, m – monoclinic setting.

Table C.2.: Nearest-neighbor Li-O-TM configurations for the lithium ions in the different sites in Li_2MnO_3 (space group $C2/m$) and the corresponding observed paramagnetic Li NMR shifts according to Lee et al. [87].

Wyckoff	Li-O-TM bond angle / °	Number of bonds	Li NMR shift / ppm
2*b* (TM layer)	90	12	1460
2*c* (Li layer)	90	8	755
	180	4	
4*h* (Li layer)	90	4	734
	180	8	

A.4. Appendix to Section 5.2

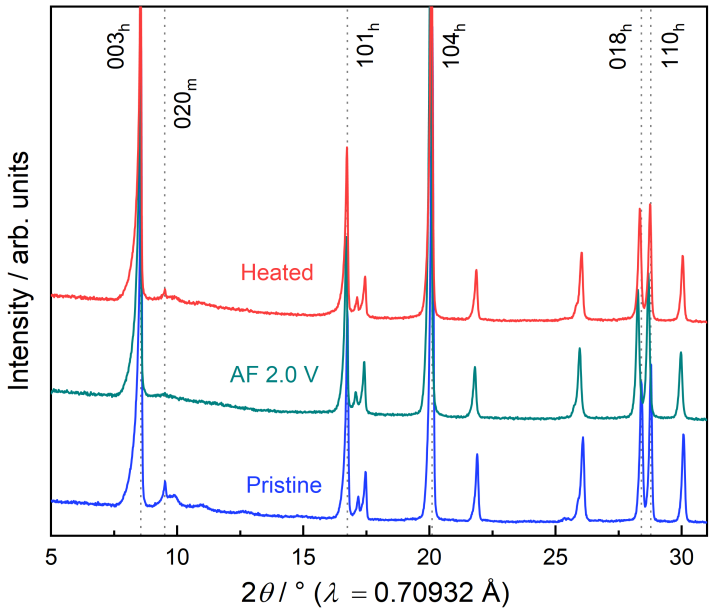

Figure D.7.: X-ray powder diffraction patterns of the '6-50:50' powder in the pristine state as well as of the respective patterns after formation (AF 2.0 V) and after heating (300 °C, 1 h). Reflection-subscripts: h – hexagonal setting, m – monoclinic setting.

A.5. Appendix to Section 5.6

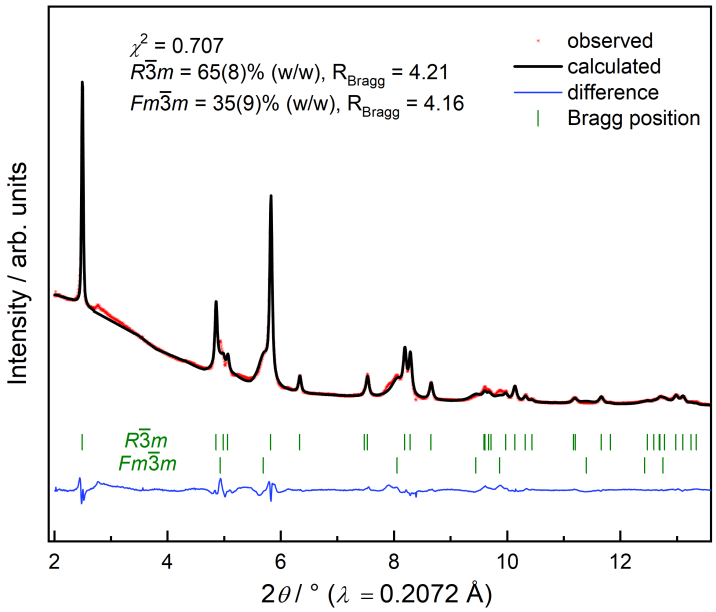

Figure E.8.: Experimental SRPD pattern of a discharged 'HE5050' sample after the thermogravimetric analysis (up to 500 °C) with simulated pattern from the Rietveld refinement and the thereof resulting difference curves (blue).

A.6. Appendix to Section 5.8

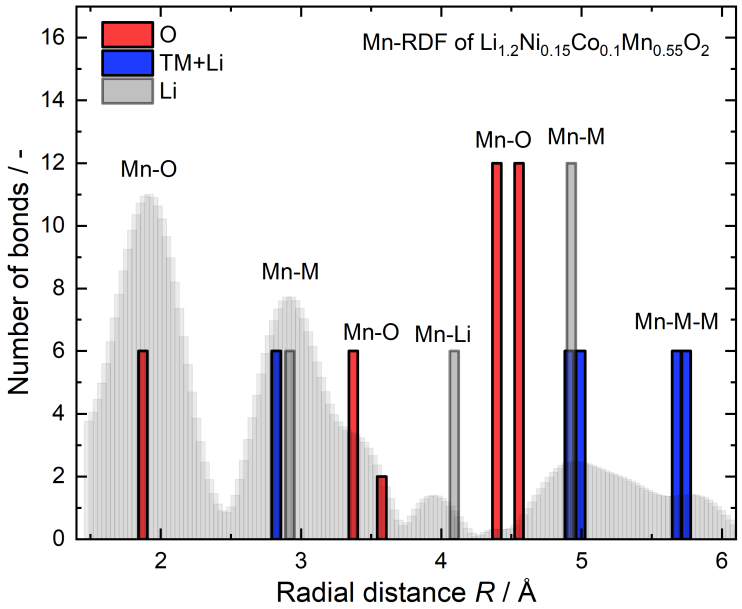

Figure F.9.: Histogram of the bond distances in the Li- and Mn-rich NCM cathode material ('HE5050' composition, $R\bar{3}m$) in comparison with the measured Mn RDF. The radial distances were slightly shifted in order to match the histogram. The bond distances base on refined lattice parameters originating from the diffraction pattern of the pristine 'HE5050' material. A Li/Ni exchange is not considered here. Labels: Mn-O – manganese-oxygen single scattering, Mn-M/Li – manganese-metal single scattering, M-M-M – collinear multiple scattering.

Scientific Contributions

Publications

Christoph Dräger, Florian Sigel, Sylvio Indris, Daria Mikhailova, Lukas Pfaffmann, Michael Knapp, and Helmut Ehrenberg. Delithiation/relithiation process of $LiCoMnO_4$ spinel as 5 V electrode material. *Journal of Power Sources*, 371:55–64, 2017.

Xianhui Zhang, Zhenlian Chen, Björn Schwarz, Florian Sigel, Helmut Ehrenberg, Ke An, Zhifeng Zhang, Qinggang Zhang, Yantu Li, and Jun Li. Kinetic characteristics up to 4.8 V of layered $LiNi_{1/3}Co_{1/3}Mn_{1/3}O_2$ cathode materials for high voltage lithium-ion batteries. *Electrochimica Acta*, 227:152–161, 2017.

Lars Riekehr, Jinlong Liu, Björn Schwarz, Florian Sigel, Ingo Kerkamm, Yongyao Xia, and Helmut Ehrenberg. Fatigue in $0.5Li_2MnO_3$:$0.5Li(Ni_{1/3}Co_{1/3}Mn_{1/3})O_2$ positive electrodes for lithium ion batteries. *Journal of Power Sources*, 325:391–403, 2016.

Lars Riekehr, Jinlong Liu, Björn Schwarz, Florian Sigel, Ingo Kerkamm, Yongyao Xia, and Helmut Ehrenberg. Effect of pristine nanostructure on first cycle electrochemical characteristics of lithium-rich lithium–nickel–cobalt–manganese-oxide cathode ceramics for lithium ion batteries. *Journal of Power Sources*, 306:135–147, 2016.

Nadine Dannehl, Sven Ole Steinmüller, Dorothée Vinga Szabó, Mathias Pein, Florian Sigel, Lars Esmezjan, Ulrich Hasenkox, Björn Schwarz, Sylvio Indris, and Helmut Ehrenberg. High-Resolution Surface Analysis on Aluminum Oxide-Coated $Li_{1.2}Mn_{0.55}Ni_{0.15}Co_{0.1}O_2$ with Improved Capacity Retention. *ACS applied materials & interfaces*, 10(49):43131–43143, 2018.

Conference posters

Florian Sigel, Björn Schwarz, Sylvio Indris, and Helmut Ehrenberg. Thermally induced structural reordering in Li- and Mn-rich layered oxide Li-ion cathode materials. *SNI 2018*, Munich, Germany.

Florian Sigel, Björn Schwarz, Lars Riekehr, Sylvio Indris, and Helmut Ehrenberg. Investigation of degradation behavior in Li- and Mn-rich NCM cathode materials with high-resolution solid state NMR spectroscopy. *ISE Annual Meeting 2016*, The Hague, Netherlands.

Florian Sigel, Björn Schwarz, and Helmut Ehrenberg. Artificial aging of Li- and Mn-rich NCM Li-ion battery cathodes via thermal treatment. *3rd International Summer School Spectroelectrochemistry 2015*, Dresden, Germany.

Florian Sigel, Peter Jakes, Lars Riekehr, Björn Schwarz, Rüdiger Eichel, Cordula Braun, and Helmut Ehrenberg. Investigation of degradation behavior in Li-rich NCM cathode materials with spectroscopic methods. *SFB 595 – International Symposium on Electrical Fatigue in Functional Materials 2014*, Sellin, Germany.

Conference talks

Florian Sigel, Björn Schwarz, Lars Riekehr, Sylvio Indris, and Helmut Ehrenberg. Investigation of degradation behavior in Li- and Mn-rich NCM cathode materials with high-resolution solid state NMR spectroscopy. *German-Israeli Battery School 2016*, Munich, Germany.